Density Functional Theory Modelling of Intrinsic and Dopant-Related Defects in Ge and Si

Submited by Colin Janke to the University of Exeter as a thesis for the degree of Doctor of Philosophy in Physics.

December, 2008

I certify that all material in this thesis which is not my own work has been identified and that no material is included for which a degree has previously been conferred upon me.

Abstract

This thesis covers the application of the local density approximation of density functional theory to a variety of related processes in germanium and silicon. Effort has been made to use calculated results to explain experimentally observed phenomena.

The behaviour of vacancies and vacancy clusters in germanium has been studied as these are the dominant intrinsic defects in the material. Particular attention was paid to the annealing mechanisms for the divacancy as a precursor to the growth of the larger clusters, for which the electrical properties and formation energies have been studied. Some preliminary work is also presented on the germanium self-interstitial structure and migration paths.

Attention was then turned to a selection of dopant-vacancy defects in both silicon and germanium. An effort was made to explain recent experimental observations in silicon through investigating a number of defects related to the arsenic E-centre. Following this, the properties of donor-vacancy clusters in germanium were studied, and comparison with the results calculated for silicon suggest a significant parallel between the behaviour of the defects and dopants in the two materials.

Finally, extensive work was performed on the diffusion of phosphorus and boron in germanium. Diffusion of both dopants was studied via interstitial and vacancy mediated paths as well as by a correlated exchange path not involving any intrinsic defects. The results obtained confirmed current theories of the mechanisms involved in the diffusion of the two defects, while also expanding the knowledge of other paths and giving Fermi level dependences for the energy and mechanism for diffusion of the two defects. Boron diffusion was found to exhibit strong Meyer-Neldel rule effects, which are used to explain the unusually high diffusivity prefactors and energy barriers calculated from experimental measurements for this dopant.

Acknowledgements

The research presented between these covers owes its existence to many people, and I would like to take this space to express my gratitude.

First and foremost, my supervisor of the past three years, Prof. Robert Jones, whose enthusiasm, insight and guidance have been a great benefit, and who has always had time for my questions and puzzles.

Secondly, my family, especially my parents, Susan and Eric Janke, who kindled my interest in science and the natural world so many years ago, and without whose support and encouragement this thesis would never have been completed.

Various members of the extended AIMPro group are due a mention here, too: Patrick R. Briddon for making the code available and working tirelessly to maintain and improve it, Alexandra Carvalho and Naomi Fujita for their friendship over the past three years, Steve Sque, Luke Hounsome and Thomas Eberlein for their patience and guidance with my interminable questions and mistakes, Sven Öberg for allowing us to use his computers and spending significant time and effort on getting my calculations running and José Coutinho for his guidance and encouragement, and for showing me that you don't *have* to wear a suit to a conference.

Derek W. Palmer, for many insightful discussions on the experimentalist's view of the field and invaluable time spent proof-reading this thesis.

The Engineering and Physical Sciences Research Council for the financial backing which has allowed me to perform this research and present it at several conferences.

Finally, to Mark Roberts-Mapp, my long suffering house mate for helping me remain connected to the real world (and several less real ones) outside the walls of the Physics Department, and to my many other friends, particularly those involved with Heart of Pargon for making sure I didn't forget that there is more to life than solid state physics.

List of Publications

First Author

1. *Supercell and cluster density functional calculations of the thermal stability of the divacancy in germanium*
   C. Janke, R. Jones, J. Coutinho, S. Öberg and P. R. Briddon, Mat. Sci in semicond. Proc. **9**, 484 (2006)

2. *Ab initio investigation of boron diffusion paths in germanium*
   C. Janke, R. Jones, S. Öberg and P. R. Briddon, J. Mater. Sci.: Mater. Electron. **18**, 775 (2006)

3. *Supercell and cluster density functional calculations of the thermal stability of the divacancy in germanium*
   C. Janke, R. Jones, S. Öberg and P. R. Briddon, Phys. Rev. B, **75**, 195208 (2007)

4. *Ab initio studies of arsenic and boron related defects in silicon mesa diodes*
   C. Janke, R. Jones, S. Öberg and P. R. Briddon, Appl. Phys. Lett **90**, 152103 (2007)

5. *Ab initio investigation of boron diffusion paths in germanium*
   C. Janke, R. Jones, S. Öberg and P. R. Briddon, Phys Rev B, **77**, 075208 (2008)

6. *Ab initio investigation of phosphorus diffusion paths in germanium*
   C. Janke, R. Jones, S. Öberg and P. R. Briddon, Phys Rev B, **77**, 195210 (2008)

7. *Ab initio investigation of phosphorus and boron diffusion in germanium*
   C. Janke, R. Jones, J. Coutinho, S. Öberg and P. R. Briddon, Mat. Sci. in Semicond. Proc., in press

Collaborative Work

1. *Early stage donor-vacancy clusters in germanium*
   J. Coutinho, V. J. B. Torres, S. Öberg, A. Carvalho, C. Janke, R. Jones and P. R. Briddon, J. Mater. Sci: Mater. Electron., **18**, 769 (2006)

2. *Strong compensation of n-type Ge via formation of donor-vacancy complexes*
   J. Coutinho, C. Janke, A. Carvalho, V. J. B. Torres, S. Öberg, R. Jones and P. R. Briddon, Phys. B, **401**, 179 (2007)

3. *Self-interstitial in germanium*
   A. Carvalho, R. Jones, C. Janke, J. P. Goss, P. R. Briddon, J. Coutinho, S. Öberg, Phys. Rev. Lett., **99**, 175502 (2007)

4. *Limits to n-type doping in Ge: Formation of donor-vacancy complexes*
   J. Coutinho, C. Janke, A. Carvalho, S. Öberg, V. J. B. Torres, R. Jones, P. R. Briddon, Defects and Diffusion Forum, **273**, 93 (2008)

5. *Primary defects in n-type irradiated germanium: a first-principles calculation*
   A. Carvalho, R. Jones, C. Janke, S. Öberg and P. R. Briddon, Sol. Stat. Phen., **131-133**, 253 (2008)

6. *First-principles study of the diffusion mechanisms of the self-interstitial in germanium*
   A. Carvalho, R. Jones, J. P. Goss, C. Janke, S. Öberg and P. R. Briddon, J. Phys.: Cond. Mat., **20**, 135220 (2008)

Contents

List of Figures

List of Tables

Chapter 1

Introduction

1.1 Introduction

Semiconductor devices are almost omnipresent in modern life, and their continued development and evolution come on the back of a great deal of dedicated research across the world. In 1965, G. E. Moore predicted that the complexity of such devices would double every year, later revised down to two years, for at least a decade [1]. The law has so far held, more or less, for over fifty years and has become a benchmark for progress as much as a prediction of it.

In modern devices, the drive to achieve the high component density predicted by Moore's Law has led to a requirement for junctions of the order of a few tens of nanometres across, and this small scale engineering has magnified the issues surrounding reliable, stable nano-scale doping of semiconductors.

1.2 Silicon and Germanium

Since the early days of semiconductor devices when the first junctions were manufactured on germanium substrates, the industry has turned almost exclusively to silicon for a number of reasons. Technologically, the existence of a stable silicon oxide to serve as a dielectric on the device surface was a very important point in favour of silicon. Economically, the scarcity and cost of germanium have also played a role in ensuring the dominance of silicon in commercial electronic applications.

More recently, with the advance of semiconductor technology, the use of SiO_2 as a dielectric is becoming challenging as the dielectric thickness approaches the point where electron tunnelling is an important effect. Interest is hence growing in the use of other materials, with higher dielectric constant κ, such as HfO_2. However, the use of such non-native, high-κ dielectrics decreases the channel carrier mobility in these devices [2]. Germanium then becomes a desirable candidate material due to its higher low field mobility - a factor of two higher for electrons and four for holes compared with silicon [3] while the use of a non-native dielectric removes the issue of a lack of stable germanium oxide.

The manufacture of germanium devices can also benefit from the expertise that has been developed in silicon, as germanium crystal growth is very similar to that for silicon. The integration of germanium based devices into silicon technology is therefore an appealing concept. The higher density and lower physical strength of germanium compared with silicon does restrict the size of germanium wafers currently [3], but work is ongoing to improve the techniques for germanium growth.

Experimentally, the properties of germanium are much less well understood than those of silicon. This is largely due to the dominance of silicon technology for the past several decades, but is also affected by difficulties in transferring techniques which have been very successful in silicon to germanium. Electron paramagnetic resonance, for example, is a technique which has been used to great effect in silicon, while in germanium, it suffers from weak signals and complex hyperfine coupling resulting in broad lines [4].

Modelling of germanium has also encountered problems. The small experimental band gap of germanium, combined with the well known underestimation of the band gap using density functional theory (DFT) leads to negligible and sometimes negative values for the band gap calculated in this way and therefore poses serious problems for calculations involving electrically active defects.

Despite these problems, the study of germanium and the defects that it regularly contains progresses apace with the work presented in this thesis forming a part of a substantial growth in knowledge in this area.

1.3 Unintentional Defects

In addition to intentional doping of semiconductor crystals, which will be discussed below, there are often also unintentional defects present. These can be intrinsic - involving only atoms which would be present in the perfect crystal - or extrinsic - involving species foreign to the crystal.

1.3.1 Intrinsic Point Defects

Intrinsic point defects (IPDs) consist of vacancies, crystal sites without an atom, and self-interstitials, additional native atoms in the crystal. The latter can exist in different structures, most commonly the $\langle 110 \rangle$ split interstitial, where two atoms share a single crystal site separated along a $\langle 110 \rangle$ direction, the interstitial at a T-site, a position in the crystal where the extra atom has four equivalent nearest neighbours, and the interstitial at an H-site, where the interstitial has six neighbours. These structures are illustrated in Figure 1.1. Establishing the most stable configuration for the vacancy and interstitial is the subject of ongoing, primarily theory-lead, research in the field.

1.3.1.1 Vacancies

DFT investigations on the vacancy in germanium have demonstrated a number of charged states in the band-gap, and lattice relaxations which are strongly charge-dependant [5, 6]. It has been shown that the relaxations are strongest along the $\langle 110 \rangle$ chains containing the vacancy, and extend at least to the fifth shell of neighbour atoms [7]. The symmetry of the vacancy in germanium has been calculated to

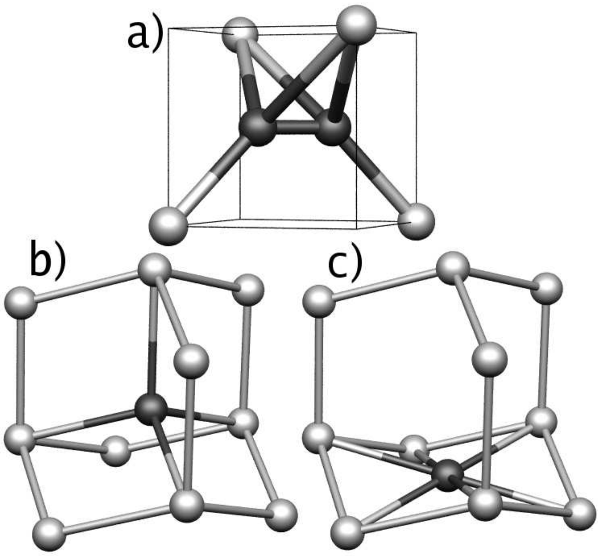

Figure 1.1: Diagrams showing three different configurations for the interstitial atom in a silicon or germanium crystal. In all pictures, the interstitial atom or atoms are shown in a darker grey than the surrounding crystal atoms. a) The ⟨110⟩ split-interstitial, whereby two atoms share a single crystal site. b) The tetragonal or *T*-site, where the interstitial atom is at the centre of a tetragonal cage, with four nearest neighbours. c) The hexagonal or *H*-site, where the interstitial atom is at the centre of a hexagonal ring of atoms, with six nearest neighbours.

depend on the charge state of the defect, with the doubly positive state having a structure almost identical to the unrelaxed case, with T_d symmetry. The atoms surrounding the vacancy are found to relax inward as electrons are added, forming extended bonds between them that reduce the energy of the vacancy. Although there is agreement that the inward relaxations of the surrounding atoms increase with increasingly negative charge state, the symmetry for the singly and doubly negative charge states of the vacancy are found to be either C_2 or D_2 in different studies [5, 6]. The relaxations for all charge states of the vacancy are shown to be smaller than their equivalents in silicon, as are the Jahn-Teller distortions, due to a much smaller electron-lattice coupling in germanium [8]. The type of the Jahn-Teller distortions calculated for the germanium vacancy is also still debated [9, 10]. Energy levels have been calculated using the formation-energy method (see Section 3.3.4) to give the first donor level as lying at $E_v+0.20$ eV, with the first and second acceptors at $E_v+0.37$ and $E_v+0.40$ eV respectively [9]. A later study using the marker method (see Section 3.3.4) gives the donor levels of the vacancy as lying within the valence band, while the $E(-/0)$ energy is calculated to fall at $E_v + 0.20$ or 0.17 eV depending on the details of the method used, and the $E(=/-)$ and $E(\equiv/=)$ levels are found to lie at $E_c - 0.5$ eV and $E_c - 0.3$ eV respectively [5]. The latter work seems to be in better agreement with experiments outlined below.

An experimental study [11] of the vacancy, using perturbed angular correlation spectroscopy (PACS) has been performed, using probe atoms to trap vacancies for measurement. By applying an argument based on a combination of coulomb and strain interactions between the vacancy and the negatively charged probe atom or the similarly charged dopant atoms, it is shown that the acceptor level lies in the range $E(-/0) = E_v + 0.20 \pm 0.04$ eV. A more recent study [12] using deep level transient spectroscopy (DLTS) methods gave a position for a vacancy acceptor level at $E_v + 0.14$ eV.

In silicon, the vacancy has been calculated in theoretical studies [13] to exhibit Anderson negative-U level ordering [14]. This is an effect in which structural relaxations between charge states provide energy gains that are sufficient to offset electron-electron Coulomb repulsion, thus allowing two electrons to be bound to a defect with the second electron held more tightly than the first. For the vacancy in silicon, this is observed between the doubly positive and neutral charge states such that the first donor level lies below the second. The defect can be observed experimentally in five charge states, ranging from the doubly positive to doubly negative [15].

1.3.1.2 Self-Interstitials

The self-interstitial has also been studied using DFT calculations, and has been shown to be most stable in the $\langle 110 \rangle$ split-interstitial configuration [7, 16]. Energy levels have been calculated to lie at $E(0/+) = E_v + 0.07$ eV and $E(-/0) = E_v + 0.31$ eV [6, 16]. There is still some debate as to whether the formation energy of the $\langle 110 \rangle$ split interstitial is higher in silicon or germanium. Earlier studies had given a lower formation energy in germanium [7, 6, 16], but later calculations give, for larger **k**-point sampling sets, a larger formation energy in germanium [17].

The PACS study mentioned above for the vacancy also included results for the Ge self-interstitial. Analysis of the data suggests that the self-interstitial has a donor level in the range $\mathrm{E}(0/+) = \mathrm{E}_\mathrm{c} - 0.04 \pm 0.02$ eV [11]. This is not compatible with the theoretical work presented above, and the authors of the above work suggest that the observed energy level is the $\mathrm{E}(-/0)$ level [6, 16, 17]. Subsequent experimental work has consistently yielded a donor nature of the level, placing it between $\mathrm{E}_\mathrm{c} - 0.2$ and 0.04 eV [12, 18, 19].

In silicon, the $\langle 110 \rangle$ split-interstitial is found to be one of two degenerate forms of the defect with the hexagonal-sited interstitial the other. There do not appear to be any energy levels within the band-gap, but this may be due to the reduced band-gap of DFT [20]. The self-interstitial in silicon has not been observed directly in experiment, though a number of indirect measurements have attributed energy levels to this defect [21].

1.3.1.3 Formation

Vacancies and interstitials can be formed thermally or by atoms being displaced from crystal sites through interaction with high energy particles. In the latter, the energy needed can come from atoms being implanted by an ion beam, or from intentional or incidental irradiation with protons, electrons, neutrons or γ-rays. Thermal quenching experiments can be used to study excess thermally generated defects.

In germanium, due to its having a lower formation energy than the self-interstitial, the vacancy is the dominant defect [22]. One indirect measure of thermal vacancy concentration can be obtained from diffusion experiments in germanium. It is believed that metal atoms in germanium diffuse in the interstitial state, and then combine with vacancies, falling into substitutional sites. By studying substitutional metal concentration as a function of depth into the sample, and applying this model, the vacancy concentration can be derived. Results suggest that crystal surfaces act as sources for vacancies, and give an upper limit for the equilibrium concentration of around 10^{14}–10^{15} cm^{-3} at 750 to 850°C[23].

Another, more direct measurement involves studying the electrical properties of heat-treated germanium samples. By comparing the observed generation of acceptor levels with the suggested electrical activity of the intrinsic defects in germanium, it is possible to show that thermal treatment creates Frenkel (vacancy-interstitial) pairs rather than isolated vacancies. Also, the equilibrium concentration of vacancies can be determined, giving

$$C_V^{eq}(T) = 3 \times 10^{23} \exp\left(-\frac{2.01\text{eV}}{k_B T}\right) \text{ cm}^{-3} \tag{1.1}$$

for the equilibrium concentration, with $C_V^{eq}(T) = 1.3 \times 10^{15}$ cm^{-3} at the melt temperature of 938°C, consistent with the results above [24].

Irradiation studies also demonstrate that acceptor levels can be created in the bandgap [25]. After low-temperature irradiation, several electron traps and one hole trap were detected by DLTS, although it is not believed that all of these are due to single vacancies and interstitials [26]. By measuring the introduction rates as a function of electron irradiation energy, the minimum energy required to create these centres can be determined. This can help identify them, and the energy to displace a single germanium atom is thus found to be 20±5 eV [27]. It has also been suggested that, as in silicon, irradiation produces large numbers of close-bound Frenkel pairs that are not observable to most detection schemes [28].

1.3.1.4 Intrinsic Point Defect Clusters

Clusters of vacancies or interstitials may also be found in semiconductors. Clustering leads to new defect centres and eventually to large voids or interstitial clusters that can have severe effects on device behaviour. Large vacancy clusters have been observed in germanium [29], and this combined with the dominance of the vacancy in germanium has lead to a great deal of interest in theoretical studies on the behaviour of vacancy clusters of varying sizes.

A divacancy consists of two vacancies at adjacent crystal sites, stable due to the reduction in the number of incomplete bonds per vacancy. This reduction continues for larger clusters of vacancies, as will be discussed in Section 5.4. Irradiation studies in germanium have detected a defect centre with a minimum energy for formation of 40 ± 10 eV, twice the energy for displacing a single atom. This centre is therefore identified as the divacancy, as interstitials are more likely to be scattered apart [26, 27]. Acceptor levels at $\mathrm{E_v} + 0.20$ and 0.24 [19] or $\mathrm{E_v} + 0.37$ eV [30] have been attributed to the divacancy, though the latter level has more recently been attributed by the original authors to a larger vacancy cluster [31]. Theoretical calculations for the divacancy in silicon and germanium have been carried out, and have demonstrated that, as with the monovacancy, relaxations and Jahn-Teller distortions are smaller in germanium than silicon [10].

One experimental study [32] claims to have detected tetravacancies after neutron irradiation, basing the assignment on symmetry measurements taken using stress studies, although other properties of the defect are not reported.

In germanium, bulk microdefects have been observed by x-ray topography and small-angle x-ray scattering experiments [33] and by optical microscopy [29]. The former method detects defects in the size range of hundreds of nanometres, while the latter looks in the 1 to 6 micron range. The latter paper describes the observed defects as voids, or vacancy clusters, while the former does not assign a species. A radial dependence of defect concentration within germanium wafers is observed in the first study, with larger defects concentrated at the centre, and smaller ones toward the edge of the wafers [33].

1.3.1.5 Annealing Behaviour

As well as the electronic properties, the annealing behaviour of defects is important from a device viewpoint. Heat treatments during device fabrication cause many defects to anneal, and understanding these processes can help to optimise the treatments used.

Experiments using resistivity measurements have suggested that germanium self-interstitials are highly mobile, but collect at dislocations, preventing recombination with vacancies. At higher temperatures, given as 516°C, the interstitials escape from the dislocations and annihilate with vacancies [24]. Work studying local vibrational modes (LVMs) concluded that vacancies become mobile at around 60K [34]. Later work [25] using conductivity measurements supported this, and suggested that in *n*-type material, the interstitial is trapped at a dopant atom. Coulombic attraction between the donor and the vacancy could then enhance the recombination rate. More recent DLTS results have suggested that the vacancy anneals out at around 100K [26], and positron lifetime spectroscopy and PACS results have suggested 200K [11, 35]. These discrepancies may well be due to differing environments for the experiments, as the diffusion barrier for the defects is expected to depend on charge state, and therefore on Fermi level.

Most experimental studies on germanium suggest that divacancies are more stable than monovacancies, and have been shown by DLTS experiments to anneal at 125°C[32], 150°C[26] or 180°C[30] in studies on a variety of *n*-type germanium samples with varying levels of phosphorus, antimony and oxygen doping. There have been few results suggesting an evolution of IPDs in germanium, with those models proposed assuming annihilation as the annealing mechanism.

In silicon, the migration energy of the divacancy is known directly from paramagnetic resonance experiments to be around 1.3 eV, and fairly insensitive to the charge state of the defect, while the dissociation energy must be at least 1.6 eV as divacancies anneal by migration [36]. In highly oxygenated float-zone silicon, the divacancy anneals at 220-300°C, evolving into a defect with similar energy levels, assigned to the V_2O centre [37]. It has also been shown that migration of the divacancy in silicon is a one-step process, and hence that dissociation requires two atoms to simultaneously move between the vacancies as the V-Si-V structure is unstable [38]. The migration barrier for the single vacancy has also been calculated from experimental measurements to be 0.45 eV in the neutral charge state and 0.32 eV in the doubly positive charge state with the same energy and mechanism at cryogenic and elevated temperatures [39]. This lies in contrast with previous work which has suggested a much higher barrier for high temperature vacancy diffusion of around 1.8 to 2.8 eV [40, 41, 42, 43]. Theoretical studies [20] have found a migration energy for the self-interstitial of 0.03-0.20 eV depending upon the method used and the path taken. The low energy and multiple path options explain why the self-interstitial dominates diffusion in silicon.

1.3.1.6 Self Diffusion Mechanisms

Self-diffusion in both silicon and germanium is mediated by intrinsic point defects. In germanium, tracer diffusion experiments suggest that in intrinsic material, the negatively charged vacancy accounts for 77% of self-diffusion, leading to an increase in self-diffusion with *n*-type doping, and a reduction with *p*-type [44]. From theory that both self-diffusion and diffusion of copper are limited by vacancies, copper diffusion can be used to study self-diffusion by estimating the diffusivity of vacancies. This has been done, and the results are in good agreement with direct experiments, supporting the assignment of the same mediating defect to copper and self-diffusion [23]. A more recently developed method uses isotopically-rich germanium heterostructures, with a series of layers containing different stable isotopes of germanium at high purity. By studying depth profiles using secondary ion mass spectroscopy (SIMS) measurements, diffusion profiles can be obtained for each isotope. The results from this process support previous work and open up new methods of study [45]. Experimental results suggest an activation energy for self-diffusion of 3.1 eV, with a pre-exponential factor of about 11 $\mathrm{cm^2s^{-1}}$ [22].

For silicon there seems to be disagreement on the activation energy for self diffusion, with results ranging from 3.5 to 4.9 eV reported [46].

1.3.2 Dislocations

Dislocations are extended intrinsic defects, see Figure 1.2. Dislocations can propagate from the seed crystal during growth, and they affect electronic properties. Dislocations are also known to act as both sources and sinks for vacancies, and for

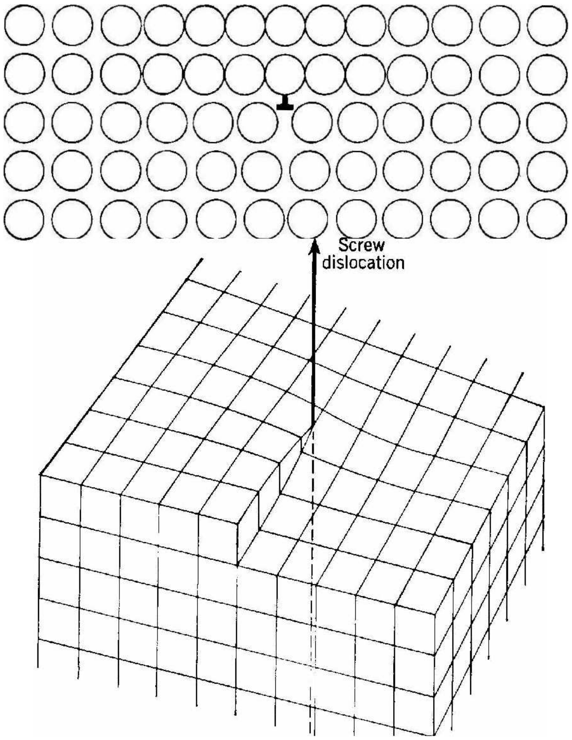

Figure 1.2: Diagrams showing the two types of dislocations in crystals. Top: Edge dislocations consist of a line of under co-ordinated atoms, running out of the plane of the page. It can also be thought of as an extra plane of atoms inserted into the crystal. Bottom: A diagram showing a screw dislocation, where the atoms have the co-ordination of the perfect crystal, but the arrangement of atoms is distorted so as to create a ‘screw’ structure around a dislocation axis, as shown. From Reference [48].

some applications, a small concentration of dislocations is desirable to avoid void and V_2H formation [22]. It is also known that dislocations trap interstitials and vacancies via strain fields. This can be important for the dynamics of the simpler intrinsic defects [24, 47].

1.3.3 Donor-Vacancy Complexes

In silicon and germanium, single donor-vacancy complexes are termed E centres. They are important as they can remove donors from electrically active substitutional sites and contribute to dopant diffusion. The predominance of vacancies in germanium combined with the compatible charge states of the donor atom and vacancy make these defects very important in any study of donor deactivation in this material.

Experimental studies have been performed on the E-centre, demonstrating a reduction in donor centres as they are generated. One study, on germanium samples with a variety of donor species, used γ irradiation to generate the vacancies, then Hall coefficient measurements to estimate the number of donor and acceptor centres present. They concluded that the E-centres of phosphorus, arsenic, antimony and bismuth are electrically inactive, and observed a small number of acceptor states, attributed to divacancy-donor complexes [49] . In contrast, a later study also using γ irradiation, the same dopants and capacitance transient techniques to study the electrical activity, concluded that the centres act as double acceptors, with energy levels in the band-gap [50]. The latter study also reported that the centres, anneal in the range 100-300°C, with thermal stability increasing with increasing size of the donor atom. Their results for the antimony E-centre also agree with those of a DLTS study into various defects in antimony-doped germanium [30].

Experimental work in silicon using positron annihilation spectroscopy (PAS) has identified a series of defects associated with a decrease in carrier concentration in heavily *n*-doped material. Donor vacancy (DV) complexes are observed to anneal out at around 150°C, and are replaced by D_2V, and then D_3V at around 400°C in samples with sufficient donor concentration. The subsequent annealing of D_3V defects at around 800°C is not associated with the growth of a larger defect, but coincides with a recovery of carrier concentration at around this temperature [51, 52]. A signal associated with a larger defect, tentatively identified as D_5V_2, has been observed, but not at concentrations significant to the electrical activity of the samples.

In germanium and silicon, such defects have been studied theoretically, and the D_3V and D_4V defects have been predicted to have a negative formation energy relative to isolated substitutional donor atoms in both materials [53, 54]. In germanium, there has been a suggestion that Sb_5V may be stable, though a formation mechanism has not been proposed [55].

1.4 Doping

Doping of semiconductors is a fundamental process in device manufacture. In germanium, *p*-type doping has been achieved with boron [56, 57, 58], while phosphorus [59], arsenic [57, 59] and antimony [57] have been studied as *n*-type dopants.

This is very similar to the list of dopants used in silicon, where boron, nitrogen, phosphorus, arsenic and antimony are often used [60, 61, 62, 63, 64].

1.4.1 Implantation of Dopants

There are different approaches that can be used to insert dopants into semiconductors to create the doped regions required for devices or research.

Molecular beam epitaxy (MBE) involves growing a layer of dopant rich material upon a usually undoped substrate. Using this method, junctions cannot be grown on the length scales required for device manufacture, but it is often used for experimental studies of defects as the technique produces relatively few defects ($\sim 10^7$ cm^{-2}) [58].

Ion-beam implantation (IBI) involves firing dopant ions into the material with energies of tens or hundreds of keV. The ions are usually angled at around 7° to avoid ion channelling effects where the ions travel through open channels in the diamond structure. The penetration depth for the ions can then be controlled by adjusting the beam energy [56, 57, 58, 59]. This method allows nano-scale junction formation, but also generates many IPDs, (see Section 1.3.1), and many of the dopant atoms do not lie in electrically active substitutional sites immediately after implantation. Post-implantation processing to anneal out the defects and activate the dopants is then required, and much research has been devoted to achieving this while minimising the diffusion of implanted dopant atoms.

There is a variation on the IBI technique intended to minimise the required annealing, involving pre-implantation amorphisation of a layer of material by firing ions of the same material into it. Much of the damage caused by the dopant ions then causes solid phase epitaxial regrowth of the crystal, allowing higher substitutional dopant concentration to be achieved and lower annealing requirements to remove the implantation damage [56, 65].

1.4.2 Dopant Activation

After IBI, dopant atoms need to be activated by moving them to substitutional lattice sites. This is usually achieved through heat treating the sample.

Dopant activation in germanium has been studied intensively in the past. From spreading resistance probe (SRP) and SIMS data, it is possible to determine both the active and total concentrations of dopants respectively [56, 57, 59]. Comparing results of these measurements allows the fraction of active dopants to be evaluated and studied after a variety of heat treatment steps.

It is desirable during post-implantation processing to minimise the thermal budget, defined by both the temperature of the thermal treatment and its duration. This is because, as well as removing implantation defects and activating dopants, the elevated temperatures can also cause the diffusion of dopants, deepening and widening junctions and diluting the dopant concentration.

Rapid thermal annealing (RTA) studies on germanium have been carried out [57, 59], and have achieved activated concentrations of $\sim 10^{20}$ cm^{-3} for RTA treatment at 650°C for 10 s, with both boron and phosphorous doping [57]. For shallow junctions, treatments with a small thermal budget can be used to activate the dopants and remove implantation damage, but for deeper junctions, more implantation damage is present, and the higher thermal budget required results in a greater degree of dopant diffusion. It has also been shown that dopant implantation above the solid-state solubility limit does not result in greater activated dopant concentration, merely increased damage [59].

Studies on the technique involving pre-implantation amorphisation of the germanium described above have shown that the best results are achieved for an amorphised region which is just deep enough to survive implantation. The remaining amorphous region can then be recrystallised with a minimal further anneal. Active dopant concentrations of 4.5×10^{20} cm^{-3} are reported [56, 65].

1.4.3 Dopant Diffusion

Dopant diffusion in semiconductors is an important area of research, as it is the process which limits junction size during heat treatments.

For *p*-type regions in germanium, boron has been studied as a dopant, and has been found to have very low diffusivity. With an activation energy for diffusion of $\sim$ 4.5 eV, it does not diffuse until annealing treatments at ~900°C for eight hours are performed [58]. The high diffusion barrier for boron is accompanied by a high pre-exponential factor of $\sim 10^5$ cm^{2}s^{-1} compared with typical values of around ~ 1 cm^{2}s^{-1} for most other diffusion processes. It is also found that the diffusivity of boron is the same whether the boron is inserted into the material using IBI or MBE techniques [58, 66, 67, 68]. One theoretical study has been performed on interstitial-mediated boron diffusion in germanium. The calculations yielded a diffusion barrier of 4.5 eV, but did not offer an explanation for the anomalously large pre-exponential factor [69].

This compares with the case in silicon, where boron is found to diffuse more quickly, with a diffusion barrier of 3.2-3.6 eV but a more modest pre-exponential factor of ~ 0.8 cm^{2}s^{-1} [61]. Transient enhanced diffusion (TED) is also observed, whereby diffusion is greatly enhanced by interaction with excess IPDs, likely self-interstitials, after ion implantation. Carbon has been used to arrest this process by trapping self-interstitials, but it has now been shown that carbon atoms may also trap boron, forming undesirable, electrically active complexes [60]. It has also been shown that boron in silicon diffuses by an interstitial-mediated mechanism, as the vacancy-mediated diffusion energy is too high [62]. Various theoretical studies have been performed on boron diffusion in silicon, giving a number of interstitial-mediated diffusion paths with similar energy barriers [61, 70, 71].

Doping to produce *n*-type regions has been studied with a larger variety of dopants, and diffusion has been found to be quicker in germanium than silicon. Phosphorus, arsenic and antimony have been studied as possible *n*-type dopants in germanium. They have been shown to diffuse with activation energies of ~ 2.7 eV [57, 72, 73]. Tailing of the dopant profile is observed with phosphorus, where a region of low dopant concentration extends significantly past the edge of the grown-in junction, softening the junction edge. Significant out-diffusion has also been observed with phosphorus and antimony doping where a portion of the dopant atoms diffuse out of the surface of the sample, reducing the concentration available to provide carriers within the doped region [74]. Theoretical work suggests that a vacancy-mediated mechanism for the diffusion of these species matches the barriers calculated from experimental measurements [55].

In silicon, the diffusion of these dopants has also been studied. Phosphorus diffuses in silicon with barriers of 3.68 and 3.43 eV attributed to diffusion via an interstitial mechanism in the neutral and singly positive charge states respectively [75]. The interstitial- and vacancy-mediated mechanisms have been studied with modelling methods, and it is suggested that while the interstitial-mediated mechanism is dominant for most conditions, the vacancy-mediated mechanism may play an important role in heavily doped regions, where the charge states of the dopant and vacancy are compatible [63]. Arsenic diffusion was found from experiment to proceed with a barrier of 4.20 eV, attributed primarily to the vacancy-mediated mechanism [75].

1.5 Aims and Chapter Summaries

The work presented in this thesis aims to expand and extend the knowledge of defect behaviour in germanium and silicon. It has been of particular interest to investigate dopant related defects and dopant diffusion in germanium, but interest has also been found in studying intrinsic defects in germanium and some dopant related defects in silicon. Comparison of results for the two materials will form a significant part of the discussions sections of the proceeding Chapters. The remainder of the thesis will be divided up a follows:

Chapter 2: The work presented here has been performed using the local density approximation (LDA) under density functional theory (DFT). This chapter discusses the background of this theory starting with the Schrödinger equation for a many body system, and leading to the DFT.

Chapter 3: This chapter discusses the methods used in applying the theory presented in Chapter 2 to research problems. Details of how the code used implements DFT will be discussed, along with the methods used to calculate experimentally observable results and the specifics of the methods used in later chapters.

Chapter 4: Theoretical modelling work, while sometimes useful in isolation, is at its most enlightening when used to predict or explain experimental results. This Chapter details the experimental methods used in the various studies reported in later chapters. As well as an overview of the methods used, an example of application is included for each method discussed.

Chapter 5: Intrinsic point defects are the most fundamental lattice defects in any crystalline material. In germanium, the vacancy is the dominant defect, with the self-interstitial only recently coming under similar scrutiny. This Chapter details studies performed on the annealing behaviour of the divacancy in germanium, and the electrical properties and formation energies of larger vacancy clusters. Also discussed are calculations of the stable structure and migration paths for the self-interstitial.

Chapter 6: Dopant-related defects play a very important role in device performance in any semiconductor material. They can change the electrical properties of the dopants, reducing the carrier concentration in doped regions, and can enhance dopant diffusion, deepening junctions and diluting dopant concentrations. This Chapter describes work on the electrical and formation energies of a family of dopant-vacancy related defects in silicon and germanium.

Chapter 7: Dopant diffusion is an important process in semiconductor devices. As well as broadening sharp and shallow junction edges, significant out-diffusion of dopants can reduce carrier concentration in junction regions. Also of significant interest is the difference in diffusion properties between boron and phosphorus, commonly used as *p*- and *n*-type dopants, respectively, and why the differences seem to be reversed between silicon and germanium devices. This Chapter presents in depth studies of diffusion mechanics for both dopants in germanium, confirming and extending the present understanding, and discusses how the difference in mediating species between the dopants can explain the differences in relative diffusion between silicon and germanium devices.

Chapter 2

Theory Background

2.1 The Many Body Problem

The Schrödinger equation, the basis for all quantum mechanical investigations, is analytically soluble only for a very limited number of systems. In classical mechanics, the interactions of systems involving three or more bodies are known to produce chaotic results whereby a minor change in initial conditions can lead to a very significant difference in long-term behaviour. Similar problems are encountered in the quantum regime, and finding analytical solutions to the Schrödinger equation for any system involving three or more interacting particles is similarly impossible.

If no external fields are present, the Schrödinger equation takes the form

$$\hat{\mathcal{H}}\Psi_i = E_i\Psi_i \tag{2.1}$$

where $\hat{\mathcal{H}}$ is the many-body Hamiltonian, Ψ_i is the many-body wavefunction for the energy level of the system having energy E_i. $\hat{\mathcal{H}}$ expands to give

$$\hat{\mathcal{H}} = \hat{\mathcal{T}}_e + \hat{\mathcal{T}}_N + \hat{\mathcal{V}}_{e-e} + \hat{\mathcal{V}}_{N-N} + \hat{\mathcal{V}}_{e-N} \tag{2.2}$$

where $\hat{\mathcal{T}}_{e,N}$ are the electron and nucleus kinetic energy operators, and $\hat{\mathcal{V}}_{x-x}$ are the potential energy operators due to the interactions of the indicated species in the system. For this chapter, the atomic unit (a.u.) system will be used, in which the values of $\hbar$, e, m_e, and $4\pi\epsilon_0$ are defined as unity. The atomic unit of length is then 0.529 Å, and that of energy is 27.211 eV. The Hamiltonian then becomes

$$\begin{aligned}\hat{\mathcal{H}} &= -\frac{1}{2}\sum_{\mu=1}^{X_e}\nabla_\mu^2 - \sum_{\alpha=1}^{X_N}\frac{1}{2M_\alpha}\nabla_\alpha^2 + \frac{1}{2}\sum_{\mu\neq\nu}^{X_e}\frac{1}{|\mathbf{r}_\mu - \mathbf{r}_\nu|} - \sum_{\mu,\alpha}^{X_e,X_N}\frac{Z_\alpha}{|\mathbf{r}_\mu - \mathbf{R}_\alpha|} \\ &\quad + \frac{1}{2}\sum_{\alpha\neq\beta}^{X_N}\frac{Z_\alpha Z_\beta}{|\mathbf{R}_\alpha - \mathbf{R}_\beta|} \end{aligned} \tag{2.3}$$

where $M_\alpha, \mathbf{R}_\alpha$ and Z_α are the mass, position and charge of the α^{th} nucleus, $\mathbf{r}_\mu$ is the position of the μ^{th} electron, and $X_{e,N}$ is the total number of electrons and nuclei in the system, respectively.

Finally, the wavefunction Ψ_i is a function of nucleus position and electron position and spin (s_μ) co-ordinates.

$$\Psi_i \equiv \Psi_i\left(\mathbf{R}_1, \mathbf{R}_2 \ldots, \mathbf{R}_{X_N}, \mathbf{r}_1, s_1, \mathbf{r}_2, s_2 \ldots, \mathbf{r}_{X_e}, s_{X_e}\right) \tag{2.4}$$

For any but the smallest systems, no analytical solution to this problem exists, and for a crystal sample with hundreds of nuclei and thousands of electrons, the computational resources required to achieve a direct numerical solution would be tremendous. In order to usefully solve the problem, then, a series of approximations must be employed.

2.1.1 Born-Oppenheimer Approximation

The first approximation commonly applied to quantum mechanical many body problems is the Born-Oppenheimer Approximation [76]. This consists of the argument that, due to the difference of masses between the nuclei and electrons, the motion of the electrons and nuclei can be decoupled. In this methodology, the electrons are assumed to react instantly to any change in the nuclei positions, and the wavefunction can be rewritten as

$$\Psi\left(\mathbf{R},\mathbf{r}\right)=\chi\left(\mathbf{R}\right)\psi_{\mathbf{R}}\left(\mathbf{r}\right) \tag{2.5}$$

where **r** is now taken to encompass all electron spatial and spin co-ordinates, while **R** covers all the nuclei co-ordinates. Equation 2.1 can then be rewritten as separate electron and nuclei equations:

$$\begin{aligned}\left[\hat{\mathcal{T}}_N+\hat{\mathcal{V}}_{N-N}\right]\chi\left(\mathbf{R}\right) &= E_N\chi\left(\mathbf{R}\right) & (2.6)\\ \left[\hat{\mathcal{T}}_e+\hat{\mathcal{V}}_{e-e}+\hat{\mathcal{V}}_{e-N}\right]\psi_{\mathbf{R}}\left(\mathbf{r}\right) &= E_e\psi_{\mathbf{R}}\left(\mathbf{r}\right) & (2.7)\end{aligned}$$

where ψ and χ are separate all electron and all nucleus wavefunctions. The Schrödinger equation for the entire system is then written as

$$\begin{aligned}\hat{\mathcal{H}}\chi\left(\mathbf{R}\right)\psi_{\mathbf{R}}\left(\mathbf{r}\right) &= \left(E_N+E_e\right)\chi\left(\mathbf{R}\right)\psi_{\mathbf{R}}\left(\mathbf{r}\right)-\sum_{\alpha}^{X_N}\frac{1}{2M_\alpha}\left[\chi\left(\mathbf{R}\right)\nabla_\alpha^2\psi_{\mathbf{R}}\left(\mathbf{r}\right)\right.\\ &\left.+2\nabla_\alpha\psi_{\mathbf{R}}\left(\mathbf{r}\right)\nabla_\alpha\chi\left(\mathbf{R}\right)\right] \qquad (2.8)\end{aligned}$$

The second term is significant only in a system in which there is strong electron-nucleus coupling. The strong coupling leads to a large value for $\nabla_\alpha\psi_{\mathbf{R}}\left(\mathbf{r}\right)$ which can overcome the large value of M_α in the denominator. In these cases, electron-phonon interactions need to be considered, but in most cases the second term can be neglected, leading to a Schrödinger equation where the product $\chi\left(\mathbf{R}\right)\psi_{\mathbf{R}}\left(\mathbf{r}\right)$ is the eigenfunction and the sum of independent energy eigenvalues E_N+E_e is the energy eigenvalue for the system.

$$\hat{\mathcal{H}}\chi\left(\mathbf{R}\right)\psi_{\mathbf{R}}\left(\mathbf{r}\right)=\left(E_N+E_e\right)\chi\left(\mathbf{R}\right)\psi_{\mathbf{R}}\left(\mathbf{r}\right) \tag{2.9}$$

For the fully decoupled electron problem with fixed nuclear positions, the Schrödinger equation is then

$$\left[\hat{\mathcal{T}}_e+\hat{\mathcal{V}}_{e-e}+\hat{\mathcal{V}}_{e-N}\right]\psi\left(\mathbf{r}\right) = E_e\psi\left(\mathbf{r}\right)$$

$$= \left[-\frac{1}{2} \sum_{\mu=1}^{X_e} \nabla_\nu^2 + \frac{1}{2} \sum_{\mu \neq \nu}^{X_e} \frac{1}{|\mathbf{r}_\mu - \mathbf{r}_\nu|} - \sum_{\mu,\alpha}^{X_e,X_N} \frac{Z_\alpha}{|\mathbf{r}_\mu - \mathbf{R}_\alpha|} \right] \psi(\mathbf{r}) \tag{2.10}$$

2.1.2 Variational Principle

Equation 2.10 can be solved by integration over a discreet grid, and also through use of the variational principle. As the latter is the method used in almost all calculations to obtain the ground-state energy of an ensemble of atoms, it is the method which will be discussed here.

In this method, a subspace of the associated Hilbert space, described as $\{\phi_1, \ldots, \phi_M\}$, is chosen to form an approximation Ψ_{app} to the total ground-state wavefunction Ψ_0 by the equation

$$\Psi_0 \simeq \Psi_{\text{app}} = \sum_i^M c_i \phi_i. \tag{2.11}$$

The corresponding approximation of the ground-state energy E_{app} can be calculated as the expectation value of E given by Ψ_{app}:

$$\begin{aligned} E_{\text{app}} &= \frac{\langle \Psi_{\text{app}} | \hat{\mathcal{H}} | \Psi_{\text{app}} \rangle}{\langle \Psi_{\text{app}} | \Psi_{\text{app}} \rangle} \\ &= \frac{\sum_{i,j}^M c_i^* c_j \langle \phi_i | \hat{\mathcal{H}} | \phi_j \rangle}{\sum_{i,j}^M c_i^* c_j \langle \phi_i | \phi_j \rangle} \\ &= \frac{\sum_{i,j}^M c_i^* c_j H_{ij}}{\sum_{i,j}^M c_i^* c_j S_{ij}} \end{aligned} \tag{2.12}$$

where H_{ij} and S_{ij} are the Hamiltonian and overlap matrix elements, respectively. By including the condition that the derivative of E_{app} with respect to c_i must vanish for stationary states, it can be shown that

$$\sum_{j=1}^{M} \left(H_{ij} - E_{\mathrm{app}} S_{ij}\right) c_j = 0 \tag{2.13}$$

for all i, which can be generalised to the matrix eigenvalue equation

$$\mathsf{H} \cdot \mathbf{c} = E_{\mathrm{app}} \mathsf{S} \cdot \mathbf{c} \tag{2.14}$$

The Rayleigh-Ritz variational principle [77] states that the lowest eigenvalue of this equation will be equal or greater than the true ground-state energy, and that including more basis functions ϕ_i will improve the approximation asymptotically toward Ψ_0 and E_0.

Theorem 1 (Variational Principle)**.** *The energy E_{app} calculated from an approximate form of the wavefunction Ψ_{app} is an upper bound for the true value of the ground-state energy E_0. Fully minimising the functional $E[\Psi]$ with respect to the basis functions will yield E_0:*

$$E_0 = \min_{\Psi} E[\Psi] \tag{2.15}$$

2.1.3 Hartree's Method

The electronic Schrödinger equation given in Equation 2.10 still contains a term involving electron-electron interactions, $\hat{\mathcal{V}}_{e-e}$. In order to allow separation of variables, Hartree proposed modelling each electron as interacting only with an averaged electron density, rather than every other individual electron. The total electronic wavefunction $\psi(\mathbf{r})$ can then be rewritten as a product of single electron wavefunctions [78]

$$\psi(\mathbf{r}) = \psi_1(\mathbf{r}_1)\psi_2(\mathbf{r}_2)\ldots\psi_{X_e}(\mathbf{r}_{X_e}) = \prod_{\nu}^{X_e} \psi_\nu(\mathbf{r}_\nu). \tag{2.16}$$

From this, it is possible to write

$$\begin{aligned}\langle\psi|\psi\rangle &= \int\int \psi^*(\mathbf{r}')\psi(\mathbf{r})d^3r'd^3r = \prod_{\nu}^{X_e}\int \psi_\nu^*(\mathbf{r}_\nu)\psi_\nu(\mathbf{r}_\nu)d^3r_\nu &(2.17)\\ \langle\psi|\hat{\mathcal{H}}|\psi\rangle &= \prod_{\nu}^{X_e}\int \psi_\nu^*(\mathbf{r}_\nu)\left[-\frac{1}{2}\nabla_\nu^2 + \hat{\mathcal{V}}_{e-N}(\mathbf{r}_\nu)\right]\psi_\nu(\mathbf{r}_\nu)d^3r_\nu \\ &+\frac{1}{2}\prod_{\mu\nu}\int\int \frac{1}{|\mathbf{r}_\mu - \mathbf{r}_\nu|}\left|\psi_\mu(\mathbf{r}_\mu)\right|^2\left|\psi_\nu(\mathbf{r}_\nu)\right|^2 d^3r_\nu d^3r_\mu. &(2.18)\end{aligned}$$

Using these equations to construct an equation for the expectation value E^H leads to

$$\hat{\mathcal{H}}_H\psi_\nu(\mathbf{r}) = E_\nu^H\psi_\nu \tag{2.19}$$

with

$$\hat{\mathcal{H}}_H = -\frac{1}{2}\nabla^2 - \sum_{\alpha}^{X_N}\frac{Z_\alpha}{|\mathbf{r}-\mathbf{R}_\alpha|} - \int\frac{\rho(\mathbf{r}')}{|\mathbf{r}-\mathbf{r}'|}d^3r' \tag{2.20}$$

where $\rho(\mathbf{r}')$ is the electronic charge density given by

$$\rho(\mathbf{r}') = -\sum_{\nu}^{X_e}\left|\psi_\nu(\mathbf{r}')\right|^2. \tag{2.21}$$

When using the Hartree method, a set of ψ_ν are initially chosen to approximate the electron wavefunctions of the system. These wavefunctions are then used to calculate the electron density and another set of wavefunctions ψ_ν' are found. Thus by an iterative process, it is possible to find a self-consistent set of electron wavefunctions and from them the electronic contribution to the energy.

Despite this utility, the Hartree wavefunctions are unphysical, as they are invariant under the exchange of particles and do not prohibit electrons from sharing wavefunctions. This contravenes the Pauli exclusion principle, and an extension to the Hartree method is required to account for the fermion nature of the electrons.

2.1.4 Hartree-Fock Theory

Both Fock [79, 80] and Slater [81] independently developed an adaptation to Hartree's approach to take into account the fermion nature of the electrons. In this case, the total wavefunction must be antisymmetric with respect to exchange of electrons, and this can be achieved by writing $\psi(\mathbf{r})$ as

$$\psi_{\mathrm{SD}}(\mathbf{r}_1,\mathbf{r}_2,\ldots,\mathbf{r}_{X_e}) = \frac{1}{\sqrt{X_e!}}\begin{vmatrix} \psi_1(\mathbf{r}_1) & \cdots & \psi_{X_e}(\mathbf{r}_1) \\ \vdots & \ddots & \vdots \\ \psi_1(\mathbf{r}_{X_e}) & \cdots & \psi_{X_e}(\mathbf{r}_{X_e}) \end{vmatrix} \tag{2.22}$$

ie a Slater determinant. As above, ψ_i are a series of orthonormal single-electron wavefunctions, but in this case, the exchange of any two electrons changes the sign of the resulting wavefunction and if any two electrons were to share their co-ordinates, the determinant would become zero.

Using ψ_{SD} as the solution to the purely electronic Schrödinger equation (Equation 2.10), an equation of the form

$$\hat{\mathcal{F}}|\psi_\nu\rangle = \epsilon_\nu|\psi_\nu\rangle \tag{2.23}$$

is obtained, where $\hat{\mathcal{F}}$ is the Fock operator:

$$\begin{aligned}\hat{\mathcal{F}}\psi_\nu(\mathbf{r}) &= \left[-\frac{1}{2}\nabla^2 - \sum_\alpha \frac{Z_\alpha}{|\mathbf{r}-\mathbf{R}_\alpha|}\right]\psi_\nu(\mathbf{r}) + \sum_{\mu=1}^{X_e}\int |\psi_\mu(\mathbf{r}')|^2 \frac{1}{|\mathbf{r}-\mathbf{r}'|}\psi_\nu(\mathbf{r})d^3r' \\ &\quad - \sum_{\mu=1}^{X_e}\int \psi_\mu^*(\mathbf{r}')\frac{1}{|\mathbf{r}-\mathbf{r}'|}\psi_\nu(\mathbf{r}')\psi_\mu(\mathbf{r})d^3r'. \end{aligned}\tag{2.24}$$

Alternatively, the equation can be split into component terms:

$$\hat{\mathcal{F}} = \hat{h} + \hat{J} - \hat{K}. \tag{2.25}$$

$\hat{h}$ is the term in square brackets, and represents the Hamiltonian of a single electron in the potential due to the nuclei, $\hat{J}$ is the Coulomb operator,

$$\hat{J}\psi_\nu(\mathbf{r}) = \sum_\mu \hat{J}_\mu\psi_\nu(\mathbf{r}) = \sum_{\mu=1}^{X_e}\int |\psi_\mu(\mathbf{r}')|^2\frac{1}{|\mathbf{r}-\mathbf{r}'|}\psi_\nu(\mathbf{r})d^3r' \tag{2.26}$$

and $\hat{K}$ is named the exchange operator, and is given by

$$\hat{K}\psi_\nu(\mathbf{r}) = \sum_\mu \hat{K}_\mu\psi_\nu(\mathbf{r}) = \sum_{\mu=1}^{X_e}\int \psi_\mu^*(\mathbf{r}')\frac{1}{|\mathbf{r}-\mathbf{r}'|}\psi_\nu(\mathbf{r}')\psi_\mu(\mathbf{r})d^3r'. \tag{2.27}$$

Representing the operators as matrices, as above, yields

$$\mathsf{F} \cdot \mathbf{c} = \epsilon \mathsf{S} \cdot \mathbf{c} \tag{2.28}$$

where $F_{i,j} = \langle \psi_i | \hat{\mathcal{F}} | \psi_j \rangle, c_i = \langle \psi_i | \psi_{\mathrm{SD}} \rangle$ and S is the overlap matrix $\langle \psi_i | \psi_j \rangle$. This is known as the Roothaan equation [82]. As with the Hartree theory, this equation can be solved by a self-consistant interactive process leading to convergence of the total energy. The eigenvalues ϵ of the converged solution have a physical significance realised by Koopmans [83].

Theorem 2 (Koopmans' Theorem)**.** *Assuming that the eigenstates* $\mathbf{c}$ *do not vary significantly after the removal of one electron from the system, the ionisation energy of the* m^{th} *electron is given by* -ϵ_m.

Even with the enhancements here, the Hartree-Fock theory is still flawed. The correlation energy except for exchange is assumed to be zero, which leads, for example, to a zero density of states at the Fermi level of a homogeneous electron gas.

A number of methods have been proposed to incorporate correlation effects into the Hartree-Fock theory. The configuration interaction method is an example of such, in which the wavefunction is described by a linear combination of Slater determinants, as opposed to the single determinant described above [84]. This yields exact many-electron eigenstates and eigenvalues, but the computational resources required to perform the calculations are very large, and the method quickly becomes impractical as the number of atoms involved moves past a few tens.

2.2 Density Functional Theory

Density functional theory (DFT) is a method wherein a variational principle is applied with the variable being the electron density $n(\mathbf{r})$ of the ground state of the system. This method leads to the total energy of the system being a functional of n rather than of the all-electron wave-function as described above [85, 86]. In fact, the fundamental variable for determining the properties of the entire system becomes

n, in place of X_e and the external potential v_{ext} in the Hartree-Fock theory. This is known as the first Hohenberg-Kohn theorem [85].

Theorem 3 (First Hohenberg-Kohn theorem)**.** *The external potential is described, to within a trivial additive constant, by the electron density* $n(\mathbf{r})$*.*

As n therefore defines both X_e and v_{ext}, it must also define the ground state wavefunction and therefore the total energy.

The second Hohemberg-Kohn theorem states that for a charge density n',

$$\begin{aligned} E[n'] &= F[n'] + \int v_{\text{ext}}(\mathbf{r}) n'(\mathbf{r}) d^3r && (2.29) \\ &\geq E[n] && (2.30) \end{aligned}$$

where F is a universal functional accounting for the electron kinetic energy, electron correlation and exchange correlation. [85]

Theorem 4 (Second Hohenberg-Kohn theorem)**.** *For a trial density,* $n'(\mathbf{r})$ *such that* $n'(\mathbf{r}) > 0$ *and* $\int n'(\mathbf{r}) d^3r = X_e$*,*

$$E[n'] \geq E_0 \tag{2.31}$$

This is very similar to the Raleigh-Ritz variational principle, with the charge density, rather than wave function, being the variable. The total energy, $E[n]$ is defined by the equation

$$E[n] = T_e[\psi] + V_{e-e}[n] + V_{e-N}[n] + E_{XC}[n] \tag{2.32}$$

where $\psi(\mathbf{r}, s)$ is a set of orthonormal spin orbitals linked to n via the relationship

$$n(\mathbf{r}) = \sum_{\lambda=1}^{X} \sum_{s} |\psi_\lambda(\mathbf{r}, s)|^2, \tag{2.33}$$

and the four terms are the electron kinetic energy

$$T_e[\psi] = \frac{1}{2} \sum_{\lambda,s} \int \psi_\lambda^*(\mathbf{r}, s) \nabla^2 \psi_\lambda(\mathbf{r}, s) d^3r, \tag{2.34}$$

the electron-electron potential energy

$$V_{e-e}[n] = \frac{1}{2} \int \frac{n(\mathbf{r}) n(\mathbf{r'})}{|\mathbf{r} - \mathbf{r}|'} d^3r d^3r', \tag{2.35}$$

the electron-nucleus potential energy

$$V_{e-N}(n) = -\int n(\mathbf{r}) \sum_{\alpha} \frac{Z_\alpha}{|\mathbf{r} - \mathbf{R}_\alpha|} d^3r, \tag{2.36}$$

and the exchange correlation functional E_{XC} the form of which will be discussed later.

2.2.1 Kohn-Sham Equations

Using the above equations, the energy can be determined for a charge density formed by summing the probability density of a set of orthonormal spin-orbitals. The process of determining these orbitals is usually performed using the Kohn-Sham equations.

Using the variational principle and the orthonormal property of the spin-orbitals, the quantity

$$E - \sum_{\lambda,s} \epsilon_{\lambda,s} \left[\int |\psi_\lambda(\mathbf{r}, s)|^2 d^3r - 1 \right] \tag{2.37}$$

may be minimised with respect to $\epsilon_{\lambda,s}$ and ψ_λ. This done, a series of one electron Schrödinger equations is obtained:

$$\left[-\frac{1}{2}\nabla^2 + \int \frac{n(\mathbf{r}')}{|\mathbf{r} - \mathbf{r}'|} d^3r' - \sum_{\alpha} \frac{Z_\alpha}{|\mathbf{r} - \mathbf{R}_\alpha|} + \frac{\partial E_{XC}[n]}{\partial n(\mathbf{r})} \right] \psi_\lambda(\mathbf{r}) = \epsilon_\lambda \psi_\lambda(\mathbf{r}), \tag{2.38}$$

where the charge density is obtained as above:

$$n(\mathbf{r}) = \sum_{\lambda=1}^{X} \sum_{s} |\psi_\lambda(\mathbf{r}, s)|^2. \tag{2.39}$$

Equations 2.38 and 2.39 are known as the Kohn-Sham equations, and are solved via an interactive self-consistent method. First an initial charge density is used in Equation 2.38 to generate a set of spin-orbitals, which are then used to calculate a new charge density using Equation 2.39. This new charge density can then be fed directly back into Equation 2.38 to generate the next set of spin-orbitals. At each step, the total energy of the system is calculated, and the process continues until the difference between the energy calculated at two consecutive iterations is considered negligible.

One further refinement of the process is often included to speed the convergence. The process above usually results in a charge density that oscillates about an optimum solution. By using a input charge density at each iteration that is some combination of the input and output densities for the previous iteration, this oscillation is damped and the number of iterations required to achieve convergence is reduced.

2.2.2 Exchange and Correlation Energies

The value of the exchange correlation energy E_{XC} is one of the more challenging problems for the application of density functional theory. Different approaches are used in different implementations, and their failings are usually manifest in poor agreement with experimentally determined band structure parameters such as band gap and effective mass. Ground state properties such as bulk modulus and lattice constant are, however, usually found to agree well with experiment for even quite simple approximations.

The most common approximation used in implementing DFT is the local density approximation (LDA) or local spin density approximation (LSDA), a generalisation of LDA for systems with a net spin [86, 87, 88]. In these approaches, it is assumed that the exchange correlation energy is local and can be decomposed into an exchange energy and a correlation energy. In the notation of the LSDA:

$$E_{XC}[n\uparrow, n\downarrow] = E_X[n\uparrow, n\downarrow] + E_C[n\uparrow, n\downarrow] \tag{2.40}$$

where the ‘up’ and ‘down’ spin densities are calculated through Equation 2.39, restricting s to be one or other spin rather than summing the contributions.

Restricting the calculation to a local density allows the treatment of each point in the system as a homogeneous electron gas with the local density. In this approximation, the exchange energy is known exactly [88]:

$$E_X[n\uparrow, n\downarrow] = -\frac{3}{2}\left(\frac{3}{4\pi}\right)^{1/3}\left(n\uparrow^{4/3} + n\downarrow^{4/3}\right). \tag{2.41}$$

The correlation energy is, however, much more complicated, and there is no single analytical solution which can be used. For high charge densities, perturbation theory has been used to give an expression for E_C [87], while for low density, a quantum-Monte-Carlo approach using Green functions yields a different expression [89, 90]. It is possible, though, to construct a parameterised expression from the numerical results of these two extremes [87, 91, 92], and this is what is used in DFT implementations.

While the LDA is an attractive and useful method for calculating the exchange-correlation energy, it suffers from an underestimation of the energy of excited states. This leads directly to a strong underestimation of the band-gap of semiconductors, an important problem for any calculation involving defects which introduce energy levels into the gap. The calculated band gap can be expressed as the difference between the energies of the highest occupied and lowest unoccupied Kohn-Sham levels:

$$E_g = E_{\mathrm{LU}} - E_{\mathrm{HO}} - \Delta_{XC} \tag{2.42}$$

where Δ_{XC} is the discontinuity of the exchange correlation potential at the Fermi level as a function of the occupation number. The band-gap underestimation stems from both a self-interaction error inherent in the LDA potential and the vanishing of Δ_{XC} [93]. In germanium, this problem is especially acute as the small experimental band-gap combined with the LDA underestimation leads to a predicted gap that is either negligible or in some cases zero or even negative [94].

Another approximation used in some implementations for E_{XC} is the generalised gradient approximation (GGA). In this approximation, E_{XC} is expanded to the first order, including terms of ∇n at an additional computational expense [95, 96, 97].

2.2.3 Pseudopotentials

When modelling electrons in solids with DFT, complications arise due to the differences in electron behaviour close to the nucleus compared with behaviour at interstitial positions far from atom centres. Of particular difficulty is the rapid spatial oscillation of the wavefunctions close to the nuclei, requiring a large number of basis functions to model accurately, therefore rapidly increasing the computational resources required. Also, the energy calculated in all-electron simulations is very large, with correspondingly large errors when calculations require the energy difference between two comparable systems.

A common approach to solving these problems involves dividing the electrons into *core* and *valence* sets, and treating the two with different approaches. Potentials are calculated not for the bare atomic nuclei but for ions consisting of the nuclei plus the core electrons, taking into account the screening of the nuclei by the core electrons resulting in a smoother potential for the valence electrons. These *pseudopotentials* rely on a few approximations/assumptions:

The all-electron Coulomb operator must be able to be decomposed into two parts - one for the core electrons and one for the valence electrons.

The core must be unaffected by its environment. This is called the *frozen core approximation*.

There must be negligible overlap between the core and valence states. This allows the decomposition of E_{XC} into two parts. The violation of this assumption does not preclude the use of the pseudopotentials, but it does require compensation. Non-linear core correlation is sometimes used to improve the accuracy of calculations [98].

In solid state calculations, the use of pseudopotentials has another important benefit, as it removes the need to calculate either wavefunctions or charge densities due to the core electrons, dramatically reducing the resources required per atom of the material and allowing significantly larger systems to be studied. Also, in any calculation involving heavy atoms where relativistic effects become important for the core states, these effects can be taken into account in the calculation of the pseudopotentials while allowing the treatment of the valence electrons to be entirely non-relativistic.

There are various methods which can be employed to calculate pseudopotentials. Those of Bachelet, Hamann and Schlüter [99] are quite commonly used, as are those of Troullier-Martins [100] and Hartwigsen, Goedecker and Hutter [101].

2.2.4 Choice of Boundary Conditions

When implementing DFT, the choice of boundary conditions used in the calculations can be very important on the results calculated, as will be seen in many of the proceeding Chapters. There are two options for the treatment, periodic boundaries or boundaries to vacuum, commonly referred to as the supercell or cluster methodologies respectively.

In supercell calculations, the modelling is performed within a supercell of tens to hundreds of atoms with periodic boundary conditions that form an infinite perfect crystal in the case of an undistorted supercell. When a defect or defects are introduced into the supercell it forms a periodic array of defects. Supercell calculations have the advantage that defect energies thus calculated are independent of the location of the defect within the supercell. This then gives more reliable results for any calculation involving the comparison of energies of different defect structures, including migration calculations and calculations comparing different structures of the same defect.

In cluster calculations, the modelled sample consists of a nanoparticle of usually a few hundred atoms, with boundaries to vacuum. The surface bonds of the sample are often terminated with hydrogen atoms to minimise their effect on the calculations. In the cluster, compared with supercell calculations, there are no defect-defect interactions, but instead interactions between the surface of the cluster and the defect within must be considered. Modern computing facilities can allow for the use of large atomic clusters, which can minimise this effect, but defects still need to be kept away from the cluster surface to avoid significant interaction.

Cluster calculations can be more accurate under some conditions than supercell calculations, particularly when dealing with host material for which the LDA band-gap underestimation is critical. Quantum confinement in the cluster artificially raises the calculated band-gap of the material, with the gap found to decrease towards the supercell value with increasing cluster size [102]. This effect has been employed to compensate for the LDA band-gap underestimation as described for example in reference [103] and Section 5.3. It has also been suggested that Jahn-Teller distortions are strongly affected by defect-defect interaction in the supercell, and hence are more reliably calculated in the cluster where these interactions are absent [8].

A further complexity of the cluster methodology is the treatment of the surface of the cluster. This usually either involves preventing the motion of the outermost layer of crystal and hydrogen atoms or allowing them to relax with the rest of the cluster. The full relaxation method has been used in the past for example in references [104, 105, 106, 107, 108], while the fixed surface method has been used in references [5, 10, 109, 110]. Another technique that may be employed is the use of strained surface X-H bonds to tune the quantum confinement effect. It is possible to manipulate the strength of the quantum confinement through the position of the hydrogen atoms, tuning the calculated band gap to the experimental value. The effects of these methods on calculated properties of the divacancy are discussed in Section 5.3, and the fixed surface approach with relaxed X-H bond lengths has been used for the majority of the work of this thesis. The fixed surface is expected to reduce the effect of the surrounding vacuum on the system, as the surface provides the pressure normally exerted by the crystal, and, as it is a fixed volume calculation, it should be more accurate for calculations comparing the energy of different defect structures than the fully relaxed systems.

A comparison of the supercell and cluster methods as applied to the single and divacancy in silicon will be presented in Section 3.2

2.3 Chapter Summary

In this Chapter, the theoretical background underlying the work presented in the proceeding chapters has been discussed. Starting from the many body Schrödinger equation, the development of the theory up to the Density Functional Theory has been discussed. In the next Chapter, the application of this theory to the problems of later Chapters will be discussed.

Chapter 3

Theoretical Methods

3.1 AIMPro

The work presented in this thesis has been performed using a code known as the *Ab-initio Modelling Program*, or AIMPro [102, 111, 112]. The AIMPro code is capable of performing calculations in both the supercell and cluster methodologies with slightly different implementations for each.

3.1.1 Supercell AIMPro

In the supercell methodology, the wavefunctions and charge density must be periodic along the lattice vectors of the supercell. Due to this, some properties are more efficient to calculate in reciprocal space, so while AIMPro uses a basis set of localised orbitals to solve the Kohn-Sham equations, the charge density is still expanded as a series of plane waves, such that integrals of $n(\mathbf{k})$ can be solved by summing over the Brillouin Zone.

3.1.1.1 Real Space Basis Functions

The choice of basis set used to expand the Kohn-Sham wavefunctions and construct the Hamiltonian of the system is always a compromise between accuracy and cost. As such, there is no consensus on the best basis set to use for a given problem.

The basis sets are constructed to conform to Bloch's theorem as:

$$\psi_\lambda = \sum_i c_i^\lambda B_{\mathbf{k}i}(\mathbf{r}), \tag{3.1}$$

with

$$B_{\mathbf{k}i}(\mathbf{r}) = \frac{1}{\sqrt{N_L}} \sum_{n=1}^{N_L} \phi_i(\mathbf{r} - \mathbf{L}_n) e^{i\mathbf{k}.\mathbf{L}_n}, \tag{3.2}$$

where the sum is over all the N_L real space lattice vectors. In AIMPro, the basis functions ϕ_i are constructed by multiplying a polynomial by a Gaussian:

$$\phi_{i,n_1,n_2,n_3}(\mathbf{r}) = (x - R_{ix})^{n_1} (y - R_{iy})^{n_2} (z - R_{iz})^{n_3} e^{-\alpha_i(\mathbf{r}-\mathbf{R}_i)^2}, \tag{3.3}$$

where n_1, n_2 and n_3 are integers. If all are zero, the orbital is s-type. When one of the integers is one and the others zero, a p-type orbital results, while $n_1+n_2+n_3 = 2$ yields five d-type and one s-type orbitals. Throughout the calculations, the orbitals are atom centred, and move with the atoms as calculations proceed.

Many other implementations of DFT employ plane wave basis sets to model the electron wavefunctions. Gaussian orbitals offer a number of advantages over the plane wave sets, particularly in efficiency and flexibility. Plane wave basis sets require a large number of functions to model even relatively simple atoms - around 100 functions for Si, and even more for 'difficult' atoms with rapidly changing wavefunctions, for example carbon, nitrogen and oxygen. These are quite common impurities in both silicon and germanium, and the Gaussian basis sets can model them to fair accuracy with only 28 functions. Using atom-centred Gaussian orbitals also automatically devotes more coverage to regions of the sample with higher density while still allowing the addition of 'ghost' centres to increase coverage at bond centres or vacuum surfaces if the default orbital distribution proves insufficient to describe these regions. Finally, increasing the system size under this type of treatment produces a more sparse Hamiltonian matrix. However, there are drawbacks to this approach, most notably that the non-orthonormality of the Gaussian orbitals necessitates a more complex programme. It is also more costly to test convergence with basis set size, and numerical noise can become a problem if two or more Gaussian exponents are chosen too close together.

Exponents for the Gaussian orbitals are chosen by a variational method with the best exponents being those which minimise the total energy of a test system. Usually, the test system is more simple than the system being studied, for example the exponents for germanium and silicon are usually optimised for bulk material and the orbitals for dopant atoms are often optimised for isolated atoms rather than for the specific defect being studied. Convergence is tested by adding further functions to the basis set and repeating the optimisation.

It is possible with some systems to use a smaller basis set and still calculate the properties of a system to reasonable accuracy. Contracted basis functions of *d*-type or higher angular momentum are produced by combining a number of Gaussian orbitals:

$$\phi^{\text{cont}}_{i,lmn} = \sum_{n_1,n_2,n_3} c_{lmn,i,n_1,n_2,n_3} \phi_{i,n_1,n_2,n_3} \tag{3.4}$$

where coefficients $c_{i,lmn}$ are optimised for the model system, usually bulk material [113].

3.1.1.2 Reciprocal Space Basis Functions

In the supercell code, the charge density is approximated in a plane wave basis as

$$\tilde{n}(\mathbf{r}) = \sum_{\mathbf{G}} A_G e^{i\mathbf{G}.\mathbf{r}} \tag{3.5}$$

where the sum is over a set of **G** vectors within a cutoff energy

$$E_{\text{cut}} = \frac{1}{2} G^2_{\text{cut}}. \tag{3.6}$$

E_{cut} is chosen to be sufficient for $\tilde{n}$ to be converged to the value of n calculated from the Gaussian wavefunctions. The value required for this varies depending on the species in the system under investigation, with the more 'difficult' species requiring a larger cutoff energy. As this calculation is performed only for the charge density, not for every wave function, it does not add significantly to the computational effort of the simulation. From this plane wave representation, the charge density can be converted to a reciprocal space representation $n(\mathbf{k})$ fairly simply.

3.1.1.3 Integration over the Brillouin Zone

Once n has been represented in $\mathbf{k}$-space, integration of $n(\mathbf{k})$ can be performed to calculate properties such as the total energy of the system. The integration is performed numerically by summing over a set of $\mathbf{k}$ points using the method proposed by Baldereschi, Chadi and Cohen [114, 115]. AIMPro uses the sampling scheme for $\mathbf{k}$ space proposed by Monkhorst and Pack [116] which is used to produce a set of $\mathbf{k}$-points within the Brillouin zone. The symmetry of the supercell is then used to eliminate equivalent points leaving an irreducible set of points to be used in the calculations.

3.1.2 Cluster AIMPro

As in the supercell methodology, the wavefunctions for the cluster implementation are expanded with Gaussian basis sets. With a lack of periodicity, however, the charge density is constructed in terms of a density tensor b:

$$n_s(\mathbf{r}) = \sum_{i,j} b_{ijs}\phi_i(\mathbf{r}-\mathbf{R}_i)\phi_j(\mathbf{r}-\mathbf{R}_j) \tag{3.7}$$

where elements are given by

$$b_{ijs} = \sum_{\lambda_{occ}} \delta(s, s_\lambda) c_i^\lambda c_j^\lambda. \tag{3.8}$$

The sum is over the occupied levels of the system. The energy is calculated in the space defined by this basis. With Gaussian basis functions, it is possible to calculate the kinetic and pseudopotential energies analytically using the equations

$$T_{ij} = -\frac{1}{2}\int \phi_i(\mathbf{r}-\mathbf{R}_i)\nabla^2\phi_j(\mathbf{r}-\mathbf{R}_j)d^3r \tag{3.9}$$

and

$$V_{ij}^{\mathrm{ps}} = \int \phi_i(\mathbf{r}-\mathbf{R}_i)\sum_{\alpha} V_{\alpha}^{\mathrm{ps}}(\mathbf{r}-\mathbf{R}_{\alpha})\phi_j(\mathbf{r}-\mathbf{R}_j)d^3r. \tag{3.10}$$

3.1.2.1 Hartree, Exchange and Correlation Energies

To calculate the Hartree energy, a number of integrals must be performed scaling as $O(N^4)$ where N is the number of basis functions. Clearly for a moderately large system, this would lead to prohibitively complex calculations. In order to streamline the process, a number of approximations are used. Importantly, the integrals are reduced to a simpler form using an approximate form of the charge density. The charge density is expanded in terms of a set of auxiliary basis functions of up to *d*-type by default

$$\tilde{n}(\mathbf{r}) = \sum_{s,k} c_{s,k} g_k(\mathbf{r}) \tag{3.11}$$

where the coefficients are calculated analytically to minimise the error in the Hartree energy [111]. The Hartree energy then becomes simple to solve through analytical integration. As $g_k(\mathbf{r})$ are atom-centred Gaussian functions, the coefficients are easy to calculate, but still the time taken is quite significant, and is the most time-intensive step for small clusters. In larger clusters, the time taken does not continue to scale as quickly, since the overlap between Gaussians centred on distant atoms can be neglected.

The exchange and correlation energies are calculated using the intermediate approximation of charge density [111].

3.2 Cluster and Supercell Comparison

3.2.1 Introduction

The differences in the supercell and cluster methodologies lead to some potential issues with regards to the best choice of method for the problem at hand. As a test of the behaviour of the supercell procedure compared to that of the cluster, calculations were performed on the single vacancy (V) and divacancy (V_2) in silicon.

Calculations were undertaken in supercells containing 216 and 512 atoms in the perfect case ($\mathrm{Sup}_{216,512}$), and in clusters containing 181 Si and 116 H atoms (Clus_{297}), 329 Si and 172 H atoms (Clus_{501}) and 459 Si and 204 H atoms (Clus_{663}). Calculations were performed to find the migration barriers for the two defects using the nudged elastic band method (NEB) (Section 3.3.5) and the binding energy of V_2 (Section 3.3.3), all in the neutral charge state. Binding energies were calculated by both methods presented. For Vs separated within the same system, a separation of fourth neighbours along a $\langle 110\rangle$ chain was used, as this has been found to give converged results in previous theoretical calculations [38]. Calculations were also performed to find the first acceptor and donor levels for the two defects using the marker method (Section 3.3.4) with the experimentally known donor and acceptor levels of the PV defect at $E_v + 0.27$ and $E_c - 0.45$ eV respectively [117] as markers.

Experimental studies have previously found values for these properties. The migration barrier for neutral V has been found to be 0.45 eV [39], while that for V_2 has been observed to be 1.3 eV and independent of charge state. [36] The barrier for V_2 to dissociate has been given as *at least* 1.6 eV [36]. As this can be considered as a sum of the binding energy of the defect with the diffusion barrier of the single vacancy, the binding energy is expected to be at least 1.2 eV. The first donor level of V has been assigned to a trap at $E_v + 0.03$ eV [15] and the first donor and acceptor levels of V_2 have been assigned to levels at $E_v + 0.25$ eV and $E_c - 0.42$ eV [118]. These last two levels have however been attributed to a high-temperature structure averaged over three equivalent Jahn-Teller distorted configurations (Section 3.3.1.1), and so may have positions different from those of the low-temperature structure calculated with DFT.

3.2.2 Results

All the calculated results are given in Table 3.1. Across all the results, it can be seen that the convergence on supercell size seems to have been achieved by Sup_{216}, with the possible exception of the V_2 binding energy as calculated from separated vacancies. The change in the sign of the first donor level of both defects between the Sup_{216} and Sup_{512} supercells is not in itself significant, as the difference in level position is relatively small. For the cluster calculations, convergence on cluster size is seen to have been achieved for the smallest cluster for static properties - the binding energy and energy levels - while for the migration barriers, Clus_{501} is required to achieve convergence. For the V energy levels and migration barriers, it is clear that the supercell calculations give better results. For the V_2 energy levels, the cluster calculations seem to give results closer to the experimental values, but it is not clear how much this is due to the high temperature structural averaging effects mentioned above. Similarly, for the binding energy calculations the experimental data only gives a lower bound of 1.2 eV. As all the calculated results satisfy this condition, little more can be said save that the supercell results agree with previous theoretical results using a different code suggesting that vacancies can be considered separate at fourth neighbour positions along a $\langle 110 \rangle$ chain.

From this, it is seen that there is significant difference between the results of supercell and cluster calculations. The differences in energies calculated via the two methods is believed to be largely due to the quantum confinement effects in the cluster. This effect increases energies calculated in the cluster, widening the band gap and increasing the energies and energy differences calculated by the theory.

For calculations on defects in silicon, the band-gap underestimation in supercell calculations is not seen to lead to results far from expected values. This is understood to be due to the relatively wide band-gap in this material meaning that any defect-related energy levels are still able to fall within the reduced band-gap calculated from LDA. The quantum confinement effects in the cluster calculations then lead to overestimation of many calculated results, and so 216-atom supercells are used for all silicon-based calculations in the remainder of the thesis.

Table 3.1: Binding Energies of V_2 in silicon calculated from vacancies separated within the same system (V_{sep}) or isolated vacancies (V_{isl}) along with energy levels and neutral migration barriers calculated for V and V_2. All values are in eV and calculations have been performed in various cluster and supercell systems as indicated. Also included are experimental values for comparison.

Binding Energy	Sup_{216}	Sup_{512}	$Clus_{297}$	$Clus_{501}$	$Clus_{663}$	Experiment
V_{sep}	1.87	1.68	2.40	2.37	2.35	> 1.2
V_{isl}	1.72	1.74	-	-	-	

Energy Level	Sup_{216}	Sup_{512}	$Clus_{297}$	$Clus_{501}$	$Clus_{663}$	Experiment
$E_V(0/+)-E_v$	-0.05	0.04	0.20	0.10	0.10	0.03
$E_c-E_V(-/0)$	0.15	0.16	0.49	0.48	0.42	
$E_{V_2}(0/+)-E_v$	-0.02	0.03	0.17	0.16	0.15	0.25
$E_c-E_{V_2}(-/0)$	0.31	0.29	0.65	0.67	0.54	0.42

Migration Barrier	Sup_{216}	Sup_{512}	$Clus_{297}$	$Clus_{501}$	$Clus_{663}$	Experiment
V	0.24	0.34	1.56	0.86	0.82	0.45
V_2	1.22	1.17	2.65	1.80	1.76	1.3

In germanium, in contrast, the band-gap underestimation leads to defect-related energy levels lying within the bulk bands of the material, resulting in a calculated insensitivity of defect properties on charge state, as will be seen in Section 5.3. The quantum confinement effects present in cluster calculations compensate for the effects of underestimation in the supercell, allowing defect levels to again fall within the band gap. As such, it was decided to minimise the importance placed on germanium-based supercell calculations in these studies, and instead to focus on cluster calculations which do not suffer as severely from these problems. Therefore calculations on defects in germanium used 216-atom supercells where necessary and 501 or larger clusters where possible. This decision was subsequently supported by comparisons between supercell and cluster-focused calculations in Sections 5.3 and 7.3.

3.3 Calculation of Observables

AIMPro is able to calculate many physical properties which are in some way observable in experiment. This Section will discuss the methods used to calculate the values used in the studies forming the latter chapters of this thesis.

It is important to recognise that the Kohn-Sham DFT is a ground state theory and that the calculations of excited state properties, while possible, is non-trivial within this code. This comes from the fact that the Kohn-Sham eigenstates are not one-electron wavefunctions, but a set of basis functions which reproduce the correct ground state charge density. It is the case that the energy of the highest occupied Kohn-Sham state is directly related to the ionisation potential of the system [119], but the theory does not lend itself to elevated temperature calculations. This will be seen to be important in Section 7.4.

3.3.1 Defect Structure

While the structure of atomic defects is not often directly observable in experiment, the *symmetry* of the defects can be observed. In the case of this thesis, however, calculation of the defect structure is discussed solely as a prerequisite for later work.

The ground state structure of a system can be determined in DFT by minimising the forces acting on the atoms. For the initial atomic structure, a self-consistent charge density is calculated as described previously. The energy is calculated from the charge density and this is used to give the forces on each atom

$$\mathbf{F}_\alpha = -\nabla_\alpha E. \tag{3.12}$$

For plane-wave basis sets, this can be done using the Hellmann-Feynman theorem [120, 121]:

Theorem 5 (Hellmann-Feynman Theorem). *Let ζ be a parameter in the Hamiltonian $\hat{\mathcal{H}}$ and Ψ_ζ an eigenvalue of $\hat{\mathcal{H}}$. Then,*

$$\frac{\partial E}{\partial \zeta} = \langle \Psi | \frac{\partial \hat{\mathcal{H}}}{\partial \zeta} | \Psi \rangle. \tag{3.13}$$

However, for the Gaussian basis sets used in AIMPro, $\frac{\partial|\Psi\rangle}{\partial R} \neq 0$. This leads to extra terms called Paulay terms on evaluating the differential. The derivation of the forces in these systems is described in reference [111], and is significantly more time-consuming than for the plane-wave systems. In either case, though, the time taken to calculated forces is almost always smaller than the time taken to perform the self-consistency calculations.

The atoms are then moved by an amount calculated using the conjugated gradient algorithm [111] in the direction of the force. The process is repeated with the new structure, with the charge density calculation starting from the converged value from the previous iteration, the forces on the atoms calculated afresh. Iterations are continued until all forces in the system are considered negligible. This process is called *relaxing* the system.

This method of calculating defect structures has the advantage of being quick, but the energy minima found are local rather than global minima. Therefore, to find the most stable structure for any defect, several starting configurations are generally required. This is especially true for interstitial-type defects where a number of *meta-stable* structures may be found for a given defect - structures which are not the most energetically favourable but from which an energy barrier must be overcome to approach the more stable structures.

3.3.1.1 Symmetry Breaking and the Jahn-Teller Effect

Due to the use of the irreducible set of **k**-points discussed previously in Section 3.1.1.3, calculations on high-symmetry systems will require less computational effort than those on low-symmetry systems. It is also the case that systems in nature often tend to high symmetry arrangements, due to forces along the symmetry arrangements cancelling and resulting in such structures being either maxima or minima of the total energy. It can therefore be quite appealing to perform calculations in high symmetry systems. This, however, can often lead to erroneous results for reasons which will be discussed.

The first reason is a computational effect. Calculations performed on high symmetry systems cannot under DFT break this initial symmetry. This artificial constraint on the system can result in calculations finding unstable equilibrium structures. Such calculations are termed *symmetry constrained* and can be useful in some circumstances. They will be used in Section 5.3.

The second reason is a physical one, the Jahn-Teller effect. This occurs in systems where the symmetry has led to a number of degenerate energy states which are only partially occupied. In this case, breaking the symmetry of the system can result in the degeneracy being lifted as some of the states are pushed up in energy and others are lowered. As the electrons will naturally occupy the lower energy states, the reduction in electronic energy of the system resulting from the symmetry breaking may overcome any increase in energy from distorting the nuclei from their high-symmetry configuration resulting in the lower symmetry system being more stable.

Therefore, it is important to break the symmetry of any system either before performing any relaxations or after an initial relaxation to take advantage of the reduction in computational effort. This is most simply done by applying a small random displacement to a number of atoms in the system, typically those close to the defect being studied. In the proceeding Chapters this will be done for all relaxations not specified as being *symmetry constrained*.

3.3.2 Formation Energies

When studying defects, the concentration of the defects is one observable which can be measured in experiments. The concentration is dependent on a number of experimental parameters, such as the concentration of impurity atoms or temperature, for example, but is also determined by the defect's formation energy, which can be calculated. The formation energy of a defect can also be determined by experiment from an Arrhenius plot of the measured concentration as a function of temperature.

The equilibrium concentration of a defect is related to its formation energy as

$$C_D \propto e^{\left(-E_f(D)/k_BT\right)}, \tag{3.14}$$

where C_D is the concentration of defect D, k_B and T have their usual meanings and $E_f(D)$ is the formation energy of the defect, defined as the energy required to form the defect from a source of suitable atoms. The nature of the source can vary with the defect or process being investigated and will be discussed shortly.

In the neutral charge state, the formation energy is calculated as

$$E_f(D^0) = E(D^0) - \sum_i n_i\mu_i \tag{3.15}$$

where $E(D^0)$ is the total energy of a system containing the neutral defect, the sum is over all atomic species, n_i is the number of atoms of species i in the system and μ_i is the chemical potential of the species. The parameter μ_i is defined as the derivative of the Gibbs free energy G with respect to n_i at constant pressure and temperature [122, 123]. G is defined as

$$G = E + pV - TS \tag{3.16}$$

where p and V are the pressure and volume of the system, T and S are the temperature and entropy and E is the total energy as mentioned above. The derivatives of the last two terms are negligible in most solid-state calculations, and so the chemical potential becomes

$$\mu_i = \frac{\partial E}{\partial n_i} \tag{3.17}$$

which in turn leads to

$$E = \sum_i n_i\mu_i \tag{3.18}$$

for a system consisting of the source of the atomic species i. A suitable source for each species will depend on the nature of the process being studied, but for the work performed in this thesis, the source of atomic host atoms (Si or Ge) is taken to be a supercell of undistorted crystal, while dopant atoms are considered to be sourced as isolated, singly charged substitutional atoms already within the host crystal (B^- or P,As^+).

This requires, then, an additional consideration for charged systems. An extra term is needed in Equation 3.15 to take into account the electron chemical potential:

$$E_f(D^q) = E(D^q) - \sum_i n_i\mu_i + q\left(\mathrm{E_v} + \mu_e\right) \tag{3.19}$$

where q is the charge on the system, E_v is the energy of the valence band top and μ_e is the Fermi level measured from the top of the valence band. The term $(\mathrm{E_v} + \mu_e)$ is then the calculated energy of the Fermi level, or the electron chemical potential.

It should also be noted here that these equations hold true only for systems where different atoms of the same species can be considered equivalent. This is not the case for cluster calculations where host crystal atoms at different distances from the centre of the cluster will have different energies. Therefore, it is not possible to calculate formation energies in clusters, and energy comparison can be performed only between clusters containing the same number of atom in different arrangements.

3.3.3 Binding Energies

The binding energy of a defect AB with respect to its component defects A and B can be calculated from their respective formation energies as

$$E_b(AB^{q_{AB}}) = [E_f(A^{q_A}) + E_f(B^{q_B})] - E_f(AB^{q_{AB}}) \tag{3.20}$$

where $q_{AB} = q_A + q_B$. The binding energy is therefore defined as the energy required to separate the defects A and B. If the result is positive, the defect is bound against dissociation, at least in the charge states investigated.

Of note is that, in this form, the binding energy does not depend on the chemical potential of any impurity atoms involved in the reaction, or the electron chemical potential as these cancel out between the terms on the right hand side. So, for supercell calculations the binding energy becomes

$$E_b(AB^{q_{AB}}) = [E(A^{q_A}) + E(B^{q_B}) - n_h\mu_h] - E(AB^{q_{AB}}) \tag{3.21}$$

where n_H is the number of excess host atoms in the two supercells containing the defects A and B compared with the single supercell containing AB and μ_H is the chemical potential of the host species.

The binding energy of a defect can also be calculated in either supercells or clusters containing the defects A and B separated within the same system. In this case, the equation becomes

$$E_b(AB^{q_{AB}}) = E(A^{q_A} + B^{q_B}) - E(AB^{q_{AB}}) \tag{3.22}$$

where $E(A+B)$ is the total energy of the system containing the two separated component defects. In this case, both the total energies must be calculated in systems containing the same number of each atomic species, and the charge states q_A and q_B cannot be controlled. Still, in many systems it is possible to predict with confidence the charge states of the component defects from the total charge on the system.

3.3.4 Energy Levels

The energy levels of a defect are defined as the position of the Fermi level within the band gap where the defect switches from a charge of q to $q-1$ with increasing Fermi energy. Typically, the levels are written as $E(0/+)$, $E(-/0)$, $E(=/-)$ and so forth. Two methods are commonly used to calculate the energy levels - the formation energy method and the marker method.

3.3.4.1 Formation Energy Method

The charge-dependent formation energy of a defect, as calculated using Equation 3.19, can be used to calculate energy levels. From the definition above, the energy levels of a defect can be considered as the values of the Fermi energy where the most stable charge state changes.

Figure 3.1 shows a schematic diagram of the formation energies of a defect with a single acceptor and single donor level in the band gap. As the formation energy has a linear relationship with the Fermi level, it is simple to find the Fermi level position where the formation energies of two different charge states are equal. These positions should then coincide with the energy levels of the defect.

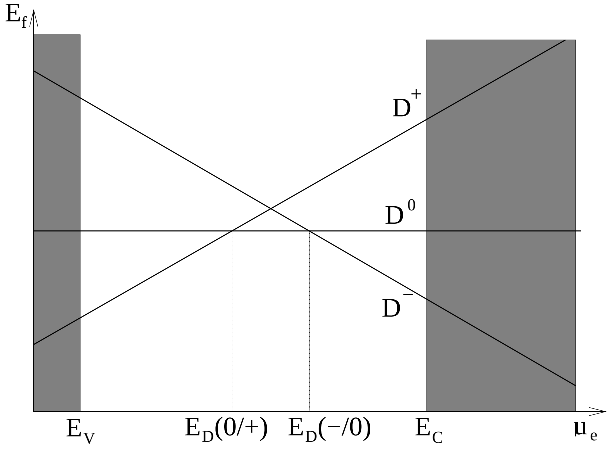

Figure 3.1: Schematic diagram depicting the formation energies E_f of three charge states of a defect D as a function of the Fermi level μ_e. The energy levels defined as shown are the value of the Fermi Energy where the most stable charge state changes.

For an Anderson negative-U defect [14], the relative position of two of the levels are reversed, leading to a situation where, for example, the donor level is above the acceptor level in the band gap, such that the neutral charge state is never the most favourable and a $(-/+)$ energy level can be observed in experiment.

This treatment can also be performed in a reversed order. If the formation energy of one charge state of the defect is known, as well as the energy levels, for example through marker method calculations, the formation energies of the other charged defect can be calculated. This method is used to calculate the formation energy of charged defects in Chapters 6 and 7

3.3.4.2 Marker Method

Another approach to the calculation of the energy levels of a defect is the marker method. This method has a few variations, most notably the *defect* marker method and *first principles* marker method. Both share the same basic principle, and differ only in the reference level used to measure energies against [104, 113, 124].

The basic concept of the marker method is that the ionisation energy of the defect being studied is compared with that of a system with known energy level. The

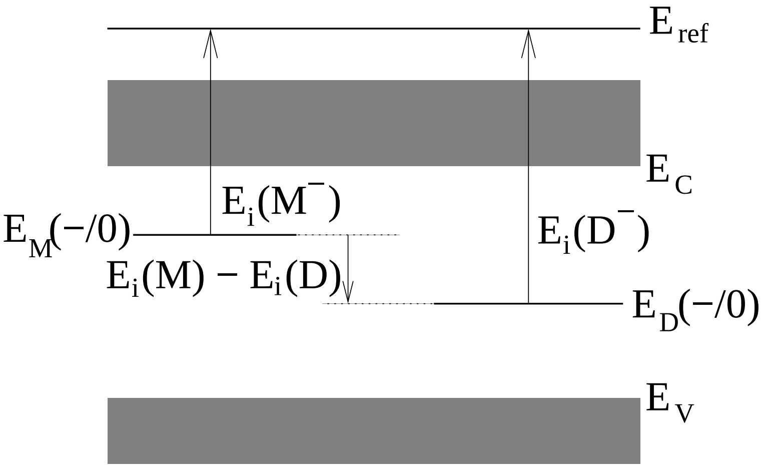

Figure 3.2: Schematic diagram showing the energies involved in defect marker method calculations. The ionisation energy is defined as the energy required to remove an electron from the system, and given a static reference energy E_{ref}, the difference in ionisation energy should be the difference in energy level.

ionisation energy is calculated as $E_i(X^{(q-1)}) = E(X^q) - E(X^{q-1})$ for both the defect D and the marker M and the difference in ionisation energies between the two systems is taken to be equal to the difference in their energy levels. That is, if it requires 0.1 eV more to remove an electron from the defect being studied than from the marker, then the defect's energy level is 0.1 eV below that of the marker. This is shown graphically in Figure 3.2 and can be expressed as

$$E_D\left((q-1)/q\right) = E_M\left((q-1)/q\right) + \left[E(M^q) - E(M^{q-1})\right] - \left[E(D^q) - E(D^{q-1})\right] \tag{3.23}$$

The two variants of the marker method are then different due to the choice of marker system. In the first principles marker method, the marker system is taken to be an undistorted crystal, with the single donor level being related to the top of the valence band and the single acceptor level being related to the conduction band minimum. This has the advantage that the results are completely *ab initio*, with no empirical data used, but it is not easy to justify applying this method to the second or third acceptor or donor levels, and in order to reference the defect level to the other side of the band gap, more common in experimental results, the experimental band gap must be used, removing the *ab initio* 'purity' of this method.

In the defect marker method, the reference level is taken as the electrical level of an experimentally well characterised defect. Ideally, the defect has a spatial extent and form that are similar to the defect being studied as well as having energy levels close to those of the defect being studied [113].

The marker method has the advantage of being easy to apply to the cluster methodology as well as supercell calculations, allowing circumvention of the problems associated with charged supercells in germanium. It also cancels to first order any systematic errors in the DFT implementation which are charge *or* structure dependent. As such it is the method which has been used throughout the studies discussed here, to avoid the use of the germanium supercell. A comparison of the two methods is given in Section 7.3.

3.3.5 Diffusion Barriers

Diffusion barriers and paths have been calculated by the Nudged Elastic Band (NEB) method. Broadly this method involves investigating a number of intermediate systems between an initial and final position, linked by virtual forces - the 'elastic bands' of the name. It is an efficient algorithm which can be applied successfully to large systems [125]. Two advances on the basic method are implemented in AIMPro, which will be discussed here - the *improved tangent* method and the *climbing image* method [126, 127].

3.3.5.1 Basic NEB

Before an NEB run can be started, the start and end points of a diffusion path must be defined. These are usually relaxed defect structures found as described in Section 3.3.1. From these configurations, a series of systems $\mathbf{R}_i$, $i = 0, ..., N$ is constructed to form a description of the path taken by the diffusion. Typically, this is done by linear interpolation between the initial and final configurations, though in some calculations it is necessary to insert an intermediate structure to break the symmetry of the path. In that case, the linear interpolation is performed between the start point and the mid point and between the mid point and the end point. This set of systems is termed the chain and the systems are termed images.

The images are linked through spring forces between each atom and its equivalent in adjacent images. The entire chain is then relaxed together with the initial and final structures remaining as fixed end points. The simplest approach to the relaxation is to minimise the function

$$S(\mathbf{R}_1, ..., \mathbf{R}_{N-1}) = \sum_{i=1}^{N-1} E(\mathbf{R}_i) + \sum_{i=1}^{N} \frac{k}{2}(\mathbf{R}_i - \mathbf{R}_{i-1})^2, \tag{3.24}$$

the sum of the energies of all the non-fixed images, including that due to the virtual elastic bands. The major disadvantages of this simple approach are that the spring forces tend to pull the path straight, cutting the corner of the true minimum energy path, and to cause the images to cluster near the usually low-energy end points leaving the saddle point region poorly described. These problems are solved by ‘nudging’ the images perpendicular to the local tangent of the path to encourage relaxation with respect to the true force in that direction.

The tangent to the path is given by the tangent vector

$$\mathbf{t}_i = \frac{\mathbf{R}_i - \mathbf{R}_{i-1}}{|\mathbf{R}_i - \mathbf{R}_{i-1}|} + \frac{\mathbf{R}_{i+1} - \mathbf{R}_i}{\mathbf{R}_{i+1} - \mathbf{R}_i}, \tag{3.25}$$

and the virtual spring forces are calculated by the three point method

$$F_i = k\left(|\mathbf{R}_{i+1} - \mathbf{R}_i| - |\mathbf{R}_i - \mathbf{R}_{i-1}|\right). \tag{3.26}$$

3.3.5.2 Improved Tangent NEB

The calculation of the tangent by Equation 3.25 can be problematic, causing the calculated path to be irregular and to fail to converge to the true lowest energy path in certain instances. In systems where the energy changes rapidly along the path but the force perpendicular to the force is weak, this becomes an important issue. One solution to this is to use an improved estimation for the tangent, defined either by the vector between the i^{th} image and its neighbour with higher energy, or by a weighted average of the vectors between the i^{th} image and its neighbours when the

i^{th} image has the higher energy [127]:

$$\mathbf{t}_i = \begin{cases} \mathbf{t}_i^+ & \text{if } E_{i+1} > E_i > E_{i-1} \\ \mathbf{t}_i^- & \text{if } E_{i-1} > E_i > E_{i+1} \\ \mathbf{t}_i^+|E_{i+1} - E_i| + \mathbf{t}_i^-|E_i - E_{i-1}| & \text{if } E_i > E_{i+1}, E_{i-1} \end{cases}, \tag{3.27}$$

where $E_i = E(\mathbf{R}_i)$, $\mathbf{t}_i^+ = (\mathbf{R}_{i+1} - \mathbf{R}_i)/|(\mathbf{R}_{i+1} - \mathbf{R}_i)|$ and $\mathbf{t}_i^- = (\mathbf{R}_i - \mathbf{R}_{i-1})/|(\mathbf{R}_i - \mathbf{R}_{i-1})|$. Provided that a sufficient number of images are used, this implementation of NEB is more stable and converges more easily to the true lowest energy path.

3.3.5.3 Climbing-image NEB

This implementation is designed to allow for an accurate description of the saddle point without requiring a large number of images to be used. It works by causing one of the images to climb along the path direction to reach the saddle point.

Starting with the regular NEB method, after a few iterations, the image with the highest energy is selected. In order to cause the image to climb to the saddle point, the component of the force parallel to the path is reversed, driving the image up the path while still using the perpendicular force to constrain the image to the saddle point.

The climbing-image NEB method is able to reach the saddle point within a small number of iterations, even for small image sets and poor initial image choices. This significantly reduces the computational effort that needs to be committed to studying the diffusion path. In some situations, though it is more efficient to use the improved tangent NEB with a sufficient number of images. Specifically, this is useful where the saddle point is a high symmetry structure between the initial and final positions.

3.4 Calculation Parameters

This Section describes the parameters used in the calculations comprising the remainder of this thesis.

3.4.0.4 Supercell and Cluster Structures

Supercell calculations were performed with cubic supercells containing 216 Ge or Si atoms in the perfect case.

Clusters were used only for germanium-based calculations. Two clusters were used, one containing 329 Ge and 172 H atoms and centred on a Ge atom (501 atom clusters), and the second containing 376 Ge and 192 H atoms and centred on an H-site of the crystal (568 atom clusters). As indicated, all the clusters are terminated with hydrogen atoms. Most of the calculations are performed with relaxed Ge-H bond lengths and with the hydrogen atoms and surface germanium held stationary during relaxations. The effect of Ge-H bonds elongated to reproduce the experimental band gap, and fully relaxed surfaces are investigated in Section 5.3. All the clusters are calculated using the experimental value for the lattice constant 5.657 Å[128].

In all calculations not specified as 'symmetry constrained', the symmetry of the system is broken by applying random displacements to the atoms surrounding the defect prior to commencing relaxation.

3.4.0.5 Brillouin Zone Sampling

In the supercell calculations, the Brillouin Zone was sampled according to a Monkhorst-Pack sampling scheme of eight **k**-points (MP-2^3).

3.4.0.6 Wavefunction Basis Sets

In all calculations, the Si and Ge atoms were modelled using contracted basis sets containing (4,4,1) distinct exponents for the (s,p,d) orbitals, respectively and optimised for the bulk crystal. The effect of using a larger basis set is discussed briefly in Section 5.4, but very little difference was found, suggesting that the contracted basis set used here is a good approximation to the uncontracted set.

The terminating hydrogen was modelled using a contracted wave function basis set of four *s* and one *p* orbital, optimised for isolated SiH_4.

Dopant atoms (As, P, B) were modelled using uncontracted basis sets containing four of each *s*, *p* and *d* orbitals and optimised for isolated atoms.

3.4.0.7 Charge Density Basis Sets

Charge density was modelled in all cases with atom-centred basis sets using five *d* and one *s*-type orbital for all species apart from terminating hydrogen, where basis sets of five *s*-type orbitals were used.

3.4.0.8 Pseudopotentials

All atoms were modelled using the pseudopotentials of Hartwigsen, Goedecker and Hutter [101].

3.4.0.9 Exchange Correlation Energy

The AIMPro default settings were used for the exchange correlation energy. In supercell calculations, the functional of Perdew and Wang (PW92) [92] was used while for the cluster calculations a Padé parametrisation was employed [129].

3.5 Chapter Summary

In this Chapter, the theoretical method used in the studies described in this thesis has been described and explained. The details of the AIMPro implementation of density functional theory in both the supercell and cluster methodologies were discussed, followed by a comparison of results calculated on the vacancy and divacancy in silicon. It was seen that a 216 atom supercell gave results converged with supercell size for nearly all values calculated, while for cluster calculations, a cluster with 181 or 329 Si atoms was required depending on the calculation being performed.

A discussion followed on the relative strengths of the supercell and cluster methodologies for calculations in silicon and germanium. It was explained why supercell calculations are believed to be more reliable for silicon while for germanium-based calculations, the cluster methodology was preferred.

The second half of the Chapter presented a description of the methods used to calculate defect structures and the experimentally observable properties as well as a discussion of the calculation parameters to be used in later chapters.

Chapter 4

Experimental Methods

4.1 Introduction

Much of the work presented in this thesis concerns the use of atomistic theoretical modelling methods to provide explanations of experimental results on the properties of lattice defects in silicon and germanium. It is in this way that theory and experiment complement one another with each asking questions that can be best answered by the other.

This chapter will contain a discussion of the experimental methods relevant to the rest of the thesis, followed in each case by an example of a specific study performed using that method to illustrate how it may be used to further our understanding of solid state physics. The aim of this Chapter is to provide a suitable background to the discussion of experimental results in later Chapters.

4.2 Deep Level Transient Spectroscopy

Deep Level Transient Spectroscopy (DLTS) is a powerful tool to study defect related electrical levels deep within the band gap of a semiconductor. It was originally introduced by Lang [130], and has been used to study the E-centre [19, 131] and divacancy in germanium [30], as well as the E-centre and oxygen related defects in silicon [132, 133], to give a very few examples. Some good reviews can be found in the literature [134, 135]. In addition to the basic technique, a number of modifications have been developed, including optical DLTS [136] and Laplace DLTS [137], but these will not be discussed in this section.

4.2.1 Deep Levels

Defects in semiconductors often introduce deep levels into the electron energy gap. These levels are defined as being located at the level of the Fermi Energy (E_F) at which the stable charge state of the defect changes. Energy levels located far from the band edges are referred to as deep levels, and due to the strong binding energies of electrons or holes, they are strongly localised on the trapping defects. This spatial localisation results in a high level of delocalisation in k-space, allowing the carriers to interact with many phonons, and therefore the defects can act as non-radiative recombination centres.

The capture rates of free electrons and holes by lattice defects are given by

$$c_n = \sigma_n \langle v_n \rangle n \tag{4.1}$$

$$c_p = \sigma_p \langle v_p \rangle p \tag{4.2}$$

where $\sigma_{n,p}$ are the capture cross sections for the carriers n, p are the free electron and hole concentrations, and $\langle v_{n,p} \rangle$ are the thermal velocities of the electrons and holes, respectively. These thermal velocities are given by

$$\frac{3}{2} k_B T = \frac{1}{2} m^*_{n,p} \langle v^2_{n,p} \rangle \tag{4.3}$$

where

$$\sqrt{\langle v^2_{n,p} \rangle} = \langle v_{n,p} \rangle, \tag{4.4}$$

$m^*_{n,p}$ is the effective mass of an electron or hole respectively, and k_B and T have their usual meanings.

Electron and hole emission rates for the traps are calculated using a Boltzmann distribution of the form

$$e_{n,p} = A_{n,p} \exp\left(-\frac{\Delta E_{n,p}}{kT}\right) \tag{4.5}$$

where $\Delta E_{n,p}$ is the Gibbs free energy for the process of emission of an electron or hole respectively. The pre-factor $A_{n,p}$ is given by

$$A_{n,p} = \frac{\sigma_{n,p}\langle v_{n,p}\rangle N_{c,v}}{g} \tag{4.6}$$

where $N_{c,v}$ is the effective density of states of the conduction and valence bands, respectively, and g is the degeneracy of the defect level. $\Delta E_{n,p}$ can be expanded into

$$\Delta E_{n,p} = \Delta H_{n,p} - T\Delta S_{n,p} \tag{4.7}$$

where $\Delta H_{n,p}$ is the enthalpy change for the emission, and $\Delta S_{n,p}$ is the entropy change. Combining Equations 4.6 and 4.7 with 4.5 gives

$$e_{n,p} = \frac{\sigma_{n,p}\langle v_{n,p}\rangle N_{c,v}}{g} \exp\frac{\Delta S_{n,p}}{k} \exp-\frac{\Delta H_{n,p}}{kT} \tag{4.8}$$

From Equations 4.3 and 4.4, $\langle v\rangle$ can be be seen to be proportional to $T^{1/2}$, and N is known to be proportional to $T^{3/2}$ for a 3D system. Therefore an Arrhenius plot of the emission rates of $\ln e/T^2$ vs $1/T$ should be linear, and will yield the enthalpy of emission from the gradient and the capture cross section of the defect from the intercept.

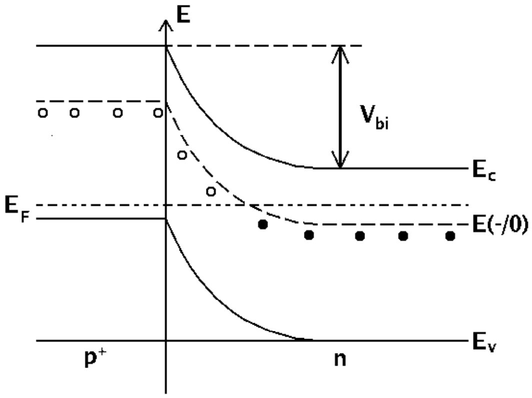

Figure 4.1: Diagram showing the band-bending present at a p^+n junction containing a defect with a single acceptor level just below the n-type Fermi level. Also shown is the built in voltage of the junction, V_{bi}

4.2.2 The Junction

DLTS experiments use the inherent properties of the space charge region of a p-n junction or Shottky diode to study the emission rates of any defects present within the region. Band bending at the interface between the regions in such a structure ionises the defects in the region as the Fermi level is effectively shifted across the band-gap, as illustrated in Figure 4.1. An electric field is also present across the interface. This is important to remove emitted charge carriers before they can be recaptured by the defects in the studied region.

The width of the space charge region can be varied using an externally applied voltage V, and is given by

$$W = \sqrt{\frac{2\epsilon(V_{bi}+V)}{qN}} \tag{4.9}$$

where V_{bi} is the built in voltage of the junction as shown in Figure 4.1, ϵ is the permittivity of the semiconductor, q is the carrier charge and N is the density of ionised defects in the region. The capacitance of the region is given by

$$C = \frac{\epsilon A}{W} = A\sqrt{\frac{qN\epsilon}{2(V_{bi}+V)}} \tag{4.10}$$

4.2.3 Capture and Emission

To study the emission rates of defects within the space charge region of the junction, a voltage pulse is applied to ionise the defects as shown in Figure 4.2. A reverse bias (V_0) is initially applied across the junction, and a filling pulse for majority carriers is applied by removing this reverse bias temporarily, decreasing the size of the space charge region. The applied voltage remains at zero for a time long enough to fill all the traps in the space charge region, after which it is returned to V_0 and the evolution of the capacitance is measured as the traps emit carriers and return to their equilibrium state. For minority carrier filling, the magnitude of the reverse bias would be increased above V_0 during the filling pulse.

From equations 4.9 and 4.10, it can be seen that the capacitance of the space charge region depends on the density of carrier traps such that

$$C(t) = C_0\sqrt{\frac{N(t)}{N_0}} \tag{4.11}$$

where C_0 and N_0 are the equilibrium values of the capacitance and number of traps for $V = V_0$. N will tend to N_0 in this regime via an exponential decay of the transient, given by

$$N(t) = N_0 - N_t e^{-e_n t} \tag{4.12}$$

for emission of electrons as majority carriers, where N_t is the number of traps under examination, and therefore $N_t e^{-e_n t}$ is the number of ionised traps at time t. If the emission is of minority carriers, the sign of the second term changes, and for hole emission, the electron emission rate would be replaced. In most studies, where $N_0 \gg N_t$, Equation 4.11 becomes

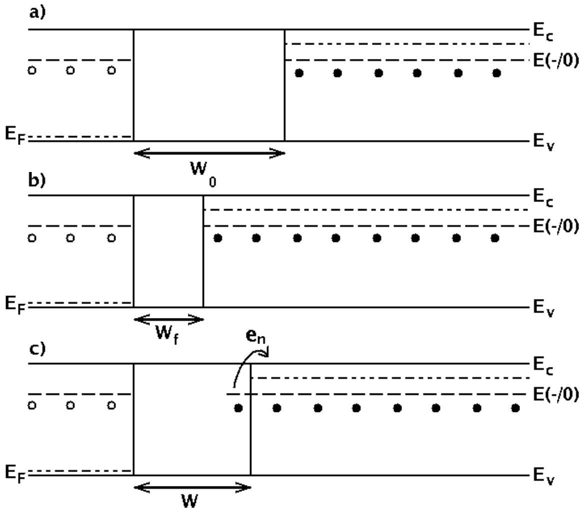

Figure 4.2: Schematic diagram illustrating the filling pulse as used in majority carrier DLTS on a p^+n junction containing a defect with a single acceptor level, such as that shown in Figure 4.1. a) The initial situation, with a steady reverse bias V_0, and space charge region width W_0. b) The filling pulse during which the applied voltage is turned off, the space charge region is reduced and the defect acceptor levels are filled. c) With the reverse bias voltage restored, charged defects in the depletion region thermally emit electrons back into the conduction band where the inbuilt electric field sweeps them away from the junction. Note that for the sake of clarity, the band bending discussed previously is not included on this diagram.

$$C(t) = C_0 \left(1 - \frac{N_t}{2N_0} e^{-e_n t} \right) \tag{4.13}$$

and the fractional change in capacitance is

$$\frac{\Delta C}{C_0} = -\frac{N_t}{2N_0} e^{-e_n t} \tag{4.14}$$

As noted above, where the method is used to study minority carrier emission, the capacitance change becomes positive but the equations and arguments presented here otherwise apply.

To measure $e_{n,p}$ versus temperature, a sequence of filling pulses is applied to the junction at different temperatures. A common measurement technique is the double box-car method [130, 138]. In this method two measurement times, t_1 and t_2 are

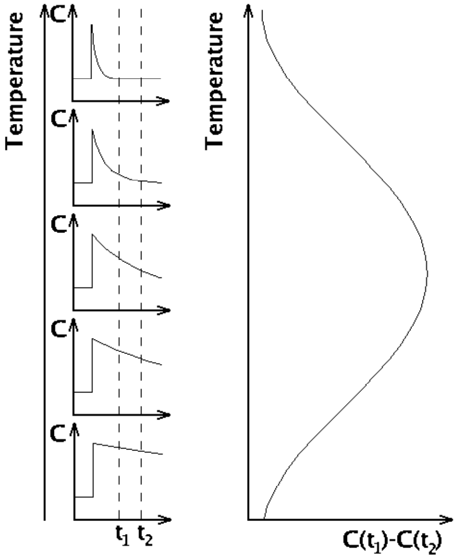

Figure 4.3: Diagram displaying the stages in a double box-car measurement under DLTS. The diagrams on the left show the evolution of capacitance with time for minority carrier emission at a variety of temperatures, increasing from bottom to top, and also indicating the two measurement times, t_1 and t_2. The diagram on the right shows how $C(t_1) - C(t_2)$ varies with temperature for fixed measurement times.

chosen, and $C(t_1) - C(t_2)$ is measured for varying values of T. This method is depicted in Figure 4.3.

The emission rates $e_{n,p}$ can be measured from these results by noting the existence of the maximum in capacitance change for a certain temperature. From Equation 4.13, we can see that

$$C(t_1) - C(t_2) = \frac{C_0 N_t}{2N_0}\left(e^{-e_n t_2} - e^{-e_n t_1}\right) \tag{4.15}$$

and that a maximum occurs when

$$0 = \frac{d\left(C(t_1) - C(t_2)\right)}{dT} \tag{4.16}$$

$$0 = \frac{C_o N_t}{2N_o}\left(-t_2 e^{-e_n t_2} + t_1 e^{-e_n t_1}\right)\frac{de_n}{dT} \tag{4.17}$$

$$0 = -t_2 e^{-e_n t_2} + t_1 e^{-e_n t_1} \tag{4.18}$$

$$e_n(T_{\max}) = \frac{1}{t_2 - t_1}\ln\frac{t_2}{t_1} \tag{4.19}$$

By altering t_1 and t_2, the value of e_n for which the maximum of $C(t_1) - C(t_2)$ occurs can be changed, and hence the temperature at which this maximum is observed. By calculating the emission rate for a number of temperatures, and plotting $\ln e/T^2$ vs $1/T$, the enthalpy of emission and the capture cross section of the defect can be calculated, as explained above in Section 4.2.1.

4.2.4 Vacancy Clusters Observed in Electron-Irradiated Silicon

Bleka *et al* published work in 2007 using DLTS to study irradiation damage caused by electron irradiation of silicon [139]. The group studied two materials - magnetic Czochralski (MCz) and standard-float-zone (SFZ) wafers, with phosphorus doping. Carbon and oxygen concentrations were measured using secondary ion mass spectroscopy (see Section 4.4) to be 0.5-1$\times10^{18}$ cm^{-3} and $\leq 10^{16}$ cm^{-3} in the MCz and $< 5 \times 10^{15}$ cm^{-3} and 2-4$\times10^{15}$ cm^{-3} in the SFZ samples respectively. The samples were irradiated with 6-MeV electrons to a dose of 5$\times10^{12}$ cm^{-2} at room temperature, and kept at room temperature for the duration of the investigation.

In both samples, peaks in the DLTS spectrum were detected at ∼80, 113, 163 and 198 K, with no significant difference in peak amplitude between the samples. The difference in amplitude that was detected was constant across all peaks and attributed to errors in electron dose. The first peak was attributed to the vacancy-oxygen (VO) centre, and the second and fourth to the divacancy (V_2) defect. The third peak was not immediately identified with any defect. After 2036 hours at room temperature, the third peak was observed to have disappeared, the second V_2 peak had decreased and the VO peak had increased.

By subtracting the final value of $\frac{\Delta C}{C_0}$ after the 2036 h anneal from the values measured after shorter anneal times for the unknown peak and the second V_2 peak, it was seen that the two peaks decreased at the same rate. This was taken to suggest that the unknown defect possesses a trap level coinciding with the second V_2 level.

The defect concentration giving rise to any given peak is calculated by using the standard equation $N_t = 2N_0\frac{\Delta C}{C_0}$, and from this an annealing rate of 2.3×10^{-7} s^{-1} was calculated. Taking a typical annealing prefactor of $10^9 - 10^{13}$ s^{-1}, an activation energy of 0.9-1.2 eV for the annealing was estimated. Level transitions at 0.37 and 0.45 eV below the conduction band were deduced for the first and second levels of the unknown defect respectively.

The unknown defect was first compared with the substitutional phosphorus-interstitial carbon (P_sC_i) defect, known to have similar energy levels and be unstable at room temperature [140]. This, however, was argued not to be the defect in question, as the ratio of phosphorus to oxygen, the two competing traps for the carbon interstitial in the samples, was very different between the two samples and yet the concentration of the unknown defect was almost unchanged.

Comparison was then made with another study on 7-MeV proton-irradiated silicon, in which the first level of the unknown defect is observed with a significantly higher trap concentration [37]. This difference was taken to indicate that the level was related to a higher-order defect centre. The difference in position of the two levels is also taken to support this view. As the two levels of the unknown defect are closer together than those of the divacancy, this suggested that the dangling bonds on which these levels are localised are more distant than in the divacancy, reducing the coulomb repulsion between them, and hence the energy difference between the levels. Thus it was suggested that the defect was an intrinsic defect cluster larger than the divacancy.

The increase in concentration of VO as the unknown defect annealed was the final piece of evidence presented to identify the defect as being vacancy related. Therefore the paper concluded that they had detected a vacancy-related defect larger than V_2 which is unstable at room temperature.

4.3 Positron Annihilation Spectroscopy

Positron annihilation spectroscopy (PAS) is a technique used to study vacancy-type defects in semiconductors and metals. The basic principle of the technique is that the annihilation of externally injected positrons (e^+) with electrons in the crystal structure is quantitatively studied, and that this data is examined to give information on the environment of the electrons. Information can be gathered on the size of vacancy clusters present and their neighbouring atoms and also on amorphised regions. It has been used for example, to study vacancy growth in silicon [141] and germanium [142] and fluorine-vacancy clusters in silicon [143, 144]. This section will provide a relatively brief explanation of the method and the information which can be gathered from it. For a more in-depth discussion, see for example, references [145, 146] and references therein.

4.3.1 Experimental Set-Up

Conventionally, artificial radioisotope β^+ emitters are used as the source for PAS studies. ^{22}Na is particularly favoured as it emits a photon of γ radiation at the same time as the positron, allowing for measurement of the positron lifetime. Mean penetration depths from such a source typically range from 10-100 μm, and the annihilations will probe a volume of the target material around this depth. Variable energy positron beams (0.1-1MeV) can also be used as positron sources, with pulses of at most $\sim$100 ps duration required for lifetime measurements. Photon detectors (often BaF_2 or plastic scintillators) are used to collect both the source and annihilation photons.

Upon entering the sample, the positrons thermalise, dropping in energy to a few tens of meV, well below the kinetic energies of the electrons with which they annihilate. This occurs through ionisation, electron-hole excitation and finally phonon scattering as the positron drops in energy. This process occurs within a few picoseconds, much shorter than the positron lifetimes of 0.1-1 ns.

4.3.2 Annihilation

The primary mechanism for positron-electron annihilation is two-photon annihilation, resulting in the emission of two 511 keV photons. In positron-electron centre of mass reference frame, these photons will be emitted in precisely opposite directions, while in the laboratory reference frame, there can be a small perturbation to both the angle and energy of the photons due to the momentum of the electron. The other quantity of note in the annihilation is the positron lifetime τ or annihilation rate $\lambda = \tau^{-1}$. These three quantities can be calculated from atomistic variables as follows:

$$\Delta E \sim \frac{cp_{//}}{2} \tag{4.20}$$

$$\Delta\theta \sim \frac{p_{\perp}}{m_0 c} \tag{4.21}$$

$$\lambda \sim \pi r_c^2 n_e \tag{4.22}$$

where $p_{//,\perp}$ are the components of electron momentum parallel and perpendicular to the photon emission direction respectively, m_0 is the electron rest mass, r_c is the classical electron radius and n_e is the effective electron density as experienced by the positron, or more accurately, the overlap integral of the electron and positron probability densities.

Via n_e, the positron lifetime is sensitive to open volumes within the target material. As positrons are repelled by the ion cores in condensed matter, thermalised positrons can become trapped at open volume defects with a rate

$$\kappa = \nu c_t \tag{4.23}$$

where c_t is the defect concentration experienced by the positrons, and ν is a trapping constant. Due to the reduction in electron density within the open-space regions, the average lifetime for positrons trapped in these defects increases, and the lifetime profile for a PAS study will contain contributions from different annihilation environments with differing τ.

$$N(t) = \sum_{i=1}^{n} I_i \lambda_i \exp\left(-\lambda_i t\right) \tag{4.24}$$

where I_i is a positron fraction which can be extracted along with λ_i for each environment by computer models. Each type of defect, and the bulk material itself will exhibit a different value of λ_i, and each defect will also possess a different trapping constant ν, and therefore I_i.

Doppler broadening of the photon energy due to electron momentum can give information on the annihilation environment. The spectrum is conventionally characterised by the parameters S and W, S being the fractional area of the central part of the count distribution, while W provides the same measure for the tails. The S parameter will therefore increase when more positrons are annihilating with low-momentum electrons, and the W parameter when interaction with high momentum electrons increases. These parameters can change if, for example, more positrons become trapped at open volume defects, or if the atoms surrounding vacancies changes, such as during defect annealing. Angular correlation measurements reveal similar information as Doppler broadening measurements, as explained above. Typically, angular correlation measurements are taken with detectors several metres from the sample, improving angular, and hence momentum resolution at the expense of detector efficiency, as only a small solid angle around the sample is monitored.

Combining Doppler broadening and positron lifetime measurements is also possible, using one photon to signal the end of a positron lifetime count and the other in the Doppler measurement.

4.3.3 Vacancy Clustering in ZnO

A study published in 2008 by Børseth et al in 2008 used PAS among other techniques to study defect evolution after nitrogen implantation into ZnO samples [147]. Nitrogen was implanted into the ZnO samples at room temperature with doses of 1.2 or 2.4×10^{15} cm^{-2} and energy of 220 keV resulting in a projected range of $\sim$ 330 nm. Measurements were taken on the samples immediately post implantation and after annealing stages at 600, 800 and 1000°C. PAS was used to study the evolution of defects containing zinc vacancies (V_{Zn}) over the annealing processes. Oxygen vacancies (V_O) were not expected to be detectable in this study due to being positively charged defects and hence not trapping positrons.

The post-implant PAS measurements on the samples shown in Figure 4.4 displayed an S component significantly above that observed for the single V_{Zn}, suggesting the presence of clusters of these vacancies, $(V_{Zn})_n$. This S value was also seen to be dose dependent, which provided further evidence that it was due to these clusters, not saturation trapping at V_{Zn} defects, as saturation trapping would not display dose dependence.

After the 600°C anneal, the S parameter was found to have risen further suggesting the formation of larger clusters, termed $(V_{Zn})_N$, $N > n$. The 800°C anneal caused the S parameter to drop substantially indicating that either all the vacancy clusters were removed by this anneal, or that the positrons were being trapped at other defects with a lower characteristic S parameter. After the 1000°C anneal, the S parameter was seen to have risen to close to the as-implanted level attributed to $(V_{Zn})_n$.

A substantial increase in electron concentration in the sample was also observed after the 1000°C anneal, attributed to the annealing of acceptor defects. To investigate whether these two changes were related, a second PAS measurement was taken on the 800°C annealed samples. During the second measurement, the temperature of the sample was raised to 500K in order that the positrons should gain sufficient thermal energy to escape from any acceptor defects and be trapped by V_{Zn}. An increase in S

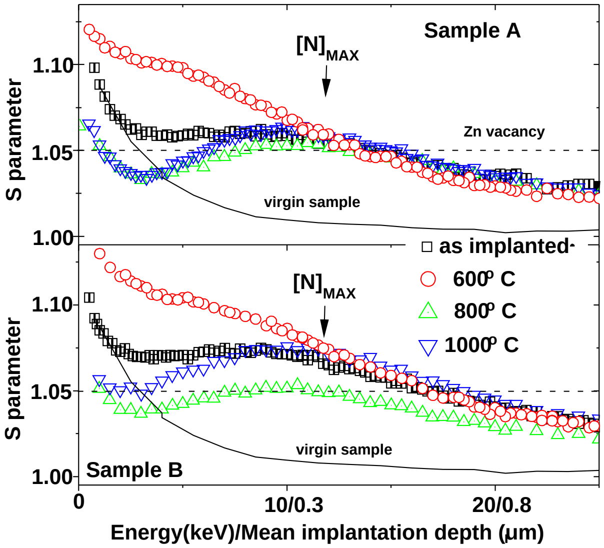

Figure 4.4: Image from Ref [147]. Doppler spectroscopy data for N implanted ZnO samples. The dashed line indicates the S parameter for V_{Zn} and $[N]_{MAX}$ indicates the position of peak N concentration. Sample A and B have implanted doses of 1.2 and 2.4×10^{15} N cm^{-2} respectively. Results for a virgin sample are included for reference.

parameter was observed, in accordance with the hypothesis that the positrons were being preferentially trapped at acceptor sites in the initial measurements.

The evolution of V_{Zn} related defects in N implanted *n*-type ZnO thus seems to follow the following pattern. After implantation, small clusters of V_{Zn} are observed to form. On annealing at 600°C, some of these clusters evolve to form larger clusters which then anneal out during the 800 or 1000°C annealing stages, while the smaller clusters survive the annealing and are still present after the highest temperature anneal. Further, the PAS data suggests the presence of acceptor defects after the 800°C anneal with a lower S parameter than the vacancy clusters which then disappear during the 1000°C anneal.

4.4 Secondary Ion Mass Spectroscopy

Secondary ion mass spectroscopy (SIMS) is a technique used to measure depth profiles of concentration of different species in a sample. Good descriptions of the method can be found in the literature [148, 149], and the method has been used to study impurities in both silicon [150, 151] and germanium [152, 153], and has even been used to study vacancy cluster concentrations in germanium through marking with impurity atoms [141].

4.4.1 Basic Principles

SIMS measurements are performed by firing a primary ion beam with energies of ∼1-20 keV at the sample of interest. These ions can produce secondary ions from the sample, which are gathered and passed to a mass spectrometer to record their mass-charge ratio. As the primary ion beam gradually erodes the sample surface, the evolution of the signal from the mass spectrometer with time can be used to produce a depth profile of the concentration of the atomic species present.

To ensure the surface erosion is constant, the primary ion beam is usually rastered over an area of the sample, and in order to avoid gathering secondary ions originating in the walls of the etching pit, either physical or electrical gating is used. These methods involve either using an experimental setup which does not collect secondary ions from regions near the pit's edge, or one which does not count events measured while the beam is passing over these edge regions.

To convert the measurements of count rate for a given species into a depth profile for that species, a reference sample must be used. This allows the determination of the fraction of atoms in the eroded volume which are sputtered as ions and collected by the detection apparatus. Once the initial surface has been eroded (once the depth exceeds ∼10 nm), the rate of erosion of the sample becomes fairly constant, and so the evolution of the measured signal with time can then be converted directly to a comparison of signal with depth.

4.4.2 Primary Ion-Sample Interactions

The processes by which the sputtering occurs within SIMS are complicated to understand in detail, involving linear cascade theory [154]. The primary ion undergoes a series of binary collisions with atoms in the sample, and imparts sufficient energy to many of those atoms that they in turn undergo further collisions, resulting in a cascade of displacements. If a cascade path intersects the surface, and the ejecting particle, be it a single atom or a group, has sufficient energy to overcome surface binding, it will be sputtered from the sample. These particles usually originate within 2-3 atomic layers from the surface, and leave the surface with energies of a few eV.

The processes resulting in the ionisation of ejected particles are more complicated still, but in terms of general trends, electronegative atoms near the sample surface tend to lead to positively charged ions while electropositive atoms cause the ejection of negatively charged ions. It is for this reason that oxygen and caesium are often used as primary ions due to their strong electronegativity and electropositivity respectively.

During the process of sputtering, changes will occur in the sample structure which need to be taken account of to some extent when considering the results. The first is that the structure of the sample will be disturbed by the addition of the primary ions, which remain in the material. These primary ions serve to ionise the ejected particles as described above, but may have other effects. The second, more important effect is that of broadening. As the cascade processes occur, they force many atoms further into the sample, increasing the depth at which the species are found. This effect is highly sensitive to channelling effects, whereby a displaced atom can travel large distances along open channels in the bulk crystal. To reduce the magnitude of the broadening, the energy of the incident ions can be reduced, and the incident beam angle relative to the surface normal can be increased.

4.4.3 Nitrogen Incorporation in GaNAs

SIMS has been used in a study published by Zhao *et al* in 2006 [155] into the incorporation of nitrogen into GaAs grown by molecular beam epitaxy at varying rates to form $\mathrm{GaN}_y\mathrm{As}_{1-y}$ quantum wells. The devices are designed to act as quantum well lasers, and the effect of the N is to decrease the band gap of the GaAs, confining carriers to the nitrogen-containing layer and allowing for carrier injection to lead to population inversion in the wells. The samples studied consisted of 500 nm GaAs buffer layers with 18 nm of GaNAs and a capping layer of a further 90 nm of GaAs grown upon them. The GaNAs layers were grown at rates ranging from 1 down to 0.125 $\mu\mathrm{mh}^{-1}$. SIMS measurements were taken of the samples both before and after a 30s 700°C rapid thermal annealing stage, as were high resolution x-ray diffraction (XRD) measurements, a technique which can be used to measure the amount of substitutional N in the crystal.

The results indicated a marked increase in nitrogen incorporation in the crystal with decreased growth rate. However for the lowest growth rates, undesirable relaxations occurred in the mis-matched GaNAs region. Also, while the concentration of substitutional nitrogen measured by XRD increased with decreasing growth rate, the total nitrogen concentration, measured with SIMS increased much faster, leading to a shift from primarily substitutional to primarily interstitial nitrogen as the growth rate decreased. The rapid thermal annealing step did not change the amount of interstitial or substitutional nitrogen in the samples, but it did increase the photoluminescence intensity and cause a blue-shift in the emitted light. Overall, it was seen that a moderate decrease in growth rate led to a desirable decrease in band gap of the GaNAs layer, but that larger decreases in growth rate led to relaxations in the GaNAs layer which dramatically lower the quantum efficiency of the device by providing centres for non-radiative recombination.

4.5 Spreading Resistance Profiling

Spreading resistance profiling (SRP) is a technique used to produce a depth profile of resistivity, and thence carrier concentration and active dopant concentration in semiconductors. The physics of the technique is discussed elsewhere [156] and there has been extensive work performed to establish reproducibility and reliability of the technique [157, 158]. There are also variations of the work including one which can measure two dimensional dopant profiles [159], though this is beyond the scope of this section.

Typically, SRP measurements are carried out using a small point contact and a large current return contact. A bevelled surface is cut into the sample usually at an angle of $\sim 5 - 10°$ from the 'natural' surface in order to magnify the depth profile of the sample. For a flat circular probe of diameter a, the majority of the potential drop occurs within a distance of $3a$ of the probe, and thus a measure of the voltage drop between the probe and the current return contact gives a measure of the resistivity of the volume of sample near the probe. Calibration is achieved by comparing the results with those measured on controlled samples of known dopant concentration.

4.5.1 Evolution of Boron Interstitial Clusters in Silicon

SRP has been used to study boron interstitial clusters (BICs) in silicon and their evolution with annealing for increasing times [160]. Boron doping was grown into silicon samples by molecular beam epitaxy, with a deeply buried δ-doped layer and a surface region with uniform doping. The samples were implanted with 60 keV Si ions to create implantation damage in the broad region, but not in the deeply buried δ-doped layer which acted as a reference.

After annealing, SIMS measurements revealed an enhanced diffusion of the broad B layer, due to transient enhanced diffusion effects caused by the interstitial supersaturation. An immobile peak was also observed in the sample with the highest level of Si implantation, attributed to BICs. SRP measurements of carrier density in the samples were performed, and showed a strong deactivation of boron in the implanted regions in accordance with the formation of BICs. With longer annealing times, the concentration of B within the clusters remained almost constant for up to fifteen minutes for all implantation doses, and the BICs dissolved as the annealing time increased further. This was attributed to an Oswald ripening process acting on the defects for short annealing times until the interstitial supersaturation dropped below a level able to sustain the BICs.

4.6 Transmission Electron Microscopy

Transmission electron microscopy (TEM) is a technique analogous to traditional optical microscopy. Using electrons in place of photons to probe the sample allows for a much higher resolution due to a decrease in wavelength. A 10 keV electron has a wavelength, calculated using the relation $pc = \sqrt{E^2 + 2Em_0c^2} = hc/\lambda$, of 0.12 Å, around five orders of magnitude smaller than that for visible light. This translates directly to an improvement of around five orders of magnitude in maximum resolution [161]. A more in-depth discussion of the technique can be found, for example, in reference [162]. This technique has been used for example, to study fluorine-vacancy complexes [144, 163], and vacancy clusters [141] in silicon.

4.6.1 Controlling the Electron Beam

The electron beam in an electron microscope is created in a vacuum of $< 10^{-4}$ mbar with an energy of usually ten to a hundred keV. Magnetic lensing of the electrons is used to focus the beam, with simple microscopes having two lenses in an equivalent set-up to an optical microscope, but with magnifications of 10,000 achievable. As the shape of the lenses are constrained by Maxwell's equations, it is not possible to shape a simple lens so as to avoid spherical aberration, which becomes the most important factor in limiting the resolution of the microscope.

The problem of spherical aberration was addressed by Scherzer and later Feynman [164], who realised that magnetic octupole and quadropole lenses could be used to correct the focus of the beam. Two correcting lenses are required, each consisting of a quadropole proceeded by an octopole lens, to correct for spherical aberration in the two directions perpendicular to the beam.

4.6.2 Sample Restrictions

Samples to be studied using TEM have to conform to two main conditions for the technique to be useful. Firstly, the samples must be penetrable by the electrons, which in general implies a maximum thickness of around 100 nm. The sample must therefore be able to withstand the preparatory techniques used, typically ion-beam milling or chemical etching, to produce a smooth surface at this thickness. Ion-beam milled samples are especially prone to structural defects caused by the ions imparting significant energies to atoms in the sample.

The second condition is that the structures being observed by the technique must be able to withstand bombardment by the 10-100 keV electrons used in the beam, and the sample must not be susceptible to damage which would obscure the structures being studied.

To form an image, it is possible to use either the transmitted or diffracted electron beam. The former is formed from those electrons which have not interacted significantly with the sample, with the material of the sample appearing as dark areas in the image, and the latter from those which have interacted strongly and have been deflected from their initial trajectories. For crystalline materials, the transmission or diffraction properties of the sample depend strongly on the Bragg condition, and so the sample is often mounted on a rotating table. The diffracted beam image is often used because the electrons which form it have directly interacted with the sample, and low-contrast details are more clearly observable.

4.6.3 Real-Time Imaging of Gold Nanowire Evolution

TEM has been used to study, in real time, the evolution of nanoscale gaps in gold nanowires under feedback controlled electromigration [165]. The gold layer was grown on Si_3N_4 membranes upon silicon wafers. Photo- and electron-beam lithography was used with thermal evaporation to shape the samples into wires with 50nm wide, ∼100-150 nm long constrictions. These constrictions were observed under TEM as currents were passed across them.

The current used was feedback-controlled, with the voltage applied being varied with the conductance of the sample, to avoid thermal runaway leading to thermal evaporation of the gold at the point of narrowing. The TEM was performed using the transmitted beam, and was used to observe the shape of the gold layer and the narrowing of the layer as the experiment progressed.

In the first experiment, current was passed across the constricted region until the wire was broken by narrowing. With the feedback mechanism keeping the potential difference across the constricted region at the critical level for electromigration, the sample exhibited faceting at a ∼15 nm narrowed region, at the upstream edge of the etched constriction. To explain this faceting, an 'unzipping' model was proposed, where the crystal erodes one atomic layer at a time. In this model, the erosion would begin with a single surface atom being thermally excited to an adatom position. This atom would then be blown across the surface in the direction of current flow by an electron wind force, leaving a vacant site in its place. This vacant site would migrate in the opposite direction until it reached the edge of the faceted region, and would also act as a source for excitation of further adatoms from the same layer, as the atoms adjacent to the vacant site have a reduced number of nearest neighbours, and hence a reduced binding energy.

To rule out the possibility of thermal migration or sublimation of the gold atoms, a second experiment was performed to study the asymmetry of the narrowing, described in Figure 4.5. Current was passed in one direction across the constriction, and a faceted narrowing was observed at the upstream side of the region as before,

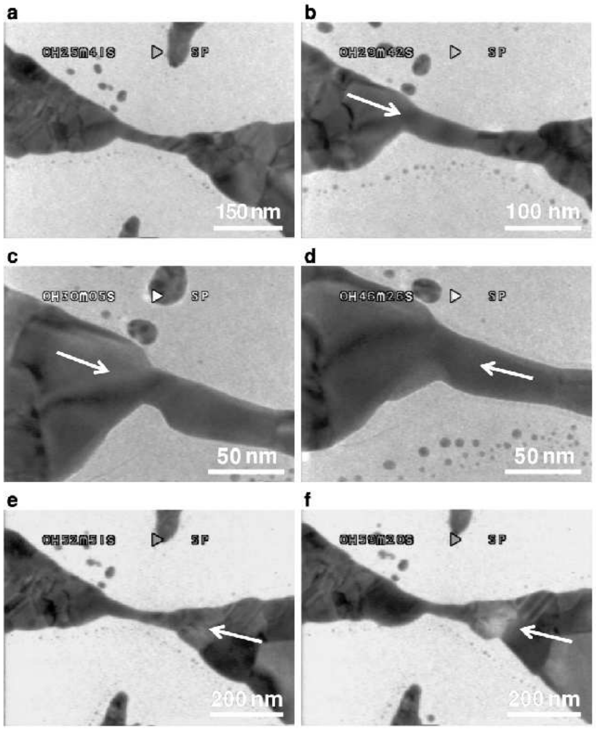

Figure 4.5: Figure from Ref [165]. TEM images of the Au layer in the second experiment described. The Au layer is the dark region, and arrows indicate the direction of current flow in the sample. a) Initial structure of the sample. b) Current is applied. c) A faceted void begins to grow into the Au layer. d) Reversal of the current causes the void to refill. e) The void is now completely refilled. f) After further time, a build-up of material is visible at the former location of the void, and a void begins to grow on the opposite side of the constricted region.

while a build-up of material was observed at the downstream end. When the current was reversed, the narrowing was then at the downstream end of the constricted region and began to refill. Further migration resulted in a build up of material over the site of the narrowing and the appearance of faceted narrowing at the other end of the constriction. This result indicated that the mechanism for narrowing cannot be thermal migration or sublimation, as neither of these processes are reversible or dependent on current direction.

4.7 Scanning Tunnelling Microscopy

Scanning tunnelling microscopy (STM) is a technique used to produce surface height profiles at an atomic scale. If the sample is electrically conductive, a current can be passed between a sharp-tipped probe, typically formed of platinum-rhodium or tungsten, and the sample. As the current depends exponentially on the width of the tunnelling barrier, a very accurate height profile can be attained. Spatial resolution of $\sim$2 Å allows for truly atomic-scale study of the surface of a sample. For an in-depth discussion of the technique see, for example reference [166] and references therein.

4.7.1 Self Assembly of Ordered Bi Patterns on InAs

Growth of bismuth patterns on Bi-passivated InAs surfaces has been studied using STM over the course of a number of annealing stages [167]. Bismuth was evaporated onto the sample at a rate of approximately 0.5 monolayers/min and approximately 1.5 monolayers were deposited onto the substrate. The sample was then annealed at 250°C for one and then twelve hours. Subsequent STM measurements revealed a set of parallel lines in the $[0\bar{1}1]$ direction which became more straight and uniform with longer annealing. Annealing at higher temperatures caused the surface bismuth to desorb, revealing the apparently unperturbed Bi-passivated InAs surface.

More detailed examination of the STM data yielded a periodicity along the lines of $\sim$8.6 Å, double the a_0 of the underlying lattice. The measurements along the lines also revealed a double-peak structure, with the two peaks separated by $\sim$3 Å, the bond length of a Bi dimer. Perpendicular to the lines, a periodicity of 4.3 nm was observed, and the full width at half maximum of the lines was measured to be 11 Å, which is slightly more than double that which has been reported for a single Bi dimer. Therefore, the lines were modelled as consisting of chains of pairs of Bi dimers, with the nano-line dimers lying parallel to the Bi dimers passivating the substrate, as this gives the correct $2a_0$ periodicity along the chains.

4.8 Summary

Various experimental techniques are applicable to studying defects in silicon and germanium. In the context of theoretical research, the usefulness of experimental techniques is to provide data with which theoretical models can be compared to gain a judgement on the reliability of the methods or the predicted atomistic mechanisms which may give rise to that data and also to test predictions made by the theory as to expected experimental measurements.

In the remainder of this thesis, the various methods outlined here will be referred to where appropriate. DLTS and SIMS measurements are often presented as these give information on defect-related carrier traps and diffusion rates, which are the focus of much of the proceeding work. PAS is also important in the study of vacancies and vacancy-related defects, and so will be important in Chapter 5.

Chapter 5

Intrinsic Defects in Germanium

5.1 Introduction

Having established the theoretical and experimental background to the investigations which will be discussed in the remainder of this thesis, this Chapter commences discussion of the original work that has been performed.

Intrinsic crystal defects are the most fundamental of all defects in semiconductors, playing an important role in the formation of many other defect centres and large complexes, as well as playing a strong role in dopant diffusion processes and often being electrically active themselves.

This Chapter will describe theoretical work undertaken in the present investigations to study the annealing behaviour of the divacancy and the electrical properties of a range of vacancy clusters, and will discuss the current understanding of the self-interstitial defect in germanium.

5.2 Modelling Method

Calculations were performed using 216 atom supercells and 501 or 568 atom clusters, as described in Section 3.4. The 568 atom clusters were used for the vacancy cluster study (Section 5.4), while the rest of the work in this Chapter was performed within 501 atom clusters. In the divacancy annealing study (Section 5.3), three treatments of the cluster surface were tested - one with relaxed surface Ge-H bonds, one with Ge-H bonds strained to reproduce the experimental band gap, and one where the entire surface was relaxed at the same time as the defect. The other studies used relaxed Ge-H bond lengths but a fixed surface. All other calculation parameters were as described in Section 3.4.

Formation energies for neutral defects were calculated using the method described in Section 3.3.2, migration barriers using the NEB method in Section 3.3.5 and electrical energy levels using the marker method as described in Section 3.3.4. The acceptor levels of substitutional gold at $E_v + 0.135$ eV and $E_c - 0.215$ eV [168] and the vacancy oxygen (VO) defect at $E_v + 0.27$ eV and $E_c - 0.21$ eV [169] were used as markers for the vacancy clusters. Binding energies for the vacancy clusters were calculated from formation energies only, while the divacancy binding energies were calculated using both methods described in Section 3.3.3.

5.3 Divacancy Annealing

Vacancies (V) in germanium have been the focus of a variety of work over the past few years. The low formation energy of vacancies, calculated to be 1.9 to 2.6 eV [9, 170], compared with 3.5 eV for self interstitials [17], suggest they will play an important role in germanium and they have been suggested as the primary mediating species for self-diffusion [44], and diffusion of some impurities [171]. Single vacancies have been the focus of a number of previous studies, dealing with their diffusivity [35, 170, 172], energy levels [7, 5, 9, 11] and atomic structure [7, 5, 6, 9, 10, 173].

With the high mobility [35, 170, 172] and low formation energy of vacancies, it would not be surprising to find vacancy clusters forming easily in germanium. Indeed, large voids have been observed with diameters ranging from hundreds of nanometres up to ten micrometres following the growth of germanium crystals [33, 29]. Such voids could severely damage a device if they form within its active region.

Although the divacancy (V_2) has been studied Previously using both *ab-initio* methods and experiments, its properties and identification are still the object of some controversy. Structurally, they were shown to have properties similar to those for the silicon case, although with much weaker Jahn-Teller distortions and energies [10]. In fact, the calculated distortion magnitudes and types found in cluster calculations are found to be sensitive to the lattice parameter that was employed to generate the cluster [10, 174]. Energy levels have also been calculated from *ab initio* methods, with a first donor level found to lie at $E_v + 0.03$ eV and first and second acceptor levels at $E_v + 0.3$ eV ($E_c - 0.36$ eV) and $E_c - 0.4$ eV respectively [174]. Two deep level transient spectroscopy (DLTS) studies also report results for the divacancy. The earlier study reports a pair of electron traps at $E_c - 0.35$ eV and $E_c - 0.32$ eV which anneal at 150°C, and are attributed to the divacancy [26, 27], while the more recent work links the divacancy to a shallower electron trap at $E_c - 0.29$ eV which anneals at 180°C[30]. An infrared absorption study has also shown a band which is attributed to an internal electronic transition at the divacancy [175]. This band anneals out at 200 K, but its assignment has been questioned by a later paper [176].

It can be expected that there are two ways in which V_2 can anneal in germanium. Firstly, it may dissociate into highly mobile vacancies. This would be expected to occur at the rate

$$R = \nu \exp(-W/k_B T), \tag{5.1}$$

where ν is an atomic jump frequency taken to be of the order of 10^{13} s^{-1}, W is the energy barrier for the process, and $k_B T$ has its usual meaning. This leads to an activation energy of $W \sim 1.3$ eV for V_2 annealing around 150 to 180°C in 15 minutes. Secondly, if V_2 anneals by migration to a trap, the prefactor would be reduced from

ν as the defect must make a number of migratory jumps before reaching a trap. Assuming a trapping centre density of $\sim 10^{18}$ cm^{-3}, the prefactor would decrease by a factor of about 10^4. This gives an energy barrier for diffusion of V_2 of $\sim$ 1.0 eV for V_2 to anneal at the temperatures observed.

It is interesting to compare the annealing behaviour of V_2 in germanium with that in silicon. The energy barrier for reorientation of V_2 in silicon is 1.3 eV and the process involves a single lattice jump. The dissociation barrier is at least 1.6 eV. Thus, in oxygen rich silicon, the defect anneals around 300°C through a migration mechanism with a barrier of 1.3 eV [36].

This section will discuss research performed to investigate a similar picture for the annealing behaviour of the V_2 defect in germanium. It will also look at the suitability of the supercell as a method in which to study charged and migrating defects in germanium. This work has been published in Materials Science in Semiconductor Processing and Physical Review B [177, 178].

5.3.1 Results

5.3.1.1 Supercell Calculations

Binding energies in the supercell calculations were calculated by both methods described in Section 3.3.3. From the first method, comparing the formation energies of the component defects, a binding energy of 0.6 eV was obtained. Using the second method, with a separation of four atomic positions along a $\langle 110 \rangle$ chain, a binding energy of 0.7 eV was calculated. This shows that the vacancies are essentially free at this separation, in line with previous work on V_2 in silicon [38]. This method was also applied to study charged defects, but only negligible changes in formation and binding energies were observed for any of the charge states examined.

Migration energies were calculated by the NEB method. The end points used were relaxed divacancies separated by one atomic jump, so a single Ge atom traverses the divacancy in each diffusion step. Figure 5.1 displays the shape of the migration

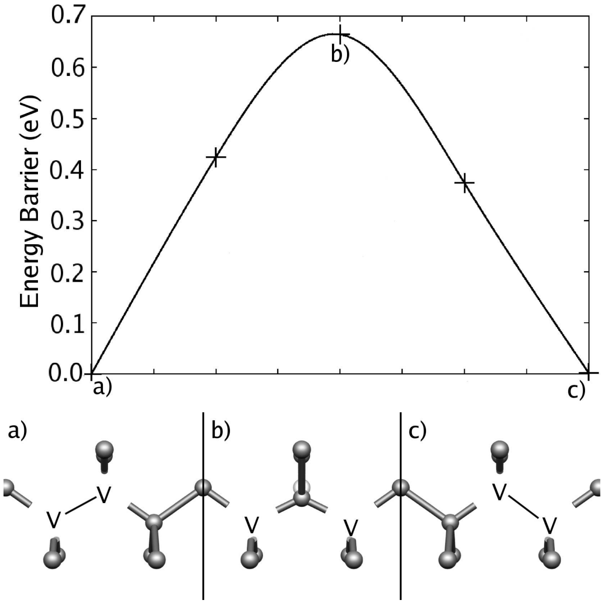

Figure 5.1: Top: Diffusion barrier shape for the divacancy in the supercell. Bottom: Atomic configuration of a) the initial structure, b) the saddle point, c) the final structure. The faded atom in the saddle-point configuration indicates the undisturbed crystal position as an aid to the reader.

barrier and the saddle point configuration. The saddle point was seen to be very close to the configuration with two vacancies at second-neighbour sites in the crystal. The energy barrier was found to be 0.7 eV.

5.3.1.2 Band Structure Analysis

In order to check the validity of the supercell results, the band structure of a supercell containing V_2 was calculated and is plotted in Figure 5.2 along with the valence and conduction bands of a bulk supercell. The levels introduced by the divacancy into the band gap are seen to cross into the valence band for a range of $\mathbf{k}$ values along the symmetry directions sampled. This includes the Γ-point and at least one of the Monkhorst-Pack (MP-2^3) sampling points. This is almost certainly an erroneous result due to the underestimation of the band gap within the supercell methodology. This explains the insensitivity of the formation and binding energies found above to charge state. It also brings the results of the migration energy of neutral V_2 given above into question.

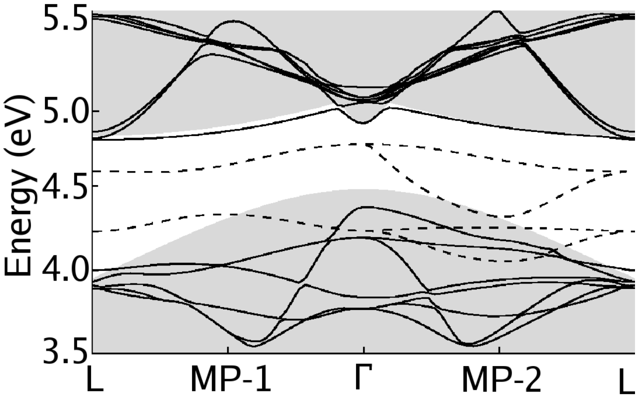

Figure 5.2: Band structure for the divacancy (lines) between the Γ point and two *L* points. The valence and conduction bands of the perfect crystal are presented for comparison (shaded regions). Indicated on the x-axis are two of the sampling points used in the MP-2^3 scheme. As can be seen, the conduction band energy levels are barely affected by the introduction of the divacancy to the system, while the valence band energy levels are strongly distorted. Defect-related states (dashed lines) are seen to lie within the valence band at the Γ-point and one of the two MP-2^3 sampling points shown.

5.3.1.3 Cluster Calculations

In the cluster calculations, it is only possible to calculate binding energies using the method of separating defects within the same system. In order to examine the effect of defect-surface interactions on the V_2 binding energy within germanium clusters, the energy increase with defect separation was calculated for clusters with strained surface bonds, and the results are summarised in Table 5.1. In the fourth nearest neighbour configuration, where the vacancies are considered to be separate, each vacancy is at a third neighbour site to an immobile surface Ge atom. It is therefore not expected for the energy difference to exhibit complete convergence, and the energy difference between the fourth and fifth neighbour configurations is considered to be dominated by vacancy-surface interactions. The difference between these energies allows an estimation of the contribution of surface interaction on the binding energy to be made, and suggests an overestimate of $\sim$ 0.2 eV from this source.

Table 5.1: Table showing the increase in energy upon moving the divacancy from the first nearest neighbour out to a fifth nearest neighbour configuration along a ⟨110⟩ chain.

Separation	Energy (eV)
1	-
2	1.06
3	1.29
4	1.53
5	1.61

Table 5.2: Binding (E_b), migration (E_m) and symmetry constrained saddle point (E_{scsp}) energies, in eV, of the divacancy found in 501 atom clusters with strained surface bonds, relaxed surface bonds and fully relaxed surfaces for various charge states.

Surface	Charge	E_b	E_m	E_{scsp}
Strained	+	-	-	1.0
	0	1.5	1.1	1.1
	−	-	1.2	1.2
	=	1.6	1.3	1.3
Relaxed Bonds	0	1.7	-	1.1
	=	1.8	-	1.3
Relaxed Surface	0	1.7	-	1.1

To avoid spurious charge transfer between the vacancies, only evenly charged states were calculated with this method. Results are given in Table 5.2 for binding energies calculated in all three cluster types. Three surface conditions were used in these calculations in order to investigate their effect on the processes being studied. The fully relaxed surface calculations also allow an estimation of the effect of the lattice parameter used to construct the clusters.

The binding energies show an increase in stability with the more negatively charged states, and are also notably higher than the supercell case. Results calculated in clusters with relaxed surface bonds and fully relaxed surfaces show an increase in binding energy. No differences were calculated between the clusters with relaxed bond lengths and those with fully relaxed surfaces, and energy changes with different charge states were not sensitive to surface treatment.

Migration energies were calculated with the migration occurring symmetrically about the centre of the cluster. The saddle point was again shown to be close to the second nearest-neighbour configuration having C_{2v} symmetry. Symmetry-constrained relaxations were performed with this configuration, and the energy difference from the bound divacancy is reported in Table 5.2 ($\mathrm{E}_{\mathrm{scsp}}$) along with the migration energies. As can be seen, the barrier calculated by the NEB method and those calculated by this relaxation are in excellent agreement, and some migration barriers were calculated solely by this method. Comparing the results calculated for different surface conditions reveals a negligible change in the migration barrier between the systems for any charge state investigated, of the order of ±0.03 eV.

Similarly to the binding energies, the migration energies show an increase as the charge state becomes more negative.

The divacancy is seen in these calculations to be unstable against Jahn-Teller (JT) distortions. These involve spontaneous lowering of the symmetry of the system accompanied by a lowering in the energy as dangling bonds on the Ge atoms surrounding the divacancy interact. As shown in Figure 5.3, the JT distortions maintain the reflection symmetry with a plane of reflection through the b and b' atoms. If, as shown in Figure 5.3, the atoms move such that $ab = bc < ac$ (and likewise $a'b' = b'c' < a'c'$), the distortion forms a resonant bonding (RB) structure, as there is a resonant reconstructed bond between the three atoms. If instead, the atoms move in the opposite sense, such that $ab = bc > ac$, there is instead a pairing bond between atoms a and c, and this distortion forms a pairing structure.

It is shown in Table 5.3 that the neutral divacancy is seen to relax into a RB configuration in most cluster calculations. In charged cluster calculations and neutral calculations with relaxed surface bonds, however, no significant distortion was observed. Also of note from these results is the increased relaxation going from the singly to doubly negative case and in the cluster with a fully relaxed surface. Given

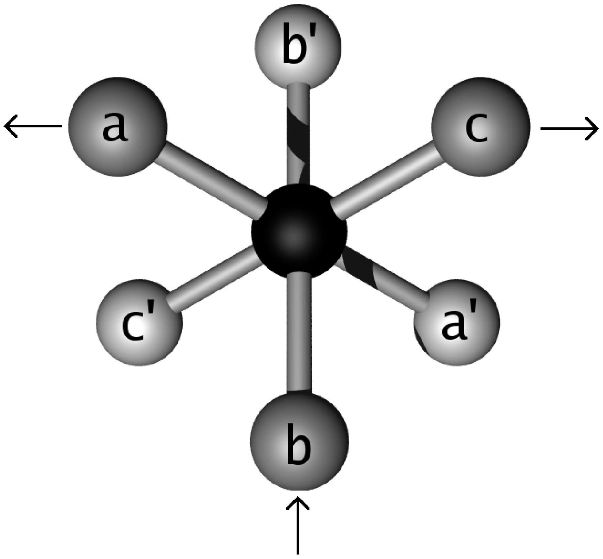

Figure 5.3: Diagram showing and end-on view of an undistorted divacancy. The vacancy sites (black) are surrounded by three Ge atoms at each end (light and dark grey, respectively). The JT distortions observed in the divacancy preserve the reflection symmetry plane containing the two vacant sites and the atoms b and b'. Resonant bonding occurs when $ab = bc < ac$, as indicated by arrows in the diagram.

the energy differences observed in the cluster calculations with different surface conditions, it is seen that the contribution from these changes must be very slight.

5.3.2 Discussion

The structures resulting from the calculations presented here show slightly smaller JT distortions than those presented in one previous theoretical work on the divacancy [10], although another, more recent study gives results that are very similar to those found here [174].

The supercell calculations showed that the vacancies are essentially free at fourth neighbour separation, similar to earlier results in silicon [38]. Binding and migration energies of about 0.7 eV were found for the neutral and charged defects. Taking a neutral vacancy migration barrier of 0.4 eV from supercell calculations in the literature [170], gives a dissociation energy of V_2 of about 1.1 eV. The migration

Table 5.3: Inter-atomic distances for atoms surrounding the divacancy in angstroms and as percentages of unrelaxed values, using the the labelling scheme from Fig 5.3. Results are presented for different charge states and surface conditions.

Method	Charge	*ab*	*ac*	*aa′*
Supercell	0	3.19 (81%)	3.33 (84%)	5.40 (89%)
Cluster with Strained Surface	+	3.77 (95%)	3.77 (95%)	6.00 (98%)
	0	3.60 (90%)	3.77 (95%)	5.86 (95%)
	−	3.60 (90%)	3.60 (90%)	5.78 (94%)
	=	3.53 (88%)	3.53 (88%)	5.67 (92%)
Relaxed Bonds	0	3.73 (94%)	3.73 (94%)	5.93 (96%)
	=	3.53 (89%)	3.53 (89%)	5.66 (92%)
Fully Relaxed Surface	0	3.31 (83%)	3.75 (94%)	5.70 (93%)

barrier for the the V_2 defect was calculated to be 0.7 eV. These are both below the experimental values deduced from the V_2 annealing temperature, and would correspond, instead, to annealing temperatures of 90 and 30°C respectively. Band structure calculations for supercells containing a divacancy showed that the energy levels introduced into the band gap by the divacancy crossed into the valence band for a range of **k**-points, including some used for sampling the Brillouin Zone.

Migration barriers from cluster calculations were found to be largely insensitive to surface conditions, yielding essentially the same results for clusters with strained or relaxed Ge-H bonds and with fully relaxed surfaces. Binding energies of both neutral and charged defects deduced from runs where the vacancies are separated at fourth neighbour were not strongly affected by the method used to treat the cluster surface. Therefore, it is deduced that the effect of the surface bonds on migration and binding energies is minimal, as is that of the choice of lattice constant used in the initial construction of the cluster. It is estimated that interaction between the separated vacancies and the cluster surface causes an 0.2 eV overestimate of the binding energy of the vacancies in V_2.

The charge dependence of the migration barrier of the divacancy is found to be opposite to that found by AIMPro calculations for the single vacancy in germanium

[170]. This trend in the divacancy case can be explained by considering the structure results above along with the migration path observed. The relaxations increase the energy of migration by reducing the space through which the mobile atom can move, thereby increasing the distortion required to allow it to pass. Increasing relaxation in more negative charge states further increases this barrier.

The dissociation energy found by the cluster method is the binding energy plus the migration energy of a single vacancy taken from cluster calculations reported in the literature [170] to be 0.7 and 0.4 eV in the neutral and singly negative charge states respectively. This gives dissociation barriers of 2.0 and 1.8 eV for the neutral and doubly negative divacancy when the overestimation from the surface interactions is taken into account. The migration barrier for the divacancy is found to rise from 1.1 to 1.3 eV in the neutral to doubly negative charge states. These suggest annealing temperatures by dissociation of 390 down to 360°C for the neutral to doubly negative defect, and by migration of 200 to 290°C. The neutral migration temperature is then in fair agreement with the experimental values of 150 to 180°C[26, 27, 30], suggesting that this is the annealing mechanism observed in the experimental work.

These results support the evaluation made above and explained in Section 3.2 that the cluster-based calculations are more reliable than the supercell for calculations in germanium. Using the cluster methodology allows the calculation of energy barriers for divacancy diffusion and dissociation, and thence a determination of the atomic-scale processes involved in the annealing observed in experiment.

5.4 Vacancy Clustering

Beyond the divacancy, small vacancy clusters form during annealing, and it is these V_n ($n \leq 10$) clusters on which this Section will concentrate. A recently published study using a variety of experimental techniques provides evidence for vacancy clustering in highly damaged germanium [142]. DLTS and high resolution Laplace DLTS (LDLTS) on neutron irradiated, *n*-type samples revealed a broad band of levels lower in the band gap than the level attributed to the divacancy after high neutron dose irradiation, though no exact position was calculated. Due to the shape of the peak, it is believed to be due to an extended or inhomogeneous defect, and is attributed to a vacancy cluster. Positron annihilation spectroscopy performed on the highly irradiated samples revealed the growth of larger vacant regions after annealing at 200°C, believed to be of the order of 10 vacancies in size. The authors attributed the formation of these defects to the creation of localised regions of type inversion. As all reported irradiation damage-induced defects act as acceptors, they will lower the Fermi level, and also be negatively charged. In local regions of sufficient damage in *n*-type material, the Fermi energy will be lowered to the point where some of the defects will become neutral, and will then be able to merge and form larger defect clusters. Other DLTS studies have attributed acceptor levels at $E_v + 0.20$ and $E_v + 0.24$ [19] or $E_v + 0.37$ eV [30] to V_2. A later paper by the second group attributed the $E_v + 0.37$ eV level to a larger vacancy cluster and suggested that the divacancy levels would lie in the lower half of the band-gap, an opposite trend in the position of the acceptor level to that suggested by the first results discussed [31]. Single vacancies have also been linked to a defect level at $E_v + 0.2$ eV [179], $E_v + 0.14$ eV [12] or $E_v + 0.33$ eV [180].

This Section will describe work to investigate the formation energies and acceptor levels of small V_n clusters, and the stability of the defects. A brief investigation of the effect of altering the basis set used to model the electronic wave functions around the Ge atoms is also discussed. Previous theoretical work has placed the first and second acceptor levels of V_1 both at around 0.2 eV above the valence band top or at $E_v + 0.37$ and 0.40 eV [5, 180] and V_2 at around 0.3 eV [174].

5.4.1 Results

The structure used for the V_n clusters is shown in Figure 5.4, and was chosen to minimise the number of broken bonds for any size of the cluster. Figure 5.5 shows the formation energy, calculated per vacant site in the cluster, for clusters ranging in size from single vacancies up to n=14. Also included is the number of dangling bonds per vacancy in the cluster. Due to the structure of the cluster, the V_n clusters with

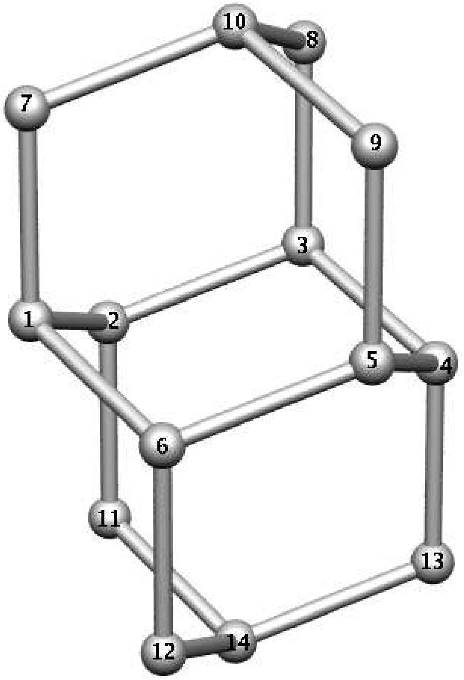

Figure 5.4: Diagram showing the structure of the V_n clusters for $n \leq 14$. The clusters were formed by the removal of atoms from the cluster or supercell in the order as indicated by the numbers on the atoms.

n=6, 10 and 14 form closed shells of vacancies, and hence dip below the overall trend for the number of dangling bonds per vacancy. Comparing this with the formation energy per vacancy in the defect, it can be seen that these clusters exhibit local energy minima with respect to cluster size. It is also the case that for every cluster size studied, $E_f(V_n) < E_f(V_{n-1}) + E_f(V_1)$. That is, there is no cluster size at which a vacancy is not bound to the cluster, with the smallest binding energy calculated as 0.3 eV for the 11th vacancy in V_{11}.

The single and double acceptor levels calculated for the vacancy clusters are shown in Figure 5.6. Alternative calculations were performed with a larger basis set for the electronic wave functions around the Ge atoms for the V defect using the VO acceptor levels as markers. Using an uncontracted basis set for the germanium atoms with four each of the s, p, d orbitals made almost no difference to the results obtained, with differences of under 0.1 eV for each energy level.

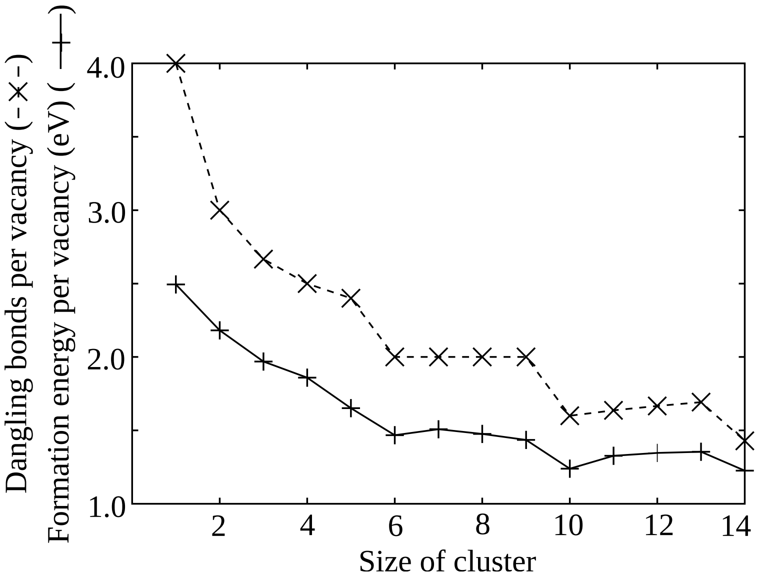

Figure 5.5: Formation energy (solid line) and dangling bonds (dashed line) per vacancy for V_n clusters up to n=14. Of note is that while both values decrease with increasing cluster size, they also show correlation for structures where the number of dangling bonds dips, at six, ten and fourteen vacancy-clusters.

As n increases, both of the levels are seen to move down in the band gap, and for larger clusters modelled with the VO marker, drop below the top of the valence band. The Au marker gives higher energy levels, but also gives a negative-U [14] ordering across all the clusters studied. Beyond $n = 6$, the second acceptor level is calculated with Au to lie within the valence band. Anomalous results are seen at n=5 and $n = 9$ where the second and first acceptor levels respectively are found to lie well below the broad trend predicted by other cluster sizes. It is not clear whether these results are due to a real physical effect or are an artifact of the modelling method.

5.4.2 Discussion

Comparing these results with prior experimental data, it can be seen that the Au marker gives acceptor levels closest to the measured levels at 0.2 eV [179] or 0.14 eV [12] above the valence band. The levels calculated using the VO marker are found to be lower in the band than any experimentally observed levels, while the level observed at $E_v + 0.33$ eV is higher than any calculated here. The levels attributed

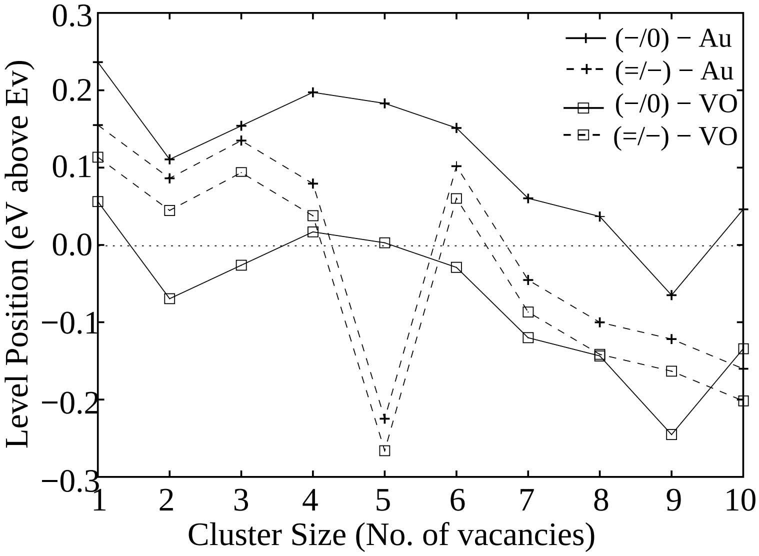

Figure 5.6: First (solid line) and second (dashed line) acceptor levels for V_n clusters up to n=10, calculated in eV from the top of the valence band using Au (crosses) and VO (squares) as markers. The dotted line indicates the top of the valence band. Of particular note are the anomalous results for the second acceptor level at n=5 and the first acceptor level at n=9.

to V_2 at $E_v + 0.20$ and 0.24 eV [19] or $E_v + 0.37$ eV [30] are notably deeper than the results calculated with either marker, and with an overall downwards trend in the position of the acceptor levels with increasing cluster size, the $E_v + 0.37$ eV level [31] does not match any vacancy cluster calculated.

Comparing the results with previous theoretical work, the levels for the single vacancy are the same as those found in previous work using the same method [5] and significantly lower than those calculated using the formation energy method [9]. The acceptor levels of the divacancy defect are calculated to be shallower than the single vacancy, and shallower than previous results of ∼0.3 eV above the valence band [174].

A more in-depth comparison of the model proposed by Peaker *et al* [142] with our results suggests that small clusters of up to 14 vacancies are stable with respect to smaller isolated clusters in the neutral charge state. The formation of these vacancy clusters in n-type material would seem to require areas of type inversion to allow the diffusion of small neutral vacancy clusters to larger defects without Coulomb repulsion, as suggested.

In conclusion, we have studied the formation energies of vacancy cluster defects V_n, with $1 \leq n \leq 14$ and acceptor levels for clusters with n up to 10. It is calculated that the clusters are stable in the neutral charge state with respect to V_{n-1} clusters and isolated single vacancies. The clusters with $n = 6, 10$ and 14 are particularly stable, coinciding with local minima in the number of dangling bonds per vacant site in the cluster. The acceptor levels were calculated to move down the band gap with increasing cluster size, with the second acceptor level entering the valence band at $n = 6$ and lying below the first acceptor for all values of n.

5.5 Self Interstitial Diffusion

While the self interstitial (I) has not been conclusively observed in experiment in germanium, there has been some interest from modelling groups to understand how this fundamental defect behaves differently in germanium and silicon, where in the latter it is a much more important defect. In the neutral charge state, a number of prior works on germanium have calculated a $\langle 110\rangle$ split interstitial as the most stable form of the defect [16, 17, 181]. The defect is calculated to have a formation energy of 3.55 [17] or 3.50 eV [181].

From experiment, donor levels between $\mathrm{E_c} - 0.2$ and 0.04 eV [12, 11, 19, 18]. have been attributed to the interstitial and the migration barrier has been estimated at ∼0.6 eV [179].

5.5.1 Results

Three defect structures were studied in the neutral charge state. The $\langle 110\rangle$ split-interstitial structure (I_{110}), a T-sited interstitial (I_T) and an H-sited interstitial (I_H).

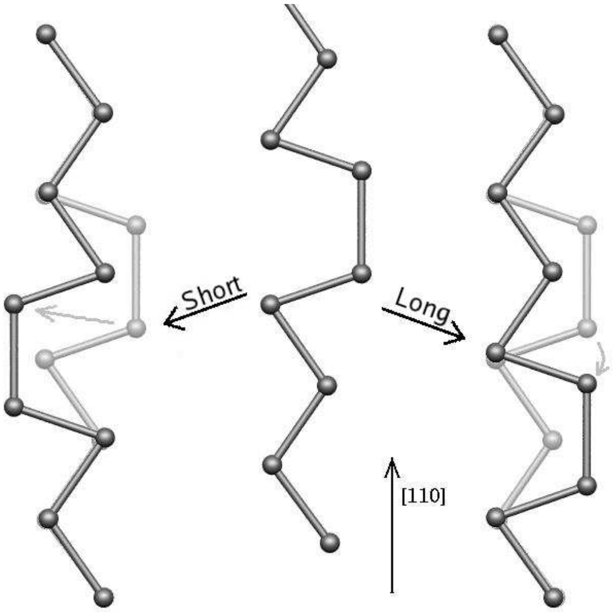

Figure 5.7: Figure depicting the ‘short’ (left) and ‘long’ (right) diffusion paths for the I_{110} defect. The faded images behind each side image are the starting point repeated as an aid to the reader.

The calculations gave the I_{110} structure as the most stable, with a formation energy of 3.60 eV compared with 3.83 eV for I_T and 4.13 eV for I_H.

Diffusion barriers were calculated for the I_{110} structure in the neutral charge state as well as for the the doubly positive I_T^{2+} as this has been calculated to be the most stable structure in an important charge state [182]. For the I_T^{2+} defect, the motion investigated consisted of motion between adjacent T-sites along the $\langle 110\rangle$ channels in the crystal. For the I_{110} defect, two diffusion steps along the $\langle 110\rangle$ chains were considered, as depicted in Figure 5.7, and a rotation between adjoining chains was also investigated.

The migration barrier for the I_T^{2+} defect was calculated to be 1.23 eV. For the I_{110}^0 defect, the ‘long’ diffusion step exhibited a barrier of 0.64 eV, the ‘short’ step 0.80 eV and the rotation between chains was calculated to proceed with a barrier of 0.75 eV. This suggests that in the neutral charge state, diffusion proceeds via the long step, with the rotation between chains occurring less frequently, but enough to allow diffusion throughout the crystal.

5.5.2 Discussion

The formation energies and structure calculated here are in good agreement with previous theoretical work giving a I_{110} structure and a formation energy of 3.50 or 3.55 eV [16, 17, 181]. Subsequent work on the germanium self-interstitial has found a more favourable diffusion path for the I_{110}^0 defect with a barrier of 0.5 eV via a metastable I_H^0 structure. A stable structure for the singly positive defect, with the interstitial atom lying between an H- and adjacent T-site ($I_{H\mathrm{d}}^+$) has also been calculated along with a diffusion path for this defect with a barrier of 0.3 eV and a saddle point at I_H^+ [183]. Energy levels have been calculated for the different defect structures. The I_{110} defect is found to be electrically inactive, and in low temperature experiments, the barrier for transformation from the split-interstitial to the caged T- or H-site interstitials can lock the defect in the I_{110} structure. At higher temperatures, the singly and doubly positive charge states of the defect become attainable as the thermal energy becomes sufficient to allow the defects to relax into $I_{H\mathrm{d}}^+$ and I_T^{2+} structures. The first donor level of these structures is calculated to lie below the top of the valence band, and the second donor level at $E_c - 0.08$ or 0.20 eV depending on the marker used [182]. Comparing these with the experimental data, it can be seen that there is good agreement between the theoretical and experimental values.

In addition to the papers referenced above, much of the work discussed in this final section has formed a section of the thesis of A. Carvalho [184].

5.6 Chapter Summary

In this Chapter, the calculated annealing behaviour of the divacancy as well as the electrical properties and formation energies of vacancy clusters were presented. Finally, details were given of some initial work done on the germanium self-interstitial, followed by a brief description of the study to which this work led.

The first notable result from the divacancy work in germanium was that on the applicability of the supercell method to calculations in germanium. Band structures calculated in the neutral supercell clearly show electron states in the valence band which are due to the divacancy. This suggests that results calculated in the supercell would be unreliable, and explains the result that the binding and migration energies calculated in the supercell are insensitive to charge state. Thus the decision was made to minimise the use of germanium supercells in further studies.

Supercell calculations are seen to predict annealing temperatures via either dissociation or migration at temperatures which are well below those observed in experiment. Cluster calculations, on the other hand, give annealing temperatures for annealing via migration to trapping defects which are in good agreement with the experimental results for the neutral charge state, supporting the decision to rely on cluster calculations and suggesting that this is the atomistic mechanism involved in the experimentally observed annealing.

The vacancy cluster calculations demonstrated a definite link between the formation energy per vacancy in the cluster and the number of dangling bonds per vacancy. As expected, the formation energy calculations showed that for every cluster up to V_{14}, the last vacancy was bound to the cluster, with the smallest binding energy being 0.3 eV for the 11^{th} vacancy in the V_{11} defect. The energy levels calculated for the clusters showed a broad downward trend of the acceptor levels, with the larger clusters having acceptor levels falling below the edge of the valence band.

The results for the self interstitial structure in germanium are in agreement with prior theoretical work on the problem, giving the $\langle 110 \rangle$ split interstitial as the most stable structure in the neutral charge state. The diffusion barrier for the defect was calculated to be 0.75 eV in the neutral and 1.23 eV in the doubly positive charge states. This formed a basis for later work by A. Carvalho in which the charge-dependent structures, energy levels and diffusion mechanics of the self interstitial in germanium were studied in detail.

Chapter 6

Dopant-Related Defects

6.1 Introduction

The study of dopant-related defects in semiconductors is a very wide-ranging subject of great importance to device behaviour. As well as removing dopants from electrically active substitutional sites in the crystal, thus reducing the active dopant concentration, defects may also actively compensate the remaining active dopants if they are themselves electrically active. In addition they may promote diffusion of the dopants, impeding the creation of small-scale sharply defined devices. Diffusion of dopants will be dealt with in more detail in Chapter 7

In germanium, the dominant intrinsic defect is the vacancy, due to its low formation energy [9, 170]. In silicon, while the self-interstitial is an important defect, the vacancy still plays an important role, and therefore this chapter will focus on vacancy-related defects in both materials, looking at their energy levels, formation paths and annealing mechanics.

6.2 Modelling Method

The silicon-based calculations of Section 6.3 were performed in 216 atom supercells while the germanium-based calculations in Section 6.4 used a combination of 216 atom supercells and 501 atom clusters. Description of the systems and other calculation parameters may be found in Section 3.4.

Formation energies for neutral defects were calculated using the method described in Section 3.3.2, migration barriers using the NEB method in Section 3.3.5 and electrical energy levels using the marker method as described in Section 3.3.4. Formation energies for charged defects were calculated using marker-method-calculated energy levels and the formation energies calculated for neutral defects. Binding energies were calculated from formation energies as described in Section 3.3.3 For germanium, the antimony E-centre (SbV) donor level at $E_v + 0.09$ eV and acceptor levels at $E_v + 0.31$ and $E_c - 0.30$ eV [50, 131] were used as markers for the phosphorus-related defects in germanium. In silicon, the phosphorus E-centre (PV) donor level at $E_v + 0.27$ eV and acceptor level at $E_c - 0.45$ eV [117] were used for all defects while the vacancy-oxygen (VO) acceptor level at $E_c - 0.17$ eV [185] and interstitial carbon (Ci) donor level at $E_v + 0.28$ eV [186] were used in addition to model the As_2V defect.

6.3 Arsenic-Boron-Vacancy defects in Silicon

One line of research performed on this topic was prompted by an interesting study involving vacancy-related defects carried out in silicon [187]. An electron beam incident on the *n*-type layer of an As/B-doped n^+p mesa diode was used to irradiate the sample while defects in the *p*-type region were monitored by DLTS. A defect level at $E_v + 0.20$ eV was observed to grow in after heat treatment at 400 K. The defect is believed to be related to the As E-centre (AsV) which becomes mobile around this temperature, and indeed the unknown defect was not observed in similarly B-doped Schottky-diodes, confirming its As-related nature. The E-centre itself was not observed in the *p*-type region, and the authors suggested that the defect is As_2V formed in the highly doped *n*-type region which could then diffuse into the *p*-type region. This is, however, contested by previous *ab initio* theoretical calculations using a different code than that employed here which yield migration energies of 1.4 or 1.3 eV for the AsV defect and 1.9 or 2.0 eV for As_2V [53, 188], implying that a significantly higher temperature would be required for As_2V to become mobile compared with AsV.

The recent discovery that the E-centre defect has in addition to the well-known acceptor level at $E_c - 0.45$ eV, a donor level at $E_v + 0.27$ eV [117] has important consequences for defect behaviour in *p*-*n* junctions. In this case, it opens up the possibility of the mobile AsV becoming positively charged in the *p*-type region and becoming Coulombically attracted to negatively charged B dopants.

The related boron-vacancy defect has been studied previously. Watkins *et al* performed electron paramagnetic resonance studies in which a signal was attributed to the BV defect [189]. The signal was seen to anneal at 260 K and the symmetry of the observed signal led to the assignment of a structure with the B atom at a second neighbour position to the vacant site. Theoretical work by Adey *et al* revealed a charge dependent structure for the defect, with the B atom at a second neighbour site to the vacancy in the positive charge state and a third neighbour site in the negative charge state [190].

In this study, the properties of AsV were studied along with those of the As_2V and AsBV defects believed likely to form when AsV becomes mobile and is able to be captured by either As or B dopants in the n^+ or *p*-doped regions respectively. Parts of this work have been published in Applied Physics Letters [191].

6.3.1 Defect Structures

In light of the previous studies on the boron-vacancy (BV) defect in silicon, six structures for the AsBV defect were studied in the singly positive, singly negative and neutral charge states. The structures are shown in Figure 6.1. The AsVB

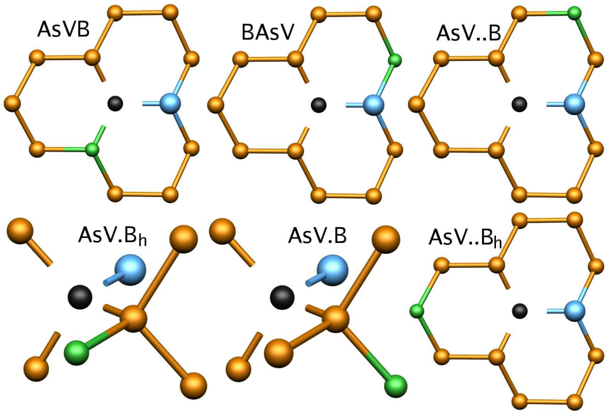

Figure 6.1: Examined structures for the AsBV defect complex. In all the images, the orange balls represent Si atoms, the black ball identifies the vacant site, the large, light blue ball represents the As atom, and the small, green ball the B atom.

structure is similar to As_2V, with the B and As atoms occupying two first neighbour sites to the vacancy. BAsV, AsV.B and AsV.B$_h$ all place the B atom at a second nearest neighbour site to the vacancy. In BAsV, the B is adjacent to the As atom, while in AsV.B and AsV.B$_h$, the B atom lies on the opposite side of the vacancy with C_1 and C_{1h} symmetry, respectively. Finally, the B atom is placed at a third neighbour site from the vacancy in the AsV..B and AsV..B$_h$ structures. In the first structure, the B atom is at a second neighbour site to the As atom, while in the latter, higher symmetry structure, it lies at a fourth neighbour site to the As.

For each charge state, the relative energies of the different structures were calculated, and the results are shown in Table 6.1. The AsV.B and AsV.B$_h$ structures are seen to be degenerate across all charge states and are the most stable structure for the defect in the neutral and singly positive charge states. AsV..B$_h$ is seen to be slightly more stable in the singly negative charge state. Barriers for reorientation of the defect are expected to be of the same order as for migration of the AsV defect and therefore much larger than the energy differences between structures. Therefore the AsV.B and AsV.B$_h$ structures (hereafter referred to collectively as AsV.B due to their degeneracy) as well as the AsV..B$_h$ structure will be considered in more depth as independent defects.

Table 6.1: Relative energies of the AsBV structures investigated in this study in the neutral, singly negative and singly positive charge states. Results are given in eV, relative to the structure exhibiting the lowest energy for each charge state.

Structure	AsVB	BAsV	AsV.B	AsV.B_h	AsV..B	AsV..B_h
$-$	0.24	0.22	0.05	0.04	0.09	0.00
0	0.08	0.39	0.01	0.00	0.20	0.15
$+$	0.09	0.37	0.01	0.00	0.20	0.14

Table 6.2: Separation between atoms for the various defects studied in the neutral charge state. All lengths are given in Å, with following brackets indicating the percentage of the unrelaxed distances. All distances apart from Si-B are for the atoms surrounding the vacancy. Si-B distances indicate the separation between the B atom and the adjacent Si atoms. Two results are given for the Si-Si length in the AsV and AsV.B complexes due to strong rebonding effects such that one length is significantly shorter than the other two.

Defect	Si-Si	Si-As	Si-B	As-As
AsV	2.91 (76%) 3.36 (88%)	3.41 (89%)	-	-
As_2V	2.84 (75%)	3.40 (89%)	-	3.45 (91%)
AsV.B	2.93 (77%) 3.95 (104%)	3.57 (94%)	2.05 (88%)	-
AsV..B_h	3.41 (89%)	3.56 (93%)	2.05 (88%)	-

For all defects studied, the positions of the atoms surrounding the vacancy were examined to investigate the nature and strength of symmetry breaking in the defects. The breaking of symmetry can be indicative of rebonding of dangling bonds surrounding the vacancy. The results for the neutral charge state are presented in Table 6.2.

In almost all cases, the vacancy relaxed entirely inward, and the inter-atomic distances decreased. The only exception is the AsV.B structure, where the B pulls the Si atom between it and the vacancy strongly away from the vacancy. The AsV and AsV.B complexes demonstrated a strong Jahn-Teller distortion, leading to one of the three Si-Si distances being significantly shorter than the other two. This suggests that rebonding occurs in these defects. This feature is also seen to be present to a similar degree in the AsV..B_h structure in the singly negative charge state, suggesting that it plays an important role in determining the lowest energy structure

Table 6.3: Donor and acceptor levels of the various defects studied. Energies given in eV. Defects in brackets indicate the markers used in the calculations.

Level	AsV	As_2V	AsV.B	AsV..B_h
$E(0/+)-E_v$	0.25	-0.05 (PV) 0.05 (C_i)	-0.10 (PV) 0.00 (C_i)	-0.10 (PV) 0.01 (C_i)
$E_c-E(-/0)$	0.40	0.01 (PV) 0.22 (VO)	-	-
$E(-/0)-E_v$	-	-	0.47	0.27

for the AsBV defect. Comparing the shorter Si-Si length in these defects to that in the As_2V defect suggests that this defect will undergo rebonding as well.

6.3.2 Energy Levels

The energy levels calculated for the various defects are summarised in Table 6.3. The AsV and As_2V levels were calculated using the donor and acceptor levels of PV. As the electronic structure of PV is not especially close to that of As_2V, the levels of this defect were also modelled using the VO defect for the acceptor level, which has a much closer electronic structure and C_i for the donor level, which has an electronic structure completely different from either PV or As_2V. These are indicated in the table. The AsBV defect was considered in either structure to consist of an As E-centre near to, but separate from a B atom. The B is expected to retain its negative charge, such that the donor level of the AsV is perturbed by its presence and is labelled the acceptor level of the AsBV defect. Thus the AsBV acceptor level is modelled using the donor level of PV as a marker, and the AsBV donor level is modelled using both PV and C_i. Of note in this model is the possibility that some experimental measurements may detect the donor level of the AsV constituent defect rather than the acceptor level of the whole defect, including the negatively charged B atom.

The calculations predict the donor levels of the As_2V and AsBV defects to all lie either below or degenerate with the top of the valence band. That the calculated levels remain effectively constant using either of two very different markers suggests that the results are accurate despite the difference in structure between the marker

Table 6.4: Formation energies of the defects studied. Results are given in eV relative to isolated $\mathrm{As}_{\mathrm{Si}}^{+}$ and $\mathrm{B}_{\mathrm{Si}}^{-}$. μ_e is the Fermi energy measured from the top of the valence band. Defects in brackets indicate the marker used in the calculation of charged states.

Charge	V	AsV	$\mathrm{As_2V}$	AsV.B	$\mathrm{AsV..B}_h$
+		2.99	$2.48-\mu_e$ (PV)	$2.78+\mu_e$	$2.92+\mu_e$
			$2.38-\mu_e$ ($\mathrm{C_i}$)		
0	3.91	$3.24-\mu_e$	$2.43-2\mu_e$	2.68	2.87
−		$3.96-2\mu_e$	$3.55-3\mu_e$ (PV)	$3.15-\mu_e$	$3.09-\mu_e$
			$3.34-3\mu_e$ (VO)		

and the defect being studied. The acceptor level of the $\mathrm{As_2V}$ defect is seen to vary with the marker used, but the VO marker is expected to yield more reliable results due to the similarity in electronic structure between it and the $\mathrm{As_2V}$ defect.

6.3.3 Formation Energies

Formation energies of the defects are given in Table 6.4. The results are given in terms of μ_e, the Fermi energy measured from the top of the valence band. The results show that each As atom is strongly bound to the vacancy. Assuming a value of μ_e of around 1 eV for the *n*-type material where these defects are expected to form, the results are in good agreement with previous non-AIMPro theoretical values of 2.3 [53] or 2.4 eV [188] for AsV, and fair agreement with a prior result of 0.8 eV [53] for $\mathrm{As_2V}$. Boron is found to be rather less strongly bound to the defect, but the AsBV defect should still be bound for the low values of μ_e expected in the *p*-type region where this defect is formed.

6.3.4 Migration Energies

Migration energies were calculated for the AsV and $\mathrm{As_2V}$ defects. The migration of AsBV was not studied as the low binding energy calculated suggests that the defect would dissociate into substitutional $\mathrm{B_{Si}}$ and AsV before it diffused as a unit. Migration is predicted to proceed via diffusion of the vacancy around the six-membered

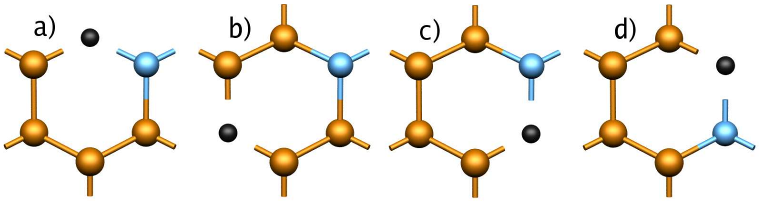

Figure 6.2: Diffusion path for the AsV defect in silicon. The smaller, orange balls represent Si, the larger, blue one As and the black ball marks the vacant site. Images a) to d) show one diffusion step as the vacancy moves around the six-membered ring and then exchanges position with the associated As atom.

rings of the diamond structure. For AsV there is only one path this can take, illustrated in Figure 6.2, while for As_2V, there are two paths. The reorientation path is shown in Figure 6.3a),b),c),d) and is a process by which the defect can change the six-membered rings it lies on without changing the position of the central vacancy. The rotation path is shown in Figure 6.3a),b),e),f) and results in net motion of the defect around one of the six-membered rings on which it is located. As the As_2V defect lies on two of these rings, diffusion can proceed by the rotation path alone, but the reorientation path can accelerate the process if the associated energy barrier is equal or less than that for the rotation path.

For AsV diffusion, the barrier was found to be dominated by the motion of the vacancy to the third neighbour site of the As atom and back. In the singly positive charge state, the barrier was calculated to be 0.9 eV, rising to 1.2 and 1.3 eV in the neutral and singly negative charge states respectively.

As_2V diffusion is also dominated by the motion of the vacancy to the side of the six-membered ring furthest from the As atoms. Calculations for the As_2V diffusion were carried out only in the neutral charge state, and gave a barrier of 2.2 eV for the rotation diffusion path and 2.5 eV for the reorientation path. This suggests that diffusion will occur primarily without the aid of the accelerating reorientation step, with a barrier of 2.2 eV.

Total barriers for As to diffuse via either of these diffusing defects are calculated by summing the formation energy of the defects and their diffusion barriers, and

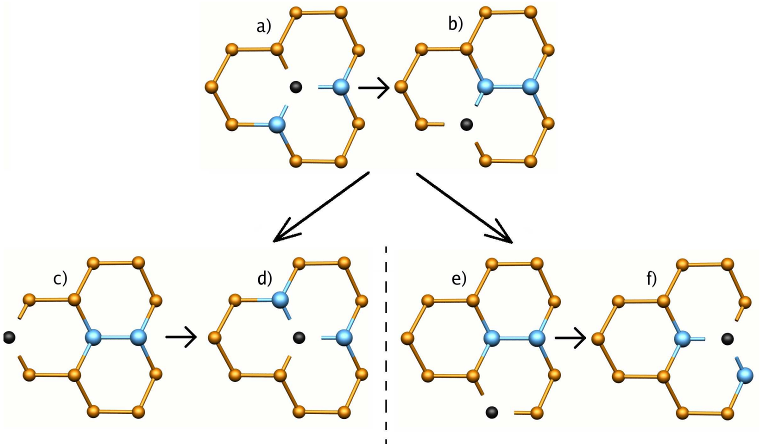

Figure 6.3: Diffusion path for the As_2V defect in silicon. The smaller, orange balls represent Si, the larger, blue one As and the black ball marks the vacant site. Images a),b),c),d) show the reorientation of the defect from one hexagonal ring to another via the net motion of As atoms only. Images a)b)e)f) show the motion of the complex around a single six-membered ring. The former process is not required for diffusion of the defect, but may act to enhance the motion if the associated energy barrier is low.

Table 6.5: Table giving total diffusion barriers for As via the formation of AsV and As_2V defects, relative to $\mathrm{As}_{\mathrm{Si}}^{+}$ in eV.

Charge	AsV	As_2V
+	3.89	
0	$4.44 - \mu_e$	$4.63 - 2\mu_e$
−	$5.26 - 2\mu_e$	

are given in Table 6.5. It can be seen there that for $\mu_e > 0.4$ eV, the total barrier for diffusion via neutral As_2V will be lower than that for any charge state of AsV calculated.

6.3.5 Discussion

The structures calculated for the AsBV defect in various charge states correlate excellently with those calculated previously for the BV defect in silicon [189, 190]. The inter-atomic distances calculated (Table 6.2) suggest that the presence of rebonding between Ge atoms around the vacancy plays an important role in determining the most stable structure of AsBV and is also present in AsV and As_2V, which are observed to be highly stable.

The As_2V energy levels calculated give a donor level close to the band edge, and an acceptor level at $E_c - 0.22$ eV using the VO marker. This level is notably above that calculated by earlier non-AIMPro modelling work of $E_c - 0.39$ eV [192] but quite close to a level assigned to the defect from experimental work at $E_c - 0.17$ eV [193]. The AsV acceptor level calculated to lie at $E_c - 0.40$ eV is in similarly good agreement with experimental work suggesting $E_c - 0.47$ eV [117].

The migration barrier for the AsV defect, calculated to be 1.2 eV for the neutral defect, and 0.9 and 1.3 eV for the singly positive and singly negative charge states is in good agreement with previous non-AIMPro modelling work which gave 1.4 [53] and 1.19 eV [188] in the neutral charge state. Similarly, the As_2V diffusion barrier is in fair agreement with the previous work giving 1.9 [53] and 2.2 eV [188] barriers for diffusion in the neutral charge state. The total diffusion barriers for As via the formation of these defects suggest that for μ_e above 0.4 eV, the most favourable diffusion path is that which proceeds via the formation of As_2V defects. This is in agreement with some earlier calculations [53], but we have not considered the alternative paths for enhanced AsV diffusion proposed later [188].

A previous experimental study on As diffusion under highly *n*-type conditions in silicon reported an estimated barrier of 2.7 eV [194]. Comparing this with the results for As diffusion via AsV and As_2V defects reported in Table 6.5, the barrier for As_2V at $\mu_e \sim 1$ eV is closest to the experimental result, while the barriers calculated for AsV diffusion approach the experimental value only for μ_e at the conduction band in the singly negative charge state.

To estimate the temperature at which a defect is expected to anneal by diffusion, we suppose that the number of diffusion steps N taken in a time Δt is given by

$$N = \nu \Delta t e^{-W/k_B T}, \tag{6.1}$$

where ν is an atomic vibration frequency, taken to be 10^{13} s^{-1}, W is the energy barrier for defect migration and k_B and T have their usual meanings. If the defect must make $\sim 10^3$ steps to encounter an annealing centre in heavily doped material, for an annealing time of 30 minutes we predict, using thermal migration barriers given above, annealing temperatures of ∼75-225°C for the AsV defect in different charge states and ∼575°C for the neutral As$_2$V defect. These results are quite close to the 175-225°C observed by experiment for AsV, but higher than the observed temperature of 420°C for As$_2$V diffusion [52].

With regard to the experimental work on As/B-doped n^+p mesa diodes discussed above, our results cast doubt on the assignment given to the new level [187]. The As$_2$V defect is not calculated to have a donor level within the gap, nor to be mobile until temperatures significantly higher than those for AsV diffusion. Conversely, the acceptor level of the AsV..B$_h$ defect calculated to lie at $E_v + 0.27$ eV seems to be in the correct range, and may exhibit donor-like ionisation behaviour; but it is not clear how the defect could form during the annealing process without the AsV defect being observed alongside it by the DLTS measurements.

6.4 Donor-Vacancy Clusters in Germanium

While p-type doping in germanium can be achieved to a high level of active acceptor concentration and shallow junction depth using boron as a dopant [65, 67], the same is not true of n-type regions. An activation ceiling of around 10^{19} cm^{-3} is measured by SRP in experiments using ion beam implantation methods, with large proportions ($\sim 90\%$) of the total implanted donor atoms as measured by SIMS remaining inactive for rapid thermal annealing (RTA) processes below 700°C[59]. The inactive donor fraction is expected to be in the form of donor aggregates or large donor-vacancy complexes and a study of the latter will form the remainder of this chapter.

In silicon, there has been a detailed PAS study on the evolution of vacancy-related defects in material heavily n-doped using phosphorus, arsenic and antimony [52]. A series of defects were identified by their distinctive W and S-parameters. The single donor-vacancy defect, DV (D=P, As or Sb) or the E-centre is the first to appear, and anneals at around 150°C. For sufficiently high doping levels (10^{20} cm^{-3}) D_2V complexes grow in, followed by D_3V complexes when D_2V anneals at 400°C. The D_3V complexes anneal out at around 800°C, coinciding with a strong recovery of active dopants as detected by electrical measurements [51]. Larger defects tentatively identified as As_5V_2 have also been observed in very heavily ($> 10^{20}$ cm^{-3}) As-doped material, but the As_3V defects are the dominant vacancy-related defects in this material [51]. D_3V has been calculated by *ab initio* methods to have a negative formation energy with respect to substitutional donor atoms in both silicon and germanium [53, 54], with arsenic and antimony donors, respectively, suggesting that it will be as important a contributor to the inactivity of dopants in germanium as silicon.

In germanium, the same detailed experimental investigation has not been performed, but there have been a number of theoretical modelling studies on donor-vacancy defects. An AIMPro study established structures with two substitutional antimony atoms both adjacent to a vacant site as the most stable structure for the Sb_2V defect [54]. While another similar study has suggested a similar structure for the E-centre, with a single donor atom adjacent to a vacant site [103]. This is supported by recent non-AIMPro studies [55], while similar earlier studies suggested a split-vacancy structure for the antimony E-centre, wherein the donor atom lies in the centre of a divacancy, at what would be the bond centre for the two absent atoms [195]. Also of interest in one of these studies is the apparent stability of Sb_5V with respect to Sb_4V and Sb_{Ge} [55]. The energy binding the fifth Sb atom to the defect is rather small, and the corresponding defects with P or As as the donor atoms are not stable, suggesting that this may be a strain-related effect. However, since the largest single vacancy defect observed in silicon is the D_3V centre and there is no clear formation mechanism for even the D_4V defect, D_5V has not been studied here.

This work seeks to investigate the behaviour of phosphorus-vacancy clusters (P_xV_y, $x \leq 5$, $y \leq 2$) to understand their contribution to donor deactivation in germanium and their thermal evolution. Parts of this work are awaiting publication in Materials Science in Semiconductor Processing [196].

Table 6.6: Calculated energy levels for a number of P_xV_y clusters. Energies are given in eV above the valence band top.

Level	PV	P_2V	P_3V	P_4V
$(0/+)-E_v$	0.13	-0.26	0.06	-0.57
$(-/0)-E_v$	0.43	0.50	0.31	1.62
$(=/-)-E_v$	0.38	0.47	1.51	1.49

Level	P_3V_2(2,1)	P_3V_2(3,0)	P_4V_2(2,2)	P_3V_2(3,1)	P_5V_2
$(0/+)-E_v$	0.01	0.15	-0.01	-0.34	0.06
$(-/0)-E_v$	0.26	0.49	0.40	0.55	0.32
$(=/-)-E_v$	0.48	0.41	0.31	0.54	1.47

6.4.1 Energy Levels

The P_xV_y defects studied were considered to consist of x P atoms in substitutional positions immediately adjacent to the vacant sites. This structure has been calculated to be the most stable for PV and Sb_2V defects [54, 103], and it is believed that these structures will continue to be the most stable for larger defects. There are two possible structures for each of the P_3V_2 and P_4V_2 defects, with different numbers of P atoms around each vacant site. These structures are denoted with numbers in brackets to indicate the number of P atoms around the first and second vacant site.

The energy levels of the various P_xV_y defects were calculated and are presented in Table 6.6. All the defects are modelled using the SbV donor level at $E_v + 0.09$ eV and acceptor levels at $E_v + 0.31$ eV and $E_v + 0.36$ eV ($E_c - 0.30$ eV) as markers [50, 131].

All of the defects studied except for P_4V are calculated to insert acceptor levels into the band gap, and several of them are predicted to become doubly negatively charged for Fermi level positions achieved in n-type regions. For PV, these values are in good agreement with experimental results of $E_v + 0.35$ and $E_c - 0.23$ eV ($E_v + 0.43$ eV) [50] for the first and second acceptor levels. For P_4V, the electrical inactivity is easily explained by noting that all the dangling bonds surrounding the vacancy have been removed by P atoms.

Table 6.7: Formation energies calculated for the P_xV_y clusters being studied. Energies are given with respect to isolated P^+_{Ge}

Charge	PV	P_2V	P_3V	P_4V	
+	2.10	$2.04-\mu_e$	$1.45-2\mu_e$	$1.49-3\mu_e$	
0	$2.23-\mu_e$	$1.78-2\mu_e$	$1.51-3\mu_e$	$0.92-4\mu_e$	
−	$2.66-2\mu_e$	$2.28-3\mu_e$	$1.82-4\mu_e$	$2.53-5\mu_e$	
=	$3.04-3\mu_e$	$2.74-4\mu_e$	$3.34-5\mu_e$	$4.03-6\mu_e$	
Charge	P_3V_2(2,1)	P_3V_2(3,0)	P_4V_2(2,2)	P_4V_2(3,1)	P_5V_2
+	$2.99-2\mu_e$	$2.69-2\mu_e$	$2.61-3\mu_e$	$2.69-3\mu_e$	$2.08-4\mu_e$
0	$3.01-3\mu_e$	$2.84-3\mu_e$	$2.60-4\mu_e$	$2.36-4\mu_e$	$2.13-5\mu_e$
−	$3.26-4\mu_e$	$3.33-4\mu_e$	$3.00-5\mu_e$	$2.90-5\mu_e$	$2.51-6\mu_e$
=	$3.74-5\mu_e$	$3.74-5\mu_e$	$3.31-6\mu_e$	$3.44-6\mu_e$	$3.99-7\mu_e$

6.4.2 Formation Energies

Formation energies are calculated as described above, and summarised in Table 6.7. All the defects are seen to be stable with respect to smaller component defects or an appropriate number of isolated lattice vacancies and substitutional P^+_{Ge}. For sufficiently large values of μ_e, the P_3V, P_4V and P_5V_2 defects are calculated to exhibit negative formation energies, indicating that they are more stable than 3,4 or 5 isolated P^+_{Ge} atoms with no vacancies. While this does not suggest that the defects will form spontaneously, due to kinetic considerations, it does suggest that these defects will contribute significantly to the deactivation of phosphorus in germanium if they are able to form.

6.4.3 Migration Energies

Migration paths for the PV and P_2V defects similar to those for AsV and As_2V in silicon, described in Section 6.3.4 were considered.

For the PV defect, the barriers for both the motion of the vacancy out to a third-neighbour distance to the P atom and for the exchange of the P atom across the vacancy were calculated. The diffusion was considered in the neutral, singly and doubly negative charge states. In all these states, the barrier for the exchange of

P across the vacancy dominated the barrier for motion out to third neighbour and back. The barrier for diffusion of the PV E-centre is then 1.6, 1.3 and 1.0 eV in the neutral, singly negative and doubly negative charge states respectively.

The P_2V complex was found to diffuse with more complex barriers, shown in Fig 6.4, for the neutral charge state while the singly and doubly negative charge states exhibit barriers of a very similar form and magnitude. As for As_2V, the barrier for both the reorientation and rotation processes were calculated, and also as for As_2V, the diffusion of the defect does not require the reorientation step to proceed. As can be seen, the defect passes over a number of increasingly high barriers, with the highest barrier lying as the vacancy moves furthest from the P_2 centre. The vacancy's subsequent return to the P_2 pair is then a symmetric reversal of the outward journey. The reorientation step is again seen to exhibit a significantly higher energy barrier, and so it is not considered to contribute to the diffusion of the complex. Therefore the calculated barrier for P_2V diffusion in the neutral state is 1.8 eV. In the singly and doubly negative states, the reorientation barrier changes by less than 0.1 eV, while the barrier for the rotation step drops to 1.7 eV for both of these charge states. It can therefore be said that the diffusion of the P_2V defect is not affected by charge state, and once formed, the defect should diffuse at a rate insensitive to the local doping conditions.

6.4.4 Discussion

Assuming that formation of the P_xV_y defects will proceed via the diffusion of vacancy-containing defects, or the vacancy itself, and that the P_{Ge}^{+} donor atoms are isolated from one another, formation paths for the defects studied above can be discussed. PV formation should be rapid, enhanced by Coulomb attraction between the negatively charged vacancy and positively charged P_{Ge}^{+}. Diffusion of PV and P_2V will allow the growth of up to P_3V centres with Coulomb attraction between the component defects speeding the process. Diffusion of the P_3V centre, however, is not as easy to envisage, as, unlike the two smaller centres, the P_3V defect does

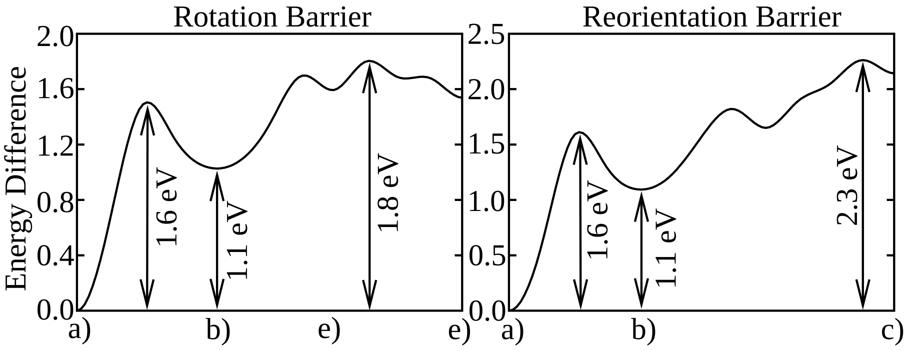

Figure 6.4: Diffusion barriers for the neutral P_2V defect, for both the reorientation and rotation paths. The labels indicate the configuration of the defect at that point along the path, and correspond with the structures shown in Fig 6.3. In the rotation path, the complex passes through two equivalent structures, both corresponding to structure e) in Fig 6.3, with the symmetry point for the diffusion process lying between these positions.

not lie on a single six-membered ring. It is therefore believed that the P_3V defect is immobile and thus formation of P_4V is unlikely.

All the P_xV_2 defects studied can be formed through the trapping of mobile PV or P_2V defects by other P_xV defects. This process is expected, however, to be impeded by Coulomb repulsion between the component acceptors. It is therefore expected that P_3V will be the most important compensating defect in germanium, with each defect removing four electrons from the conduction band. This is similar to results observed in highly *n*-doped silicon [52].

To estimate the temperature at which P_2V may be expected to anneal, we refer to Equation 6.1. If it is assumed that N, ν and Δt are the same for P_2V annealing in germanium and As_2V annealing in silicon, we come to the relationship

$$W_{\mathrm{Si}}/T_{\mathrm{Si}} = W_{\mathrm{Ge}}/T_{\mathrm{Ge}} \tag{6.2}$$

where subscripts indicate the material. Using the results presented above for As_2V diffusion in silicon, along with the annealing temperature of ~ 420°C[52], T_{Ge} is estimated to be around 290°C, about 100°C lower than T_{Si}. This value is in good agreement with DLTS results where an Sb_2V-related level has been suggested to anneal out at around 300°C[197].

The 100°C difference in annealing temperatures between germanium and silicon also appears in the carrier recovery at higher temperatures which occurs at $\sim$ 800°C in silicon, in the same temperature range as D_3V annealing [52], while in germanium, the carrier recovery appears to occur at $\sim$ 700°C[59]. This could suggest that D_3V annealing begins with D_2V diffusion away from the third D atom followed by the dissociation of D_2V.

6.5 Chapter Summary

In this chapter, the electrical properties and migration barriers for a number of vacancy-related defects in silicon and germanium were studied.

In silicon, the AsV, As_2V and AsBV defects were studied. It was found that the most stable forms of the AsBV defect were those with the B atom at a second or third neighbour site to the vacancy, in line with previous calculations on BV in silicon. The As_2V and AsBV defects were not found to exhibit donor levels, but all the defects did insert acceptor levels into the band gap.

The migration barriers calculated for AsV and As_2V were in line with previous modelling calculations on the defects, while the diffusion barriers calculated for As diffusion via formation of these defects lie in good agreement with experiment. Annealing temperatures estimated from the migration barriers were in good agreement with experiment for the AsV defect, but less so for the As_2V.

In germanium, a series of P_xV_y defects was studied. All of the studied defects except P_4V were found to possess at least one acceptor level within the band gap, and all were found to be stable with respect to isolated P_{Ge}^+ and V or smaller defects. PV and P_2V were found to be mobile, with the same paths as for AsV and As_2V defects in silicon. No similar migration path for P_3V could be seen, and combined with the Coulomb repulsion between the component defects required to form the

P_xV_2 defects, this suggests that P_3V will be the dominant compensating defect in germanium, as it has been observed to be in silicon.

Comparison between the migration barriers for P_2V in germanium and As_2V in silicon suggest a difference in annealing temperature of ∼100°C, in line with both experimental measurements of As_2V annealing and higher temperature recovery of active dopant concentration. The latter is attributed to D_2V migration being the first step in the removal of the D_3V defects in both materials.

Phosphorus diffusion in germanium will be studied more thoroughly in Chapter 7, using many of these techniques and some of these results.

Chapter 7

Dopant Diffusion in Germanium

7.1 Introduction

Dopant diffusion is an important process to understand in semiconductor research, due to the role it plays in shaping junctions in semiconductor devices. Ion-implantation is the technique most often used to achieve the small-area doping that modern devices require, but the atoms it introduces are often not at electrically active substitutional sites, and significant lattice damage accompanies any significant dopant concentration. Activating the dopants and removing this implantation damage requires thermal annealing which can also lead to diffusion of the dopant atoms away from their intended positions, and it is this diffusion which this section will concentrate on understanding.

Phosphorus and boron are important dopants in silicon and germanium, though their diffusion properties are radically different in the two materials. In germanium, boron is a very stable acceptor which readily moves to active substitutional sites and diffuses slowly, and p^+ doping of germanium is relatively simple to achieve. Phosphorus, on the other hand, diffuses readily under most annealing regimes, and achieving a high active concentration is difficult, as has been discussed in Section 6.4. In this Chapter, the diffusion of both these dopants will be examined, with the aim of understanding the mechanisms involved.

7.2 Modelling Method

Calculations were performed using 216 atom supercells and 501 atom clusters. Description of these systems and other calculation parameters can be found in Section 3.4.

Formation energies for neutral defects are calculated using the method described in Section 3.3.2 and migration barriers using the NEB method in Section 3.3.5. Electrical energy levels are calculated using either the marker or formation energy methods, as described in Section 3.3.4. Formation energies for charged defects were calculated either directly from charged supercell calculations as in Section 3.3.2 or using marker method-calculated energy levels and the formation energies calculated for neutral defects. Binding energies were calculated by both methods given in Section 3.3.3.

The experimentally known donor level of substitutional Se at $E_\text{c} - 0.28$ eV [198] and acceptor level of the VO complex at $E_\text{v} + 0.32$ eV [169] are used as markers for the boron interstitial defects, while the SbV donor level at $\text{E}_\text{v} + 0.09$ and acceptor levels at $\text{E}_\text{v} + 0.31$ and $\text{E}_\text{c} - 0.30$ [50, 131] were used for the phosphorus vacancy and boron vacancy defects. Both of these defect sets were used for the phosphorus interstitial defects.

Three mechanisms for dopant diffusion were investigated in these sections.

In vacancy-mediated diffusion, the dopants form complexes with the lattice vacancy while remaining in a substitutional position themselves. Diffusion then proceeds as motion of the vacancy enables net motion of the dopant atom. This mechanism has been discussed already in Sections 6.3.4 and 6.4.3.

In interstitial-mediated diffusion, the dopant atoms are considered to either be ‘kicked out’ into interstitial sites (P_i or B_i) or to remain in substitutional positions and form complexes with self interstitials (PI or BI). The diffusion then proceeds either by motion of the P_i or B_i defects along the open channels of the crystal, or by motion of the PI or BI defect as a whole.

The third mechanism, correlated exchange (CE) has been proposed previously by Pandey for self and dopant diffusion in silicon [199]. This method involves diffusion without interaction with any other defects, and proceeds through the rotation of the two adjacent atoms about their mutual bond-centre.

7.3 Phosphorus Diffusion

Diffusion of phosphorus via the three methods outlined above has been studied in this work and will be reported below. It has long been believed that the fast diffusion of phosphorus in germanium is due to a vacancy-mediated mechanism, and this work will confirm this view and add a degree of additional detail to the atomistic understanding of all the mechanisms. Results found using neutral supercell-calculated formation energies and marker-method-calculated energy levels are also compared here with results found using the formation energy method to calculate energy levels.

There have been various experimental works previously published on phosphorus diffusion in germanium. Tailing and out-diffusion of phosphorus implants have been observed [74], and studies of diffusion profiles have been used to determine the diffusion barrier for phosphorus in germanium. Measurements performed on the depth of the *p*-*n* junction formed through phosphorus diffusion have yielded a diffusion barrier of ∼2.5 eV [67]. Later work using spreading resistance probe techniques and secondary ion mass spectroscopy (SIMS) yielded a barrier of 2.07 eV [57], while other SIMS studies report diffusion barriers of 2.3 or 2.85 eV with a doubly or singly negative diffusing species, respectively [72, 200]. Reference [72] also suggests possible evidence for transient enhanced diffusion (TED) effects. The PV defect, termed the E-centre, has also been studied experimentally. The defect is observed to possess two acceptor levels, at $\mathrm{E_v} + 0.35$ and $\mathrm{E_c} - 0.23$ eV and anneals out between 100 and 150°C[50]. Previous supercell-based theoretical work has calculated the binding energy of the related AsV defect as 0.6 eV in germanium [201]. This seems too low in comparison with the E-centre in silicon which anneals out at similar temperatures - around 150°C for AsV and 125°C for PV [52], and is calculated to possess binding energies for AsV of 1.09 [202], 1.21 [203] or 1.34 eV [201] according to a number of previous studies. Diffusion via the PV defect has been studied with theoretical methods in the neutral charge state, and is found to have a barrier of 2.98 eV [204]. The $\mathrm{P_i}$ and PI defects have not been so well studied in germanium.

The diffusion of phosphorus in silicon has also been studied previously by *ab initio* and experimental methods. One theoretical study [205] on neutral defects found the most stable structure to be one where the P atom lies at an interstitial site between the bond centre and the centre of a hexagonal ring, dubbed the X_2 configuration. This structure was found to have a formation energy of 2.7 eV and a migration barrier of 0.2 eV through motion around the hexagonal ring alongside reorientations between them, although these energies are calculated with respect to the neutral rather than positive substitutional P atom and thus no Fermi level dependence is discussed. A second study [63], which included singly charged defects, found larger energies of 3.5 eV $- \mu_e$ for formation and 0.6 eV for migration in the neutral charge state via a very similar path, with respect to singly positively charged substitutional P, where μ_e is the Fermi energy as measured from the valence band top. In the positive charge state, the $\langle 100 \rangle$ split interstitial - dubbed the S interstitial - and Hexagonal- (H-) site interstitial were found to be degenerate with formation energies of 3.1 eV and with a migration barrier of 0.3 eV by motion between the H-site and S interstitials. In the negative charge state, the structure and path were found to be as in the neutral case, but the energies rose to $4.1 - 2\mu_e$ eV for formation and 1.4 eV for migration, and so this charge state was considered unimportant for the diffusion of the defects. The latter study is in excellent agreement with experimental studies giving 3.68 and 3.43 eV diffusion barriers for the $\mathrm{P_i^0}$ and $\mathrm{P_i^+}$ defects respectively [75].

Most of the following work on phosphorus diffusion has been published in Physical Review B [206].

7.3.1 Vacancy Mediated Diffusion

The mechanisms for vacancy-mediated diffusion as well as many of the pertinent calculations have already been presented in the discussion of P_xV migration in Section 6.4. In this Section, the work presented there will be extended to describe the diffusion of phosphorus via the formation of these defects. The diffusion process is considered to commence with the formation of the P_xV defect and then proceed as the defect migrates. To discuss this process, we therefore begin by investigating the P_xV defects before the migration calculations presented previously are included. In addition, we present in this Section formation energies calculated directly from charged supercells and energy levels calculated from these, for comparison with the marker method calculations presented earlier.

Formation energies relative to P_{Ge}^+ and energy levels of the PV complex calculated via both methods are reported in Table 7.1. The binding energy between the P_{Ge}^+ and $V^=$ in the PV^- defect is calculated to be 0.6 eV by the supercell method. Using the singly negatively charged cluster, the total energy rises by 0.33, 0.64 and 0.82 eV with respect to the bound defect as the component defects are moved to the second, third and fourth neighbour positions respectively. Thus the binding energy is calculated in the cluster to be at least 0.82 eV. It can also be seen that the energy levels calculated by relying on formation energies found in charged supercells and those calculated by relying on energy levels found in the cluster using the marker method are not in agreement. Using the experimental germanium band gap of 0.66 eV, the marker method results for energy levels, calculated using clusters, are in good agreement with experimental values of $E_v + 0.35$ and $E_c - 0.23$ eV [50] for the first and second acceptor levels of the PV defect, while the formation energy method results, calculated in supercells, are not in agreement. In addition, it should be noted that while the first acceptor level is calculated to lie above the second in the marker method, the energy difference between the two is too small to say that it contradicts the experimental data.

The same calculations were performed for the P_2V defect, and the results are detailed in Table 7.2. As with the PV defect, there is significant difference between the results

Table 7.1: Formation energies relative to P_{Ge}^{+} (E_f) and energy levels ($E(n-1/n)$) in eV of the PV defect as calculated using neutral PV supercells and charged cluster calculations (cluster) or from the formation energies calculated for charged defects in the supercell (supercell).

	E_f			$E(n-1/n)$	
Charge	supercell	cluster	Level	supercell	cluster
$+$	2.16	2.10	$(=/-)$	$E_v + 0.23$	$E_v + 0.38$
0	$2.23 - \mu_e$	$2.23 - \mu_e$	$(-/0)$	$E_v + 0.08$	$E_v + 0.43$
$-$	$2.31 - 2\mu_e$	$2.66 - 2\mu_e$	$(0/+)$	$E_v + 0.07$	$E_v + 0.13$
$=$	$2.54 - 3\mu_e$	$3.04 - 3\mu_e$			

Table 7.2: Formation energies relative to P_{Ge}^{+} (E_f) and energy levels ($E(n-1/n)$) in eV of the P_2V defect as calculated from neutral P_2V formation and the cluster-based marker method (cluster) or from the formation energies calculated for charged defects in the supercell (supercell).

	E_f			$E(n-1/n)$	
Charge	supercell	cluster	Level	supercell	cluster
$+$	$1.79 + \mu_e$	$2.04 + \mu_e$	$(=/-)$	$E_v + 0.19$	$E_v + 0.57$
0	1.78	1.78	$(-/0)$	$E_v + 0.20$	$E_v + 0.50$
$-$	$1.98 - \mu_e$	$2.28 - \mu_e$	$(0/+)$	$E_v - 0.01$	$E_v - 0.26$
$=$	$2.17 - 2\mu_e$	$2.74 - 2\mu_e$			

of the two methods. From both calculations, the P_2V defect exhibits no donor level, instead displaying two acceptor levels which show a slight negative-U behaviour, but again as with PV, the difference between the levels is too small to be certain of that assignment.

The migration paths considered and barriers calculated in Section 6.4.3 are used here again. Combining them with the formation energies of the PV defects as given in Table 7.1 yield total diffusion barriers reported in Table 7.4. These vary with the position of the Fermi level and for a mid-gap value for μ_e, the diffusion barrier is found to lie between 2.7 and 3.5 eV for PV, and 2.7 to 3.3 eV for P_2V with the barrier decreasing in more heavily doped material.

7.3.2 Interstitial Mediated Diffusion

7.3.2.1 Phosphorus-Interstitial Structures

The phosphorus-interstitial pair was studied, in configurations described as a substitutional P atom along with a T-site and H-site Ge self interstitial ($\mathrm{PI}_{T,H}$); T- and H-sited P interstitials ($\mathrm{P}_{\mathrm{i}T,H}$) and $\langle 110\rangle$ and $\langle 100\rangle$ split interstitials. From all these initial structures,the neutral defect relaxed without barrier to a structure with the P atom lying between a hexagonal and bond-centred site, labelled $\mathrm{P}_{\mathrm{i}X_2}$. This structure was also the most stable in the singly negative charge state, while in the singly positive, the distorted bond-centre relaxes to a $\langle 100\rangle$ split interstitial with the P atom distorted towards an adjacent H site ($\mathrm{P}_{\mathrm{i}S}$). In the positive state, the $\mathrm{P}_{\mathrm{i}S}$ structure is degenerate with the $\mathrm{P}_{\mathrm{i}H}$ within the limits of the calculations. The stable structures are shown in Fig 7.1 and their formation energies with respect to $\mathrm{P}_{\mathrm{Ge}}^{+}$ and energy levels are given in Table 7.3.

The nearest neighbour distances between P and adjacent Ge atoms are 2.44 Å(101% of the $\mathrm{P}_{\mathrm{Ge}}^{+}$-Ge distance) for the $\mathrm{P}_{\mathrm{i}H}^{+}$, 2.21 Å(91%) for the $\mathrm{P}_{\mathrm{i}X_2}^{0}$ and 2.20 Å(91%) for the $\mathrm{P}_{\mathrm{i}X_2}^{-}$ defects. In the $\mathrm{P}_{\mathrm{i}S}^{+}$ defect, there is a separation of 2.18Å(90%) between the P atom and the Ge that forms the other half of the split interstitial, 2.32Å(96%) for the other two neighbours of the P atom, and 2.36Å(97% of the bulk Ge-Ge separation) between the split-interstitial Ge and its neighbouring Ge atoms. All of these structures are very similar to those previously published for silicon [63]. The binding energy for the dissociation of the $\mathrm{P}_{\mathrm{i}}^{+}$ defect into $\mathrm{P}_{\mathrm{Ge}}^{+}$ and a neutral $\langle 110\rangle$ Ge self interstitial was calculated within the supercell to be 0.7 eV. In a positively charged cluster, the total energy rose to 0.34, 0.54, 0.58, 0.70 then 0.77 eV above that of the stable bound defect as the component defects were moved from first through fifth nearest neighbour positions. The energy levels exhibit a normal level ordering within the band gap when calculated with the marker method and a possible negative-U behaviour with the formation energy method. Using different markers leads to differences in the level positions of 0.2-0.3 eV. There are no known experimental results to compare with for the PI defect, and so it is not possible to determine which set

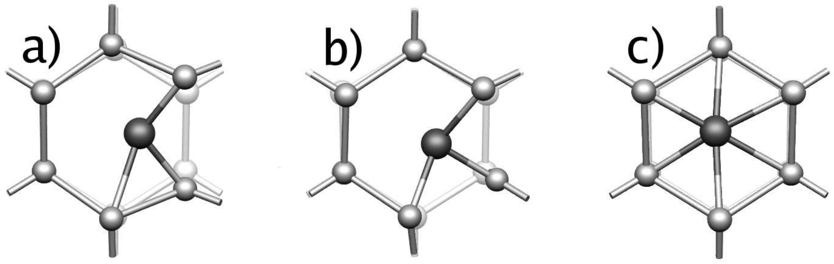

Figure 7.1: Structures of the phosphorus interstitial complex, as viewed along a ⟨111⟩ direction. The smaller, lighter grey balls represent Ge atoms, and the larger, darker grey ball represents the P. Each structure has been superimposed on a lighter grey image of perfect Ge, as an aid to the reader. a) The distorted bond centre structure $\mathrm{P}_{\mathrm{i}X_2}$. b) The distorted ⟨100⟩ split interstitial $\mathrm{P}_{\mathrm{i}S}$. c) The H-site phosphorus interstitial $\mathrm{P}_{\mathrm{i}H}$.

Table 7.3: Formation energies relative to $\mathrm{P}_{\mathrm{Ge}}^{+}$ ($\mathrm{E_f}$) and energy levels ($\mathrm{E}(n-1/n)$) in eV of the PI defect as calculated using neutral PI supercells and charged cluster calculations with different sets of markers (cluster Se/VO or SbV) or from the formation energies calculated for charged defects in the supercell (supercell).

	$\mathrm{E_f}$				$\mathrm{E}(n-1/n)$		
Charge	supercell	cluster		Level	supercell	cluster	
		Se/VO	SbV			Se/VO	SbV
$+$	2.88	3.12	2.90	$(-/0)$	$\mathrm{E_v}+0.28$	$\mathrm{E_v}+0.39$	$\mathrm{E_v}+0.68$
0	$3.27-\mu_e$	$3.27-\mu_e$	$3.27-\mu_e$	$(0/+)$	$\mathrm{E_v}+0.39$	$\mathrm{E_v}+0.15$	$\mathrm{E_v}+0.37$
$-$	$3.55-2\mu_e$	$3.66-2\mu_e$	$3.95-2\mu_e$				

of marker defects are more accurate. It will be seen, however, that the difference in energy calculated here has little effect on the diffusion properties of phosphorus.

7.3.2.2 Phosphorus-Interstitial Migration Barriers

In the neutral and singly-negative charge states, phosphorus migration was considered to take place by a combination of three movements relating to the six-membered ring on which the defect is considered to lie: a movement of the P across the H-site to the Ge-Ge bond opposite its original location (Trans-H), a movement of the P

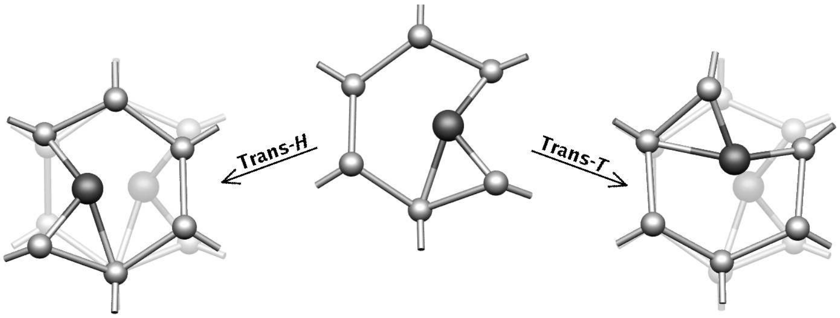

Figure 7.2: Migration steps for the $\mathrm{P}_{\mathrm{i}X_2}$ structure of the phosphorus interstitial. The smaller, light grey balls represent Ge atoms, and the larger, dark grey ball represents P. The central structure is a starting point, repeated behind the other two as an aid to the reader. To the left is the Trans-H migration step, whereby the P atom moves across the adjacent H-site, and to the right is the Trans-S step, where the P moves around the six-membered ring.

atom around the six-membered ring from one Ge-Ge bond to the next (Trans-S) and a rotation about the Ge-Ge bond the phosphorous atom interrupts to a different six-membered ring (Rot). The Trans-H and Trans-S steps are shown in Fig 7.2. In the positive charge state, the migration was considered to take place via exchange between the H-site and split interstitial structure along with migration of the phosphorous along $\langle 110\rangle$ channels linking H sites. Therefore, migration steps between H sites (HH), between the Pi_S structure and the adjacent H site (Short-SH) and an H site one step removed from the initial position (Long-SH) as well as the rotation of the $\mathrm{P}_{\mathrm{i}S}$ structure into a different $\langle 100\rangle$ direction (Rot) were considered.

In the singly negative charge state, the Rot step was calculated to have a small barrier of around 0.08 eV, with a saddle point at a bond-centre structure distorted towards an adjacent tetragonal interstitial site ($\mathrm{P}_{\mathrm{i}BC-T}$). The Trans-$S$ step was then found to exhibit the lowest barrier of the translation steps, with a saddle point of the $\mathrm{P}_{\mathrm{i}S}$ structure and a barrier of 0.80 eV. In the neutral charge state, the same path is followed, but the barrier for Rot is a little more complex, and the Trans-S barrier drops to 0.34 eV. In the singly positive charge state, the Short-SH barrier is calculated to be 0.04 eV, the Long-SH barrier 0.84 eV, the HH barrier 0.76 eV,

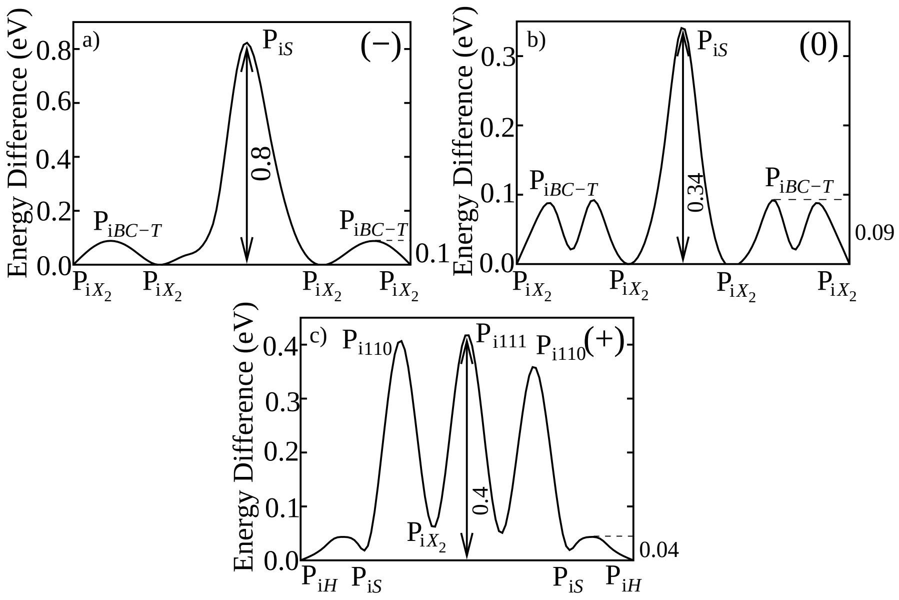

Figure 7.3: Migration barriers for the P$_\mathrm{i}$ defect in various charge states, relative to the most stable P$_\mathrm{i}$ structure for that charge state. a,b) singly negative and neutral charge states, showing the Trans-S migration step preceded and followed by a Rot step. c) singly positive charge state migration, with the Short-SH step preceding and following the Rot step. In this case, the Rot migration step consists of a series of three peaks as the defect moves through several different high-symmetry configurations during its motion.

and the Rot barrier 0.42 eV. This suggests a migration path where the P$_{\mathrm{i}S}$ defect rotates with a saddle-point of a split interstitial in the $\langle 111\rangle$ direction (P$_{\mathrm{i}111}$), and two lower barriers with $\langle 110\rangle$ split interstitial (P$_{\mathrm{i}110}$) structures. The P atom then migrates across the adjacent hexagonal ring via the H-site and rotates again. The barriers for all these paths are detailed in Fig 7.3.

Combining these barriers with the formation energies for the P$_\mathrm{i}$ defect as calculated above, we find total diffusion barriers as reported in Table 7.4. Again, the barrier depends on the position of μ_e, and lies between 3.3 and 4.2 eV for a mid-gap Fermi level.

Table 7.4: Total migration energies in eV for the PV and PI defects as calculated through the supercell based formation energy (supercell) and cluster based marker (cluster) methods.

	PV			P$_2$V	
Charge	supercell	cluster	Charge	supercell	cluster
0	$3.8 - \mu_e$	$3.8 - \mu_e$	0	$3.6 - 2\mu_e$	$3.6 - 2\mu_e$
$-$	$3.6 - 2\mu_e$	$4.0 - 2\mu_e$	$-$	$3.7 - 3\mu_e$	$4.0 - 3\mu_e$
$=$	$3.6 - 3\mu_e$	$4.0 - 3\mu_e$	$=$	$3.9 - 4\mu_e$	$4.5 - 4\mu_e$

	PI		
Charge	supercell	cluster	
		Se/VO	SbV
$+$	3.3	3.5	3.3
0	$3.6 - \mu_e$	$3.6 - \mu_e$	$3.6 - \mu_e$
$-$	$4.4 - 2\mu_e$	$4.5 - 2\mu_e$	$4.8 - 2\mu_e$

7.3.3 Correlated Exchange (CE)

The CE migration path was found to be essentially the same as that proposed by Pandey for self-diffusion in silicon [199]. The barrier for this process was calculated in the singly positive charge state, as this is the state that the substitutional P is expected to possess, and is found to be 6.2 eV.

7.3.4 Discussion

The CE mechanism is observed to have a very high diffusion barrier of 6.2 eV, strongly suggesting that it is not an important process in the diffusion of phosphorus in germanium.

The PV defect was examined in charge states ranging from the neutral to the doubly negative. Calculated electrical levels, given in Table 7.1 combined with experimental values of $E_v + 0.35$ and $E_c - 0.23$ eV [50] for the acceptor levels suggest that the cluster-based marker method is the most reliable method, providing further support for the decision to rely on clusters. The binding energy between positively charged P_{Ge}^{+} and the double negative $V^{=}$ to form the singly negative PV^{-} defect was calculated in the supercell to be 0.6 eV. This agrees with previous theoretical work using similar methods [201], but is not congruent with work in silicon. Similar annealing temperatures have been measured experimentally for annealing of the PV defect in the two materials [52] but significantly higher binding energies of 1.1-1.3 eV have been calculated in silicon [201, 202, 203]. Cluster calculations of the binding energy between P and V in germanium show a moderate increase in the energy to 0.82 eV when the component defects are separated to the fourth neighbour positions. This result is not converged with defect separation, but limited by the size of the cluster and may be expected to converge to a value close to the results for silicon if sufficiently large clusters could be used. P_2V was not studied in such detail, but migration barriers for the defect were seen to vary little with charge state, leaving the formation energy to determine the relationship between the diffusion energies via P_2V formation.

The phosphorus-interstitial structures found here are very close to those calculated previously in silicon [63]. The energy levels were found to depend on the method used to calculate them. The cluster-calculations give a donor level at $E_v + 0.15$ or 0.37 eV and an acceptor level at $E_v + 0.39$ or 0.68 eV depending on the marker used. The errors in the method are worse in this case than normal. We do not have experimental results to compare these with. The binding energy between the neutral $\langle 110 \rangle$ Ge self-interstitial and P_{Ge}^+ to form the stable form of Pi^+ was calculated in the supercell to be 0.7 eV, and 0.77 eV in the cluster calculation, when the component defects were moved to fifth neighbour positions. In contrast with the vacancy case, the cluster-calculated value is quite close to the supercell value, and seems that it may be nearly converged by this distance, but cluster size restrictions prevent further tests.

The total barriers obtained depend on the method used to calculate the formation energies of the defects. Fig 7.4 compares the barriers obtained from formation energies as calculated from charged supercells with those calculated using neutral phosphorus defects and marker method calculated energy levels with Se/VO used as a marker for the interstitial defects. Using the SbV marker for the interstitial defects lowers the total energy for PI^+ migration, such that it is the most favourable diffusion path up to $\mu_e = 0.15$ eV. This is the only difference to the diffusion paths,

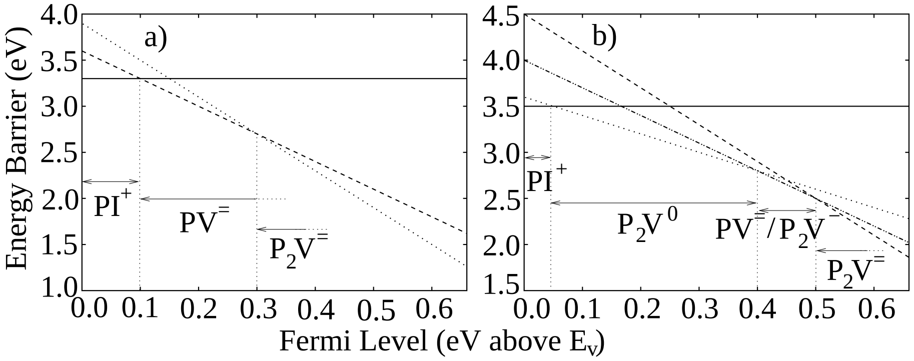

Figure 7.4: Diffusion barrier dependence on Fermi level position for phosphorus complexes as calculated from a) charged supercell formation energies and b) neutral supercell formation energies and marker method calculated energy levels with Se and VO as markers for the interstitial defects. Energies are given relative to singly positively charged substitutional P. Only the barriers which are most favourable for some Fermi level positions are displayed. Arrows and labels on the graphs indicate the most favourable defect in the indicated regions.

and since P-doped material is unlikely to be *p*-type, it does not make a significant difference to the diffusion of P.

These results suggest that phosphorus diffuses via a vacancy-mediated mechanism for almost all values of the Fermi Energy. For $\mu_e \lesssim \mathrm{E_v} + 0.4$ eV, the most favourable diffusing species is the neutrally charged P_2V complex, then for μ_e between 0.4 and 0.5 eV, diffusion would occur either via the formation of singly negative P_2V or doubly negative PV defects. Above 0.5 eV, the doubly negative P_2V will dominate. It is also possible that, for Fermi levels below 0.4 eV, the doubly negative $PV^=$ defect would be dominant in phosphorus diffusion, as the lower concentration makes P_2V formation less likely.

In *n*-type material, these results would support experimental studies reporting a doubly negative diffusing species, either PV or P_2V [72]. For a μ_e of around 0.5 eV, a diffusion barrier of ~ 2.5 eV is calculated, in good agreement with previous experimental data [67, 57, 72]. Comparing our results with those suggesting singly negative PV as the diffusing species and a diffusion barrier of 2.85 eV [200], this barrier is in good agreement with our results for diffusion via P_2V^0 with a μ_e of around 0.4 eV, which would exhibit the same dependence on carrier concentration. The results are also in good agreement with parallel non-AIMPro theoretical work using only uncharged supercells [204], and suggest that phosphorus diffusion could be enhanced by supersaturation of either interstitials or vacancies, supporting the idea that phosphorus might experience TED effects [72].

7.4 Boron Diffusion

As presented above for phosphorus diffusion, the diffusion of boron is studied in detail via the same three methods. In the case of boron, it is believed that the diffusion in germanium occurs via an interstitial-mediated mechanism, explaining the low diffusivity. This will again be confirmed by the work presented below.

Diffusion of boron in germanium is seen to be very slow experimentally [58, 68], and unlike in silicon, transient enhanced diffusion (TED) is very weak and has only recently been observed [207]. Diffusion barriers of 4.5 to 4.65 eV have been measured experimentally, but these are accompanied by unusually large pre-factors ranging from 6×10^8 down to 1.97×10^5 cm^{2}s^{-1} [58, 66, 67]. In silicon, boron diffusion is seen to progress with a barrier of $\sim$3.5 eV [75], with pre-factors close to $\sim$0.9 cm^{2}s^{-1}. In both silicon and germanium, boron diffusion is expected to proceed via an interstitial mechanism [58, 208, 209], and the differences in the diffusion behaviour are believed to stem from the differences in the behaviour of the self-interstitial in the two materials.

Theoretical studies of boron in silicon have produced a number of possible diffusion paths, most of which are in good agreement with the experimentally obtained barriers. One study [70] finds a diffusion path proceeding from the positive boron interstitial (BI$^+$) complex whose formation energy is about 3.2 eV. This on changing its charge state to neutral then migrates via the H-site without true kick-out, and with a barrier of 0.6 eV, leading to a total diffusion barrier of 3.8 eV. Another study [61] proposed different charge-state-dependent paths with energy barriers of 2.9 eV+μ_e in the neutral and 3.4 eV in the negative charge states. A third investigation [71] found a formation energy of 1.8 eV+$2\mu_e$ for BI^+ relative to the charged substitutional defect, and a kick-out migration path with a total barrier of 1.2 eV giving a net diffusion barrier of 3.0 eV+$2\mu_e$. Taking μ_e to be at mid-gap $\sim$ 0.6 eV yields a diffusion barrier of 4.2 eV.

There has also been previous modelling work carried out on boron diffusion in germanium [69]. The calculated formation energy of BI^+ was found to be 2.77 eV+$2\mu_e$, relative to B^-_{Ge} and the defect was found to migrate with a barrier of 0.9 eV via bond centres, followed by a subsequent reorientation with a barrier of 0.5 eV. The diffusion barrier is then 3.7 eV+$2\mu_e$, which if $\mu_e \sim 0.35$ eV gives a barrier of 4.4 eV. The authors quote a barrier of 4.5 eV although their reasoning is unclear. Somewhat similar barriers are found for other charge states. However, this work does not account for the large prefactors found experimentally, and so the agreement with the experimental barrier does not answer all the questions around the diffusion. The question of the high prefactors will be discussed later in this Chapter.

Most of this work has been published in Physical Review B [210].

7.4.1 Interstitial Mediated Diffusion

7.4.1.1 Boron-Interstitial Structures

Calculations were performed within the cluster method to establish the most stable configuration for the BI complex in germanium. As with PI above, several structures were studied: substitutional boron with T- and H-sited Ge self-interstitials, T- and H-sited boron interstitials, and $\langle 110 \rangle$ and $\langle 100 \rangle$ split interstitials (BI_{110} and BI_{100}). The calculations gave the BI_{110} defect as the most energetically favourable in the neutral and singly negative charge states, while the singly positive charge state exhibited a structure with a substitutional boron atom and an adjacent tetrahedral Ge interstitial (BI_T). The defect structures are in agreement with previous work [69] and are also very similar to those found for BI complexes in silicon [211]. The formation energy of BI^0 relative to B^-_{Ge} is calculated to be 3.2 eV + μ_e.

Table 7.5: Energy change, in eV, upon separation of the BI^- defect along a $\langle 110 \rangle$ chain. The last column indicates the component moved with respect to the previous separation.

Separation (Steps)	Energy (eV)	Component Moved
0	0.00	-
1	0.27	I
2	0.54	B
3	0.54	B
4	0.66	I
5	0.67	B

The binding energy for the singly negative defect was calculated by separating the defect within the cluster. Table 7.5 gives the difference in energy of the cluster as the component B_{Ge} and I defects are moved apart, along with an index showing which component defect was moved to increase the separation each step. The lack of increase when moving the B atom beyond the two-step separation suggests that the defect is separated at this stage, and that the increase on moving the I defect is due to interaction with the surface of the cluster, rather than a bulk effect. Therefore, a binding energy of 0.54 eV for the BI^- defect is calculated.

Energy levels were calculated using the marker method and charged clusters as described. The BI donor level is found to lie at $E_c - 0.10$ eV and the acceptor level at $E_v + 0.29$ eV. This implies that the structural changes indicated above give rise to a negative-U [14] system in which the neutral charge state is not stable for any Fermi Energy position, similar to BI in silicon [212]. Using the experimental band gap of 0.66 eV, the $(-/+)$ transition is found to lie at $E_v + 0.43$ eV.

Using these energy levels, formation energies of 2.6 eV + $2\mu_e$ and 3.5 eV were calculated for the singly positive and singly negative charge states, respectively.

7.4.1.2 Boron-Interstitial Migration Barriers

For the BI_{110} structure, the B atom is considered to migrate by the same mechanism as the I_{110} defect described in Section 5.5. The B atom moves along the $\langle 110 \rangle$ chains

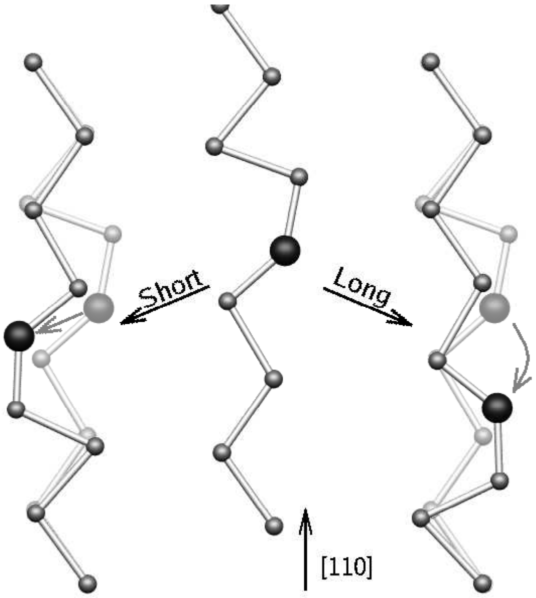

Figure 7.5: Diagram showing the mechanisms involved in the migration of singly negative BI_{110}. The smaller, light grey balls represent Ge atoms and the larger, black balls B. In the centre is the initial configuration, showing the distorted ⟨110⟩ chain containing the split interstitial. The faded chains on each side are the central image repeated as a guide to the reader. To the left is shown the 'short' migration step, where the B atom moves from one Ge to the next along the chain. To the right is shown the 'long' migration step, where the B atom skips a Ge atom, and forms a split interstitial with the next atom along.

in the crystal, and rotates between different chains. Migration along the chain occurs by steps of one or two atoms, termed 'short' and 'long' steps respectively, where the B atom forms a new split-interstitial structure with the atom to which it moves. This path is depicted in Figure 7.5. The BI_T structure migrates by movement of the B atom to an adjacent crystal site. The interstitial atom drops into the substitutional site just vacated, and the Ge atom at the site to which the B atom is moving is displaced to a T-site. This path is depicted in Figure 7.6. Kick-out mechanisms were also calculated, wherein the B atom jumps into and migrates along the ⟨110⟩ channels in the crystal.

For BI_{110}^{-}, the migration of the defect as a complex is calculated to have barriers of 0.78 eV for the long, 1.50 eV for the short and 0.31 eV for the rotation steps.

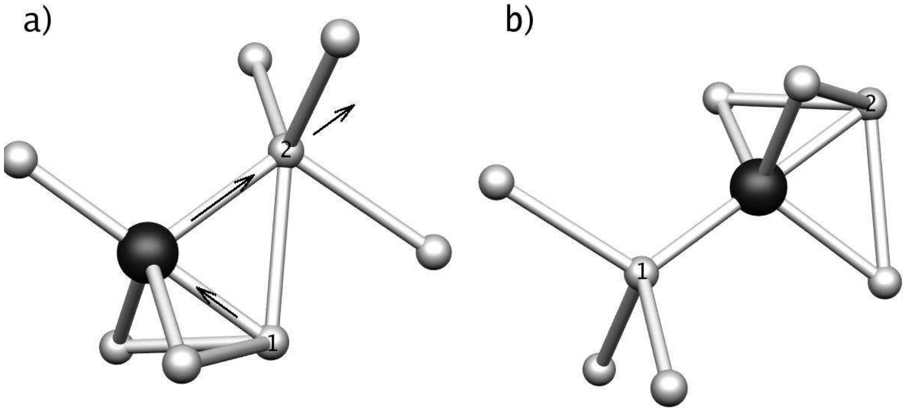

Figure 7.6: Diagram showing the proposed mechanism for migration of BI_T. The light grey balls represent Ge atoms while the large black ball represents the B atom. The arrows indicate the direction of atomic movements, and the numbered Ge atoms are used to clarify the atomic movement. Interstitial Ge atoms are at T-sites, with three of the surrounding atoms shown.

The migration would therefore proceed through long and rotation steps only, with a saddle point along the $\langle 110\rangle$ chain lying at bond-centre sites distorted towards an adjacent tetragonal site (B_{BC-T}). The kick-out path is a little more complicated. The defect first reorients with a barrier of 0.31 eV to a dumbbell lying in a $\langle 110\rangle$ direction perpendicular to the chains (B^*_{110}), lying 0.1 eV above the more stable B_{110} defect. Diffusion can then proceed to an adjacent B^*_{110} position via a metastable B_H defect. The migration barrier for the kick-out mechanism was found to be 0.68 eV, similar to the barrier for migration without kick-out.

In the neutral charge state, the migration as a complex is calculated to have barriers of 0.76 eV for the long, 0.63 eV for the short and 0.16 eV for the rotation steps. It would therefore proceed via the short and rotation steps with a barrier of 0.63 eV and a saddle point structure of a bond-centre boron interstitial (B_{BC}). The kick out path proceeds with first a reorientation to a B^*_{110} structure via a structure with a substitutional B atom adjacent to a $\langle 111\rangle$ self-interstitial structure ($\mathrm{B}_{\mathrm{Ge}}\mathrm{I}_{111}$). From the B^*_{110} structure, the B is kicked out into the interstitial channels, where it migrates between H-site configuration (B_H) saddle points and interstitial minima at a site

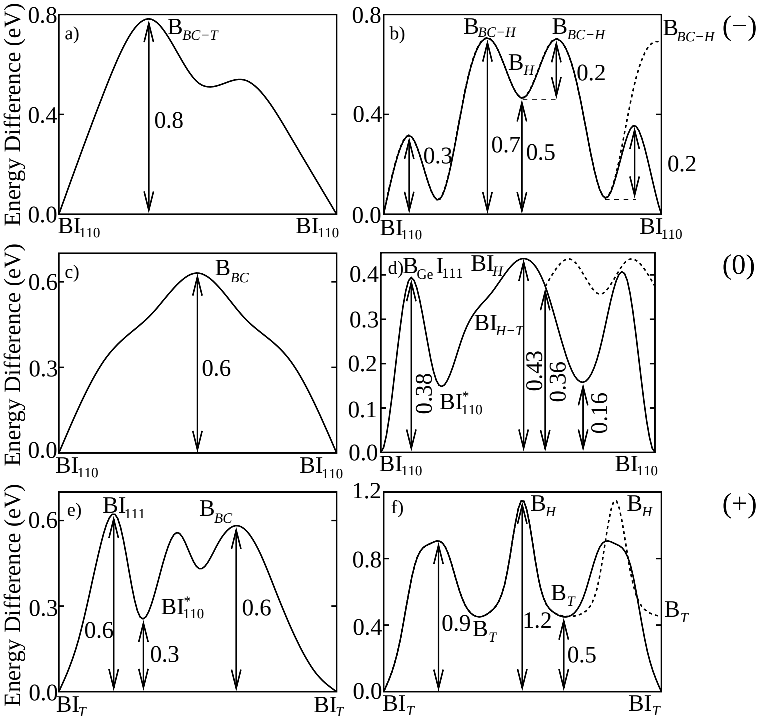

Figure 7.7: Diagrams showing the structure of the barriers for BI complex migration in three charge states. a),b) Diffusion in the negative charge state as a complex and via B kick-out, respectively. c),d) Diffusion in the neutral charge state as a complex and via B kick-out. e) f) Diffusion in the singly positive charge state as a complex and via B kick-out.

between the H and the T site (B$_{H-T}$). No barrier is observed for kick-in from the B$_{H-T}$ to B$^*_{110}$, and the total migration barrier is calculated to be 0.43 eV.

In the positive charge state, the migration proceeds as shown in Figure 7.6, with a barrier of 0.60 eV. The saddle point for this path is a split interstitial in the $\langle 111 \rangle$ direction, after which the defect relaxes into a B$^*_{110}$ structure, 0.28 eV above the stable BI$_T$ structure. The migration continues with the defect passing through a B$_{BC}$ structure before arriving at the final BI$_T$ position. For the kick-out mechanism, the barrier to kick-out is calculated to be 0.89 eV, with the B atom moving to a tetrahedral interstitial position (B$_T$) 0.45 eV above the BI$_T$ structure. It then faces a 0.70 eV barrier for further migration through the B$_H$ site, or a 0.44 eV barrier to return to a BI$_T$ position. This gives a total barrier for kick-out migration of 1.15 eV above the BI$_T$ structure.

The barriers for all the charge states are illustrated in Figure 7.7. All these results, both the paths and the calculated barriers lie close to equivalent calculations previously performed for boron in silicon [61, 71]. When compared with the earlier non-AIMPro theoretical work in germanium, the barriers calculated here are lower in all cases, but the paths taken are the same [69].

Total energy barriers for the diffusion of boron through an interstitial-mediated mechanism can be calculated by summing the migration barriers presented here with the formation energies presented in Section 7.4.1.1. These results are given in Table 7.7. For a μ_e of around mid gap, as expected in the high temperature experiments, the diffusion barriers become 3.8, 3.9 and 4.2 eV for the singly positive, neutral and singly negative charge states respectively.

7.4.2 Vacancy Mediated Diffusion

Vacancy mediated diffusion is the method associated with most fast-diffusing impurities and self-diffusion in germanium. Using the marker method with SbV as a marker, the $(-/0)$ level of the BV defect is calculated to lie at $\mathrm{E_v} - 1.29$ eV. The position of this level below the valence band is a matter of some suspicion, but as with the PI defect, it will be seen that this does not have an effect on the migration barrier for any Fermi level position.

The formation energy of the neutral BV defect as calculated in the supercell is found to be 3.0 eV$+\mu_e$ relative to the negatively charged $\mathrm{B}_{\mathrm{Ge}}^-$. From the energy level above, the formation energy for the negative defect is calculated to be 1.7 eV. The binding energy for the defect is calculated in a negatively charged cluster using the same method as for the BI defect above. The results are given in Table 7.6. As can be seen, the BV^- defect is not bound. This would therefore suggest a formation energy for BV^- of around the V^0 formation energy, 2.5 eV from Section 5.4. Therefore, the formation energy calculated form the energy level method is taken to be a lower bound for the energy of the BV^- defect.

Table 7.6: Energy change, in eV, upon separation of the BV^- defect along a $\langle 110 \rangle$ chain. The last column indicates the component moved with respect to the previous separation.

Separation (Steps)	Energy (eV)	Component Moved
1	0.00	-
2	0.02	V
3	0.14	B
4	0.08	V
5	0.07	B

The path considered for BV migration is the same as for PV migration discussed in Section 6.4.3. Calculations were performed in the singly negative and neutral charge states. These give an exchange barrier for the B atom to cross the vacancy of 2.6 eV in the negative charge state, and 2.8 eV in the neutral state. When combined with the formation energy of the BV complex, this gives a total diffusion barrier for boron by the vacancy mediated path of >4.3 eV for the negative and 5.8 eV+μ_e in the neutral charge states. These values are found in Table 7.7.

These energies imply that vacancy related mechanisms are unlikely to compete with the interstitial-mediated diffusion mechanism.

7.4.3 Correlated Exchange

The migration path for CE diffusion of boron was found to be essentially the same as found for phosphorus. The barrier was calculated for the negatively charged system, as the B dopants are expected to be in this charge state for the temperatures at which diffusion takes place, and was found to be 4.1 eV.

7.4.4 Discussion

Vacancy mediated diffusion of boron in germanium is found in these calculations to possess a high energy barrier, 5.8 eV + μ_e in the neutral charge state. This suggests that this path is not important for boron in germanium, in contrast to

Table 7.7: Total diffusion energies in eV for the BV, BI and boron CE mechanisms

BV		BI		CE	
Charge	Energy	Charge	Energy	Charge	Energy
0	$5.8 + \mu_e$	+	$3.2 + 2\mu_e$	–	4.1
–	>4.3	0	$3.6 + \mu_e$		
		–	4.2		

results suggesting it as the method for self-diffusion and some some fast-diffusing species in germanium [44, 171, 213].

Boron interstitial structures were found to be in agreement with previous theoretical work in germanium [69], and also very similar to those found in silicon [71, 211]. Boron interstitial complexes were seen to migrate either as a unit or through kick-out mechanisms. In the positive charge state, the migration as a unit exhibited a lower energy barrier of 0.6 eV, while in the neutral and singly negative, the kick-out mechanism was slightly more favourable at 0.4 and 0.7 eV respectively. Total energy barriers, including the formation energies of the BI with respect to $\mathrm{B}^{-}_{\mathrm{Ge}}$ for diffusion in the +, 0 and - charge states were then given as $3.2 + 2\mu_e$, $3.6 + \mu_e$ and 4.2 eV respectively.

Correlated Exchange has been investigated, and is observed to have a large diffusion barrier, of 4.1 eV, in the singly negatively charged case. Therefore, for most values of the Fermi energy, the interstitial-mediated diffusion path would remain the most favourable.

Figure 7.8 shows the Fermi level dependence of the diffusion barrier of boron in germanium as calculated here and indicates the most favourable diffusion mechanisms for the relevant Fermi level ranges. The results suggest that for μ_e below ~0.5 eV, the diffusion of boron will proceed via an interstitial-mediated mechanism, while for Fermi levels above this, the diffusion could proceed without any mediating defect, though it is unlikely that B-doped material will be sufficiently *n*-type for this to occur.

Prior theoretical work on boron diffusion in silicon has concentrated on the interstitial mediated diffusion method, using a kick-out mechanism to create interstitial

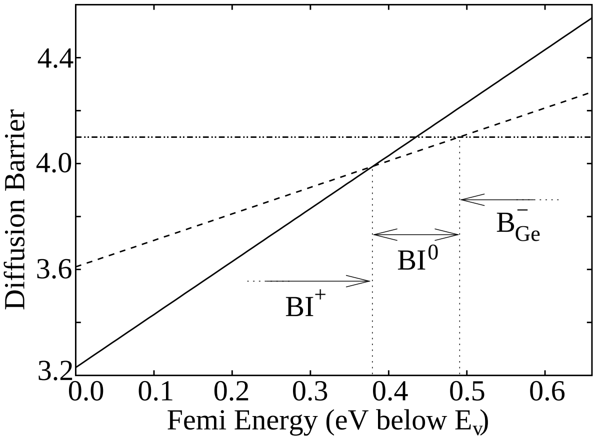

Figure 7.8: Diffusion barrier dependence on Fermi level position for boron complexes. Energies are given relative to singly negatively charged substitutional boron. Only the barriers which are most favourable for some Fermi level positions are displayed. Arrows and labels on the graphs indicate the most favourable path in the indicated regions.

boron impurities which then diffuse within the ⟨110⟩ channels with low diffusion barriers. A total activation energy for this process of 3.2-3.6 eV dependent on charge state is reported [61, 70, 71]. This is close to the energy barriers reported here.

Experimental studies of boron diffusion in germanium have been carried out at high temperatures, where the Fermi level is expected to lie around mid gap. The results presented above give a diffusion barrier for boron of around 3.8-3.9 eV for this value of μ_e. This is significantly lower than the experimental values of ~4.5 eV and the theory presented here can also not explain the high experimental pre-exponential factor of 6×10^8 down to 1.97×10^5 cm^{2}s^{-1} [58, 66, 67]. It is seen that both the barrier and path calculated here are similar to that found experimentally [75] and theoretically [61] in silicon, suggesting that the processes observed in silicon and calculated in germanium may be similar. It was therefore decided to try using the pre-factor of 0.87 cm^{2}s^{-1} measured in silicon with the barriers calculated here to calculate a diffusivity for boron in germanium. This leads to a diffusivity of $\sim 10^{-18}$ cm^{2}s^{-1} for a temperature of 800 °C. For that temperature, the experimental studies in germanium give diffusivities of 3×10^{-17} cm^{2}s^{-1} [58], 6×10^{-15} cm^{2}s^{-1} [66], and 4×10^{-13} cm^{2}s^{-1} [67]. The calculated value is seen to be lower than the smallest value found from experiment, but not excessively so. This may suggest that the diffusion observed and calculated in silicon follows the same or similar path to that calculated for germanium and the experimentally observed diffusion in germanium may not be very far removed either.

An explanation for these discrepancies in pre-exponential factors and diffusion barriers between theory and experiment in germanium can be drawn from an earlier theoretical study of the effect of high temperature electronic excitations on observed diffusion processes in germanium and silicon [214]. In that paper, calculations were performed for a general migration process, for temperatures approaching the melting point. The excitations were found to increase both the energy barrier experienced by the diffusing species and also the entropy of the process, leading to an increase in the pre-exponential factor. The two effects were found to compete with each other and result in a diffusivity which was almost unaffected. This is presented by the authors as an explanation of the empirical compensation effect or Meyer-Neldel rule [215]. In germanium, the excitations were calculated to lead to an increase in the energy barrier of ~ 1 eV, and an increase in the pre-exponential factor of $\sim 10^5$ cm^{2}s^{-1}. Applying these temperature-induced modifications to the results of the calculations here would then bring the modelling results in line with the experimental results described.

7.5 Chapter Summary

Phosphorus and boron diffusion have been studied in germanium with a variety of diffusion paths. Vacancy and interstitial-mediated diffusion have been studied at length as well as a correlated exchange mechanism for diffusion without the presence of a mediating defect.

For phosphorus, the vacancy-mediated diffusion path was found to be the most important, particularly for *n*-type material. For material with a sufficient phosphorus concentration, the P_2V defect is expected to be the dominant diffusing species, while the PV defect will be dominant for less strongly doped material. The results calculated here give a diffusion barrier of ~ 2.5 eV for n-type material, in good agreement with experiment.

For boron, the picture is complicated, apparently by high-temperature effects beyond the scope of the theory being employed. Calculations give $\mathrm{BI}^{0/+}$ as the most mobile species for material with a Fermi level in the middle or lower half of the band gap. The calculated diffusion barriers for boron in germanium are around 3.8 eV, more than 1 eV above those for P, but well below experimental results of around 4.5 eV.

This discrepancy may be resolved by including the effect of temperature induced electronic excitations on the defect migration. Earlier work, studied these for an arbitrary diffusion process in germanium, and found that the diffusion barrier would be increased by ~ 1 eV, while the pre-exponential factor would increase by $\sim 10^5$ cm^{2}s^{-1} [214]. Applying these values would bring the theoretical and experimental results into agreement. This treatment does not appear to be necessary for the phosphorus diffusion results.

Conclusion

With interest in germanium-based technology growing, demand for extending and updating the understanding of defects in germanium crystals and the behaviour of germanium devices is driving a great deal of research in the area. To best further the understanding of these devices, a combination of theoretical and experimental studies is required. Only experimental studies can investigate the full complexity of real devices and processes in germanium, while theoretical work can investigate individual defects or other clearly-defined effect within the more complex whole. Thus the theoretical work presented in this thesis has been related to experimental studies wherever possible.

The choice of supercell or cluster-based calculations to calculate the properties of defects will be an issue for any study using DFT, and some effort was devoted to ascertaining the best method for the studies performed here. Preliminary work on the vacancy and divacancy in silicon, the results and discussion of which was presented in Chapter 3, suggested that the supercell approach gave the best agreement between theory and experiment, and that 216 atom supercells and clusters with 329 Si atoms terminated with 172 H atoms are sufficient to achieve convergence with system size. For later work on silicon the 216 atom supercell was therefore used. For germanium, the picture is complicated by the combination of low experimental band-gap and LDA underestimation of the energy of excited states. This was found to lead to defect-related levels crossing erroneously into the bulk bands of the supercell for the divacancy, and a calculated insensitivity of the properties of the divacancy on the charge state of the system. Cluster calculations, on the other hand, have a wider band-gap, due to quantum confinement effects, and as such allow defect-related energy levels to fall within the band gap more reliably. For the germanium-based work presented in this thesis, then, clusters of 329 Ge and 172 H atoms were used where possible, with supercells of 216 atoms used only where necessary. Comparison was made between the supercell- and cluster-based calculations in Chapters 5 and 7, and in both cases, the results supported the decision to rely on cluster calculations over supercell ones.

Annealing of the divacancy in germanium was studied as mentioned above and the results were presented in Chapter 5. The study started with supercell calculations, but this method was revealed to be unreliable from band-structure analysis and an insensitivity to charge states, and so the study was concluded using cluster calculations. The defect was predicted to anneal through migration to a trapping centre, with a barrier of 1.0 to 1.3 eV, depending on charge state. This was translated into a predicted annealing temperature of 200 to 290°C, with the temperature for the neutral defect in fair agreement with experimentally determined values of 150 or 180°C[26, 27, 30].

Presented next were the results of a study on the properties of larger vacancy clusters in germanium. The clusters were found to be bound at all sizes studied, and all sizes yielded acceptor levels within or below the band gap, suggesting that larger clusters are negatively charged for all values of the Fermi level. Smaller clusters, however, may become neutrally charged in regions of high damage, allowing for the larger clusters to grow without Coulomb repulsion, as has been suggested previously as an explanation of experimental results [142].

Also of interest in this work was the self-interstitial in germanium. Less studied as it had not been believed to be experimentally observed, and was not a dominant defect in germanium, the self-interstitial is studied here to find its stable structure in the neutral charge state and some of its diffusion paths. This preliminary work has since formed the basis of much more extensive work by A. Carvalho [182, 183], and has formed a section of her thesis [184].

Chapter 6 covered a study of dopant-vacancy defects in both silicon and germanium. In silicon, the AsV E-centre and related As_2V and AsBV defects were studied, in an effort to explain experimental results from mesa diodes containing these dopants [187]. None of the defects studied exhibited a donor level at $E_v+0.20$ eV, as observed in the experiment, but the AsBV defect was calculated to have an acceptor level at $E_v + 0.27$ eV which may exhibit donor-like characteristics. No explanation could be reached for a mechanism to form the AsBV defect without AsV being observed in the experiment, however.

The migration barriers calculated for AsV and As_2V lay in good agreement with previous non-AIMPro theoretical work [53, 188], and predicted annealing temperatures for the two defects of $\sim 75 - 255$°C and ~ 575°C respectively, depending on charge state. The first result is in fair agreement with experimental values of $\sim 175 - 225$°C while the result for As_2V is rather higher than experimental values of ~ 420°C.

Phosphorus-vacancy defects in germanium were investigated as a possible species to explain the low activation ceiling for *n*-type doping in germanium. Calculations showed that all the phosphorus-vacancy defects studied were stable with respect to their component parts, and that all except for P_4V inserted acceptor levels into the band gap. P_3V and P_4V have been calculated previously to have negative formation energies, and this was confirmed for these defects along with P_5V_2. A consideration of migration paths for the defects along with a consideration of Coulomb forces suggest that the P_3V defect will be the dominant compensating centre in germanium, in parallel with previous experimental observations in silicon [52]. Comparing the migration barriers for As_2V in silicon and P_2V in germanium, it was calculated that the defect in germanium will migrate at a temperature ~ 100 K below that for silicon. It was suggested that this could explain the ~ 100 K difference in the temperature of post-implantation carrier recovery between the two materials [51, 59], as the annealing of D_3V (D=As,P) is expected to start with the migration of the D_2V centre away from the third donor atom.

Chapter 7 covered two in depth studies into dopant diffusion in germanium. Phosphorus and boron diffusion were calculated to proceed via vacancy and interstitial-mediated mechanisms respectively, in agreement with previous predictions based on experimental and theoretical works. The in-depth studies extend the previous understanding of the various diffusion mechanisms.

Boron diffusion is particularly interesting, as the results calculated from ground-state DFT cannot explain the large experimentally observed diffusivity prefactors. The diffusion barrier was also found to be around ~ 1 eV below that calculated from experimental measurements. This was explained by invoking independent theoretical work on the effect of thermal excitations on migration barriers in germanium and silicon. That work calculated that these effects should raise the entropy of the system, increasing the prefactor and should also raise the diffusion barrier. The values that they calculated for these increases in high temperature germanium are very similar to the differences between the experimental and theoretical calculated results presented here.

Looking forwards, the state of research into germanium devices remains open to a great deal of further research. Many questions are still unanswered and many works previously published, especially those published in the very early days of semiconductor devices, could benefit from the application of more modern techniques. Even the work presented here could be refined in the future with the application of greater computational resources and improved theoretical models. A number of advanced techniques are being developed to overcome the band-gap problem of the LDA, and as these are brought to maturity and computational resources grow to match the higher requirements of these theories, much of the theoretical literature may be re-examined with a greater accuracy and confidence.

Bibliography

[1] G. E. Moore, Electronics **38(8)**, (1965).

[2] G. D. Wilk, R. M. Wallace, and J. M. Anthony, J. Appl. Phys. **89**, 5243 (2001).

[3] B. Depuydt, M. De Jonghe, W. De Baets, I. Romandic, A. Theuwis, C. Quaeyhaegens, C. Deguet, T. Akatsu, and F. Letertre, in Germanium-based Technologies: From Materials to Devices (Elsevier, London, 2007), Chap. 1.

[4] G. Lacaster, Electron Spin Resonance in Semiconductors (Hilger and Watts, London, 1966).

[5] J. Coutinho, R. Jones, V. J. B. Torres, M. Barroso, S. Öberg, and P. R. Briddon, J. Phys. Cond. Mat. **17**, L521 (2005).

[6] A. Janotti, R. Baierle, A. J. R. da Silva, R. Mota, and A. Fazzio, Physica B **273**, 575 (1999).

[7] A. J. R. da Silva, R. Baierle, R. Mota, and A. Fazzio, Physica B **302**, 364 (2001).

[8] M. J. Puska, S. Pöykkö, M. Pesola, and R. M. Nieminen, Phys. Rev. B **58**, 1318 (1998).

[9] A. Fazzio, A. Janotti, A. J. R. da Silva, and R. Mota, Phys. Rev. B **61**, R2401 (2000).

[10] S. Öğüt and J. R. Chelikowsky, Phys. Rev. B **64**, 245206 (2001).

[11] H. Haesslein, R. Sielemann, and C. Zistl, Phys. Rev. Lett. **80**, 2626 (1998).

[12] A. Mesli, L. Dobaczewski, K. Bonde Nielsen, V. Kolkovsky, M. Christian Petersen, and A. Nylandsted Larsen, submitted to Phys. Rev. B.

[13] G. A. Baraff, E. O. Kane, and M. Schlüter, Phys. Rev. B **21**, 5662 (1980).

[14] P. W. Anderson, Phys. Rev. Lett. **34**, 953 (1975).

[15] G. D. Watkins, Phys. Stat. Sol. (a) **186**, 167 (2001).

[16] A. J. R. da Silva, A. Janotti, A. Fazzio, R. J. Baierle, and R. Mota, Phys. Rev. B **62**, 9903 (2000).

[17] M. D. Moreira, R. H. Miwa, and P. Venezuela, Phys. Rev. B **70**, 115215 (2004).

[18] D. L. Trueblood, Phys. Rev. **161**, 828 (1967).

[19] J. C. Bourgoin, P. M. Mooney, and F. Poulin, Inst. Phys. Conf. Ser. **59**, 33 (1981).

[20] R. J. Needs, J. Phys. Cond. Mat. **11**, 10437 (1999).

[21] P. M. Fahey, P. B. Griffin, and J. D. Plummer, Rev. Mod. Phys. **61**, 289 (1989).

[22] J. Vanhellemont *et al.*, Defects and Diffusion Forum **230**, 149 (2004).

[23] A. Giese, N. A. Stolwijk, and H. Bracht, Appl. Phys. Lett. **77**, 642 (2000).

[24] S. Mayberg, Physica B **95**, 38 (1954).

[25] J. M. Meese, Phys. Rev. B **9**, 4373 (1974).

[26] P. M. Mooney, F. Poulin, and J. C. Bourgoin, Phys. Rev. B **28**, 3372 (1983).

[27] F. Poulin and J. C. Bourgoin, Rev. Phys. Appl. **15**, 15 (1980).

[28] P. Ehrhart and H. Zillgen, J. Appl. Phys. **85**, 3503 (1999).

[29] S. Hens, D. Vanhellemont, D. Poelman, P. Clauws, I. Romandic, A. Theuwis, F. Holsteyns, and J. Van Steenbergen, Appl. Phys. Lett. **87**, 061915 (2005).

[30] J. Fage-Pedersen, A. Nylandsted Larsen, and A. Mesli, Phys. Rev. B **62**, 10116 (2000).

[31] V. Kolkovski, M. Christian Petersen, and A. Nylandsted Larsen, Appl. Phys. Lett. **90**, 112110 (2007).

[32] V. Nagesh and J. W. Farmer, J. Appl. Phys. **63**, 1549 (1987).

[33] D. Poelman, O. De Gryse, N. De Roo, O. Janssens, P. Clauws, W. Bras, I. D. Dolbnya, and I. Romandic, J. Appl. Phys. **96**, 6164 (2004).

[34] R. E. Whan, Phys. Rev. **140**, A690 (1965).

[35] A. Polity and F. Rudolf, Phys. Rev. B **59**, 10025 (1999).

[36] G. D. Watkins and J. W. Corbett, Phys. Rev. **138**, A543 (1965).

[37] E. V. Monakhov, B. S. Avset, A. Hallén, and B. G. Svensson, Phys. Rev. B **65**, 233207 (2002).

[38] G. S. Hwang and W. A. Goddard, Phys. Rev. B **65**, 233205 (2002).

[39] G. D. Watkins, J. Appl. Phys. **103**, 106106 (2008).

[40] T. Y. Tan and U. Gösele, Appl. Phys. A: Solids Surf. **37**, 1 (1985).

[41] H. Zimmermann and H. Ryssel, Appl. Phys. A: Solids Surf. **55**, 121 (1992).

[42] H. Bracht, N. A. Stolwijk, and H. Mehrer, Phys. Rev. B **52**, 16542 (1995).

[43] H. Bracht, J. Fage Pedersen, N. Zangenberg, A. Nylandsted Larsen, E. E. Haller, G. Lulli, and M. Posselt, Phys. Rev. Lett. **91**, 245502 (2003).

[44] M. Werner, H. Mehrer, and H. D. Hocheimer, Phys. Rev. B **32**, 3930 (1985).

[45] H. D. Fuchs, W. Walukiewicz, E. E. Haller, W. Dondl, R. Schorer, G. Abstreiter, A. I. Rudnev, A. V. Tikhomirov, and V. I. Ozhogin, Phys. Rev. B **51**, 16817 (1995).

[46] M. Kaukonen, R. Jones, and P. R. Briddon, Phys. Rev. B **64**, 245213 (2001).

[47] J. O. Kessler, Phys. Rev. **106**, 654 (1957).

[48] L. V. Azároff, Introduction to Solids (McGraw-Hill Book Company, Inc., New York, 1960).

[49] V. V. Emtzev, T. V. Mashovetz, and S. M. Ryvkin, Defects in Semiconductors **1**, 17 (1972).

[50] P. Markevich, V, I. D. Hawkins, A. R. Peaker, K. V. Emstev, V. V. Litvinov, L. I. Murin, and L. Dobaczewski, Phys. Rev. B **70**, 235213 (2004).

[51] V. Ranki, K. Saarinen, J. Fage-Pedersen, J. Lundsgaard Hansen, and A. Nylandsted Larsn, Phys. Rev. B **67**, 041201 (2003).

[52] V. Ranki, A. Pelli, and K. Saarinen, Phys. Rev. B **69**, 115205 (2004).

[53] M. Ramamoorthy and S. T. Pantelides, Phys. Rev. Lett. **76**, 4753 (1996).

[54] J. Coutinho, V. J. B. Torres, S. Öberg, A. Carvalho, C. Janke, R. Jones, and P. R. Briddon, J. Mater Sci: Mater Electron **18**, 769 (2006).

[55] A. Chroneos, R. W. Grimes, B. P. Uberuaga, and H. Bracht, Phys. Rev. B **77**, 235208 (2008).

[56] Y. L. Chao, S. Prussin, J. C. S. Woo, and R. Scholz, Appl. Phys. Lett. **87**, 142102 (2005).

[57] C. O. Chui, K. Gopalakrishnan, J. D. Griffin, P. B. Plummer, and K. C. Saraswat, Appl. Phys. Lett. **83**, 3275 (2003).

[58] S. Uppal, A. F. W. Willoughby, J. M. Bonar, N. E. B. Cowern, T. Grasby, R. J. H. Morris, and M. G. Dowsett, J. Appl. Phys. **96**, 1376 (2004).

[59] C. O. Chui, L. Kulig, J. Moran, W. Tsai, and K. C. Saraswat, Appl. Phys. Lett. **87**, 091909 (2005).

[60] J. Adey, R. Jones, and P. R. Briddon, Appl. Phys. Lett. **83**, 665 (2003).

[61] W. Windl, M. M. Bunea, R. Stumpf, S. T. Dunham, and M. P. Masquelier, Phys. Rev. Lett. **83**, 4345 (1999).

[62] J. S. Nelson, P. A. Schultz, and A. F. Wright, Appl. Phys. Lett. **73**, 247 (1998).

[63] X.-Y. Liu, W. Windl, K. M. Beardmore, and M. P. Masquellier, Appl. Phys. Lett. **82**, 1839 (2003).

[64] S. Eguchi, J. L. Hoyt, C. W. Leitz, and A. Fitzgerald, Appl. Phys. Lett. **80**, 1743 (2002).

[65] A. Satta, E. Simoen, T. Clarysse, T. Janssens, A. Bendetti, B. De Jaeger, M. Meuris, and W. Vandervorst, Appl. Phys. Lett. **87**, 172109 (2005).

[66] W. Meer and D. Pommerring, Z. Angew. Math. Phys. **23**, 369 (1967).

[67] W. C. Dunlap Jr., Phys. Rev. **94**, 1531 (1954).

[68] N. A. Stolwijk, in Impurities and Defects in Group IV Elements and III-V Compounds, edited by M. Schulz and Landolt-Börnstein (Springer, Berlin, 1989), Vol. 22A.

[69] P. Delugas and V. Fiorentini, Phys. Rev. B **69**, 085203 (2004).

[70] B. Sadigh, T. J. Lenosky, S. K. Theiss, M. J. Caturla, T. D. de la Rubia, and M. A. Foad, Phys. Rev. Lett. **83**, 4241 (1999).

[71] M. Hakala, M. J. Puska, and R. M. Nieminen, Phys. Rev. B **61**, 8155 (2000).

[72] M. S. Carroll and R. Koudelka, Semicond. Sci. Tech. **22**, S164 (2007).

[73] S. Brotzmann, H. Bracht, J. Lundsgaard Hansen, A. Nylandsted Larsen, E. Simoen, E. E. Haller, J. S. Christensen, and P. Werner, Phys. Rev. B **77**, 235207 (2008).

[74] E. Simoen and C. Clayes, in Germanium-based Technologies: From Materials to Devices (Elsevier, London, 2007), Chap. 3.

[75] H. Bracht, H. H. Silvestri, I. D. Sharp, and E. E. Haller, Phys. Rev. B **75**, 035211 (2007).

[76] M. Born and J. R. Oppenheimer, Ann. Physik (Leipzig) **84**, 457 (1927).

[77] J. K. L. MacDonald, Phys. Rev. **43**, 830 (1933).

[78] J. M. Thijssen, Computational Physics (Cambridge University Press, Cambridge, 1999).

[79] V. Fock, Z. Phys. **61**, 126 (1930).

[80] V. Fock, Z. Phys. **62**, 795 (1930).

[81] J. C. Slater, Phys. Rev. **35**, 210 (1930).

[82] C. C. J. Roothaan, Rev. Mod. Phys. **23**, 69 (1951).

[83] T. Koopmans, Physica **1**, 104 (1934).

[84] I. Shavitt, Molecular Phys. **94**, 3 (1998).

[85] P. Hohenberg and W. Kohn, Phys. Rev. **136**, B864 (1964).

[86] W. Kohn and L. J. Sham, Phys. Rev. **140**, A1133 (1965).

[87] J. P. Perdew and A. Zunger, Phys. Rev. B **23**, 5048 (1981).

[88] U. von Barth and L. Hedin, J. Phys. C **5**, 1629 (1972).

[89] D. Ceperley, Phys. Rev. B **18**, 3126 (1978).

[90] D. M. Ceperley and B. J. Alder, Phys. Rev. Lett. **45**, 566 (1980).

[91] S. J. Vosko, L. Wilk, and M. Nusair, Chinese J. Phys. **58**, 1200 (1980).

[92] J. P. Perdew and Y. Wang, Phys. Rev. B **45**, 13244 (1992).

[93] R. M. Nieminen, Topics in Appl. Phys. **104**, 29 (2007).

[94] J. Heyd, J. E. Peralta, G. E. Scuseria, and R. L. Martin, J. Chem. Phys. **123**, 174101 (2005).

[95] J. P. Perdew, in Electronic Structure of Solids '91, edited by P. Ziesche and H. Eschrig (Akademie Verlag, Berlin, 1991).

[96] J. P. Perdew, K. Burke, and M. Ernzerhof, Phys. Rev. Lett. **77**, 3865 (1996).

[97] J. P. Perdew, K. Burke, and Y. Wang, Phys. Rev. B **54**, 16533 (1996).

[98] S. G. Louie, S. Froyen, and M. L. Cohen, Phys. Rev. B **26**, 1738 (1982).

[99] G. B. Bachelet, D. R. Hamann, and M. Schlüter, Phys. Rev. B **26**, 4199 (1982).

[100] N. Troullier and J. L. Martins, Phys. Rev. B **43**, 1993 (1991).

[101] C. Hartwigsen, S. Goedecker, and J. Hutter, Phys. Rev. B **58**, 3641 (1998).

[102] R. Jones and P. R. Briddon, in Identification of Defects in Semiconductors, Vol. 51A of Semiconductors and Semimetals, edited by M. Stavola (Academic Press, Boston, 1998), Chap. 6, pp. 287–349.

[103] J. Coutinho, S. Öberg, V. J. B. Torres, and P. R. Briddon, Phys. Rev. B **73**, 235213 (2006).

[104] A. Resende, R. Jones, S. Öberg, and P. R. Briddon, Phys. Rev. Lett. **82**, 2111 (1999).

[105] B. R. Davidson, R. C. Newman, C. D. Latham, R. Jones, C. C. Button, and P. R. Briddon, Phys. Rev. B **60**, 5447 (1999).

[106] E. V. Lavrov, B. B. Nielsen, J. R. Byberg, B. Hourahine, R. Jones, S. Öberg, and P. R. Briddon, Phys. Rev. B **62**, 158 (2000).

[107] L. Hoffmann, E. V. Lavrov, B. B. Nielsen, B. Hourahine, R. Jones, S. Öberg, and P. R. Briddon, Phys. Rev. B **61**, 16659 (2000).

[108] A. N. Larsen *et al.*, Phys. Rev. B **62**, 4535 (2000).

[109] L. Hoffmann, B. B. Nielsen, A. N. Larsen, P. Leary, P. R. Briddon, and S. Öberg, Phys. Rev. B **60**, 13573 (1999).

[110] S. Öğüt, H. Kim, and J. R. Chelikowsky, Phys. Rev. B **56**, R11353 (1997).

[111] P. R. Briddon and R. Jones, Phys. Stat. Sol. (b) **217**, 131 (2000).

[112] M. J. Rayson and P. R. Briddon, Comp. Phys. Comms. **178**, 128 (2008).

[113] J. P. Goss, M. J. Shaw, and P. R. Briddon, Topics Appl. Phys. **104**, 67 (2007).

[114] D. J. Chadi and M. L. Cohen, Phys. Rev. B **7**, 692 (1973).

[115] A. Baldreschi, Phys. Rev. B **7**, 5212 (1973).

[116] H. J. Monkhorst and J. D. Pack, Phys. Rev. B **13**, 5188 (1976).

[117] A. Nylandsted Larsen, A. Mesli, K. Bonde Nielsen, H. Kortegaard Nielsen, L. Dobaczewski, J. Adey, R. Jones, D. W. Palmer, P. R. Briddon, and S. Öberg, Phys. Rev. Lett. **97**, 106402 (2006).

[118] B. G. Svensson, B. Mohadjeri, A. Hallén, J. H. Svensson, and J. W. Corbett, Phys. Rev. B **43**, 2292 (1991).

[119] C. O. Almbladh and U. von Barth, Phys. Rev. B **31**, 3231 (1985).

[120] R. P. Feynman, Phys. Rev. **56**, 340 (1939).

[121] S. T. Epstein, A. C. Hurley, R. E. Wyatt, and R. G. Parr, J. Chem. Phys. **47**, 1275 (1967).

[122] F. Reif, Fundamentals fo Statistical and Thermal Physics, Fundamentals of Physics, 1st ed. (McGraw-Hill, New York, 1965).

[123] C. P. Flynn, Point Defects and Diffusion (Clarendon Press (Oxford University Press), Oxford, 1972).

[124] J. Coutinho, R. Jones, P. R. Briddon, S. Öberg, L. I. Murin, V. P. Markevich, and J. L. Lindström, Phys. Rev. B **67**, 035205 (2003).

[125] G. Henkelman, G. Jóhannesson, and H. Jónsson, in Progress on Theoretical Chemistry and Physics, edited by S. D. Schwartz (Kluwer Academic Publishers, Netherlands, 2000), p. 269.

[126] G. Henkleman, B. P. Uberuaga, and H. Jónsson, J. Chem. Phys. **113**, 9901 (2000).

[127] G. Henkleman and H. Jónsson, J. Chem. Phys. **113**, 9978 (2000).

[128] CRC Handbook of Chemistry and Physics, 81st ed., edited by D. R. Lide (CRC Press LLC, Boca Raton, 2000).

[129] S. Goedecker, M. Teter, and J. Hutter, Phys. Rev. B **54**, 1703 (1996).

[130] D. V. Lang, J. Appl. Phys. **45**, 3014 (1974).

[131] C. E. Lindberg, J. Lundsgaard Hansen, P. Bomholt, A. Mesli, K. Bonde Nielsen, A. Nylandsted Larsen, and L. Dobaczewski, Appl. Phys. Lett. **87**, 172103 (2005).

[132] A. O. Evwaraye, J. Appl. Phys. **48**, 734 (1977).

[133] A. O. Evwaraye, J. Appl. Phys. **48**, 1840 (1977).

[134] G. L. Miller, D. V. Lang, and L. C. Kimerling, Ann. Rev. Mater. Sci. **7**, 377 (1977).

[135] P. M. Mooney, in Identification of Defects in Semiconductors, Vol. 51B of Semiconductors and Semimetals, edited by M. Stavola (Academic Press, San Diego, 1999), p. 93.

[136] A. Blondeel, P. Clauws, and D. Vyncke, J. Appl. Phys. **81**, 6767 (1997).

[137] L. Dobaczewski, P. Kaczor, I. D. Hawkins, and A. R. Peaker, J. Appl. Phys. **76**, 194 (1994).

[138] D. V. Lang, J. Appl. Phys. **45**, 3023 (1974).

[139] J. H. Bleka, E. V. Monakhov, B. G. Svensson, and B. S. Avset, Phys. Rev. B **76**, 233204 (2007).

[140] M. T. Asom, J. L. Benton, R. Sauer, and L. C. Kimerling, Appl. Phys. Lett. **51**, 256 (1987).

[141] R. Kögler, A. Peeva, A. Mücklich, F. Eichhorn, and W. Skorupa, Appl. Phys. Lett. **88**, 101918 (2006).

[142] A. R. Peaker, V. P. Markevich, J. Slotte, K. Kuitunen, F. Tuomisto, A. Satta, E. Simoen, I. Capan, B. Pivac, and R. Jačimović, Sol. Stat. Phen. **131-133**, 125 (2008).

[143] D. A. Abdulmalik, P. G. Coleman, H. A. W. El Mubarek, and P. Ashburn, J. Appl. Phys. **102**, 013530 (2007).

[144] X. D. Pi, C. P. Burrows, and P. G. Coleman, Phys. Rev. Lett. **90**, 155901 (2003).

[145] I. Procháka, Mater. Struct. **8**, 55 (2001).

[146] K. Saarinen, P. Hautojärvi, and C. Corbel, in Identification of Defects in Semiconductors, Vol. 51A of Semiconductors and Semimetals, edited by M. Stavola (Academic Press, San Diego, 1998), p. 210.

[147] T. M. Børseth, F. Tuomisto, J. S. Christensen, E. V. Monakhov, B. G. Svensson, and A. Y. Kuznetsov, Phys. Rev. B **77**, 045204 (2008).

[148] A. Benninghoven, F. G. Rudenauer, and H. W. Werner, Secondary Ion Mass Spectrometry (John Wiley, New York, 1987).

[149] J. B. Clegg, in Growth and Characterisation of Semiconductors, edited by R. A. Stradling and P. C. Klipstein (Adam Hilger, Bristol and New York, 1990), Chap. 5.

[150] J. S. Christensen, H. H. Radamson, A. Yu. Kuznetsov, and B. G. Svensson, Appl. Phys. Lett. **82**, 2254 (2003).

[151] P. M. Rousseau, P. B. Griffin, and J. D. Plummer, Appl. Phys. Lett. **65**, 578 (1994).

[152] A. Chroneos, D. Skarlatos, C. Tsamis, A. Christofi, D. S. McPhail, and R. Hung, Mat. Sci. Semicond. Proc. **9**, 640 (2006).

[153] J. Huang, N. Wu, Q. Zhang, C. Zhu, A. A. O. Tay, G. Chen, and M. Hong, Appl. Phys. Lett. **87**, 173507 (2005).

[154] P. P. Sigmund, Phys. Rev. B **184**, 383 (1969).

[155] Q. X. Zhao, S. M. Wang, M. Sadeghi, A. Larsson, M. Friessel, and M. Willander, Appl. Phys. Lett. **89**, 031907 (2006).

[156] W. R. Runyan, Semiconductor Measurements and Instrumentation (McGraw-Hill Kogakusha, Ltd., Tokyo, 1975).

[157] T. Clarysse and W. Vandervost, J. Vac. Sci. Tech. B **18**, 369 (2000).

[158] T. Clarysse and W. Vandervost, J. Vac. Sci. Tech. B **18**, 381 (2000).

[159] V. Prvitera, W. Vendervost, and T. Clarysse, J. Electrochem. Soc. **140**, 262 (1993).

[160] G. Mannino, S. Solmi, V. Privitera, and M. Bersani, Appl. Phys. Lett. **79**, 3764 (2001).

[161] I. Watt, The principles and practise of electron microscopy, 2nd ed. (Camridge University Press, Cambridge, 1997).

[162] P. Schwander, W. D. Rau, C. Kisielowski, M. Gribelyuk, and A. Ourmazd, in Identification of Defects in Semiconductors, Vol. 51B of Semiconductors and Semimetals, edited by M. Stavola (Academic Press, San Diego, 1999), p. 226.

[163] C. W. Nieh and L. J. Chen, Appl. Phys. Lett. **48**, 1528 (1986).

[164] R. Feynman, Eng. and Sci. **22**, (1960).

[165] D. R. Strachan, D. E. Johnston, B. S. Guiton, S. S. Datta, P. K. Davies, D. A. Bonnell, and A. T. Charlie Johnson, Phys. Rev. Lett. **100**, 056805 (2008).

[166] N. D. Jäger and E. R. Weber, in Identification of Defects in Semiconductors, Vol. 51B of Semiconductors and Semimetals, edited by M. Stavola (Academic Press, San Diego, 1999), p. 262.

[167] M. Ahola-Tuomi, P. Laukkanen, M. P. J. Punkkinen, R. E. Perälä, I. J. Väyrynen, M. Kuzmin, K. Schulte, and M. Pessa, Appl. Phys. Lett. **92**, 011926 (2008).

[168] E. Simoen and C. Clayes, in Germanium-based Technologies: From Materials to Devices (Elsevier, London, 2007), Chap. 5.

[169] V. P. Markevich, V. V. Litvinov, L. Dobaczewski, J. L. Lindström, L. I. Murin, S. V. Vetrov, I. D. Hawkins, and A. R. Peaker, Physica B **340-342**, 844 (2003).

[170] H. M. Pinto, J. Coutinho, V. J. B. Torres, S. Öberg, and P. R. Briddon, Mat. Sci. Semicond. Proc. **9**, 498 (2006).

[171] H. Bracht, N. A. Stolwijk, and H. Mehrer, Phys. Rev. B **43**, 14465 (1991).

[172] R. E. Whan, Appl. Phys. Lett. **6**, 221 (1965).

[173] F. C. Gozzo, M. N. Eberlin, and I. Chambouleyron, J. Non-Crys. Sol. **299**, 174 (2002).

[174] J. Coutinho, V. J. B. Torres, R. Jones, A. Carvalho, S. Öberg, and P. R. Briddon, Appl. Phys. Lett. **88**, 091919 (2006).

[175] H. J. Stein, Radiation Damage and Defects in Semiconductors, 315 (1973).

[176] S. R. Morrison and R. C. Newman, J. Phys. C **6**, 1981 (1973).

[177] C. Janke, R. Jones, J. Coutinho, S. Öberg, and P. R. Briddon, Mat. Sci. Semicond. Proc. **9**, 484 (2006).

[178] C. Janke, R. Jones, S. Öberg, and P. R. Briddon, Phys. Rev. B **75**, 195208 (2007).

[179] R. Sielemann, H. Hässlein, C. Zistl, M. Müller, L. Stadler, and V. V. Emstev, Physica B **308-310**, 529 (2001).

[180] C. Zistl, R. Sielemann, H. Hässlein, S. Gall, D. Bräunig, and J. Bollmann, Mater. Sci. Forum **258-263**, 53 (1997).

[181] J. Vanhellemont, P. Śpiewak, and K. Sueoka, J. Appl. Phys. **101**, 036103 (2007).

[182] A. Carvalho, R. Jones, C. Janke, J. P. Goss, P. R. Briddon, J. Coutinho, and S. Öberg, Phys. Rev. Lett. **99**, 175502 (2007).

[183] A. Carvalho, R. Jones, J. P. Goss, C. Janke, S. Öberg, and P. R. Briddon, J. Phys. Cond. Mat. **20**, 135220 (2008).

[184] A. Carvalho, Ph.D. thesis, University of Exeter, 2008.

[185] G. D. Watkins, J. W. Corbett, and R. M. Walker, J. Appl. Phys. **30**, 1198 (1959).

[186] L. C. Kimerling, M. T. Asom, J. L. Benton, P. J. Drevinsky, and C. E. Caefer, Mater. Sci. Forum **38-41**, 141 (1989).

[187] H. Kortegaard Nielsen, A. Mesli, L. Dobaczewski, K. Bonde Nielsen, C. E. Lindberg, V. Privitera, and A. Nylandsted Larsen, Nuclear Instruments and Methods in Physics Research Section B: Beam Interactions **253**, 172 (2006).

[188] J. Xie and S. P. Chen, Phys. Rev. Lett. **83**, 1795 (1999).

[189] G. D. Watkins, Phys. Rev. B **13**, 2511 (1976).

[190] J. Adey, R. Jones, D. W. Palmer, P. R. Briddon, and S. Öberg, Phys. Rev. B **71**, 165211 (2005).

[191] C. Janke, R. Jones, S. Öberg, and P. R. Briddon, Appl. Phys. Lett. **90**, 152103 (2007).

[192] C. D. Mueller, E. Alonso, and W. Fichtner, Phys. Rev. B **68**, 045208 (2003).

[193] H. Kortegaard Nielsen (unpublished).

[194] A. Nylandsted Larsen, K. Kyllesbech Larsen, P. E. Andersen, and B. G. Svensson, J. Appl. Phys. **73**, 691 (1993).

[195] H. Höhler, N. Atodiresei, K. Schroeder, R. Zeller, and P. H. Dederichs, Phys. Rev. B **71**, 035212 (2005).

[196] C. Janke, R. Jones, J. Coutinho, S. Öberg, and P. R. Briddon, Mat. Sci. Semicond. Proc., in press .

[197] I. Kovačević, B. Pivac, R. Jačimović, M. K. Khan, V. P. Markevich, and A. R. Peaker, Mat. Sci. Semicond. Proc. **9**, 606 (2006).

[198] S. M. Sze, Physics of Semiconductor Devices, 2nd ed. (John Wiley & Sons, Inc., New York, 1981).

[199] K. C. Pandey, Phys. Rev. Lett. **57**, 2287 (1986).

[200] S. Brotzmann and H. Bracht, J. Appl. Phys. **103**, 033508 (2008).

[201] A. Chroneos, R. W. Grimes, B. P. Uberuaga, S. Brotzmann, and H. Bracht, Appl. Phys. Lett. **91**, 192106 (2007).

[202] A. Satta, E. Albertazzi, G. Lulli, and L. Columbo, Phys. Rev. B **72**, 235206 (2005).

[203] J. Xie and S. P. Chen, J. Appl. Phys. **87**, 4160 (2000).

[204] A. Chroneos, H. Bracht, R. W. Grimes, and B. P. Uberuaga, Appl. Phys. Lett. **91**, 172103 (2008).

[205] C. Ahn, Ph.D. thesis, University of Washington, 2007.

[206] C. Janke, R. Jones, S. Öberg, and P. R. Briddon, Phys. Rev. B **77**, 195210 (2008).

[207] A. Satta, B. Van Daele, E. Simoen, and W. Vandervorst (unpublished).

[208] S. Matsumoto, Y. Ishikawa, and T. Niimi, J. Appl. Phys. **54**, 5049 (1983).

[209] Y. Ishikawa, I. Nakamichi, S. Matsumoto, and T. Niimi, Jpn. J. Appl. Phys. Part 1, **26**, 1602 (1987).

[210] C. Janke, R. Jones, S. Öberg, and P. R. Briddon, Phys. Rev. B **77**, 075208 (2008).

[211] J. Adey, J. P. Goss, R. Jones, and P. R. Briddon, Phys. Rev. B **67**, 245325 (2003).

[212] R. D. Harris, J. L. Newton, and G. D. Watkins, Phys. Rev. B **36**, 1094 (1987).

[213] F. C. Frank and D. Turnbull, Phys. Rev. **104**, 617 (1956).

[214] Y. L. Khait, R. Beserman, D. Shaw, and K. Dettmer, Phys. Rev. B **50**, 14983 (1994).

[215] N. Itoh and A. M. Stoneham, Materials Modification by Electronic Excitation (Cambridge University Press, Cambridge, 2001).